Title
Early Cancer Detection and Targeted Therapy by Magnetic Resonance Molecular Imaging and Nano Medicine

Author
Li, Zhao

Publication Date
2015

Peer reviewed|Thesis/dissertation

UNIVERSITY OF CALIFORNIA

Los Angeles

Early Cancer Detection and Targeted Therapy by Magnetic Resonance Molecular Imaging and Nano Medicine

A dissertation submitted in partial satisfaction

of the requirements for the degree Doctor of Philosophy

in Chemistry

by

Zhao Li

2015

ABSTRACT OF THE DISSERTATION

Early Cancer Detection and Targeted Therapy

by Magnetic Resonance Molecular Imaging and Nano Medicine

by

Zhao Li

Doctor of Philosophy in Chemistry

University of California, Los Angeles, 2015

Professor Yung-Ya Lin, Chair

The common theme of my 5-year PhD research is to channel progress in spin physics and nano-bio-materials into meaningful improvements in the theoretical studies, methodological developments, and advanced applications of magnetic resonance (MR) to:

1) MR Molecular Imaging: to detect lesions (especially cancers) at early stages through imaging the existence and locations of physiologically important biomarkers; and
2) MR Nano Medicine: to cure diseases (especially cancers) by targeted therapy through nanodrugs and hyperthermia.

The research activities had encompassed a balanced approach to develop a rigorous theoretical understanding on sensitively imaging magnetic nanoparticles by active- feedback spin dynamics of selective self-excitation and fixed-point dynamics on one hand and sound methodology with biomedical applicability to early pancreatic cancers and brain tumors

detection on the other. Computer simulations, phantom experiments of superparamagnetic nanoparticles, and in vivo experiments of orthotopic pancreatic cancer and brain tumor mouse models had been used to validate the applicability and efficacy of our proposed methods.

The major research projects and achievements with my coworkers under the supervision of Prof. Yung-Ya Lin include:

1) Developed original MR method, "Active-Feedback Fixed-Point Imaging", for early cancer detection, with both quantum and classical formulation of the spin dynamics.
2) Demonstrated 3-5 times of enhancement in the contrast-to-noise ratio (CNR) of early pancreatic cancers which were targeted and labeled by CA19-9 conjugated magnetic nanoparticles by our "Spin Avalanche Amplification" method, based on statistics from 7 orthotopic pancreatic cancer mouse models.
3) Demonstrated 4-10 times of enhancement in the CNR of early GBM (glioblastoma multiforme, the most common and aggressive form of brain cancers) by our "Active-Feedback Fixed-Point Imaging" method, based on statistics from 20 orthotopic GBM mouse models.
4) Developed novel multifunctional, theranostic, smart nanoparticles, called "UCS-Gd-Dox" for MR imaging and targeted cancer therapy. By conjugating Gd^{3+} at the stable core of unibody core-shell polymer (UCS) and encapsulating doxorubicin (Dox) at the shell in a pH-sensitive manner, we achieved a selective drug release (75% difference between pH 7.4 and 5.5) and MR imaging ($r1 = 0.9$ and $14.5\ mM^{-1}s^{-1}$ at pH 7.4 and 5.5, respectively). The anti-cancer effect is significantly better than free

cancer drugs in tumor-bearing mouse models, presumably due to enhanced permeability and retention effect and pH-triggered release.

5) Formulated more accurate theoretical description to magnetic resonance hyperthermia, including aggregation/disruption of monomers/clusters and nonlinear response under strong external magnetic field.

The dissertation of Zhao Li is approved.

William M. Gelbart

M. Albert Thomas

Yung-Ya Lin, Committee Chair

University of California, Los Angeles

2015

TABLE OF CONTENTS

Part III. Spin Control

Part IV. MR Theranostics

ACKNOWLEDGEMENTS

I want to first express my most sincere and deepest gratitude to my PhD advisor, Prof. Yung-Ya Lin, for his tremendous, enormous support all the time, for creating an exciting research environment, and for invaluable guidance and support at various pivotal points of my undergraduate and graduate career. His enthusiasm infects the group so that excellence and originality in research work is encouraged and expected. I have never seen such a devoted and sincere faculty who does research and teaching with a heart!

I want to thank all the faculty members in my PhD committee: Prof. William M. Gelbart, Prof. M. Albert Thomas, and Prof. Xiangfeng Duan, for their continuous encouragement and insightful comments.

I want to thank all professors and staff in the Department of Chemistry and Biochemistry at UCLA, especially Prof. Charles Knobler, Prof. Neil Garg, Prof. Benjamin Schwartz, Prof. Delroy Baugh, Prof. Louis Bouchard, Prof. Alex Levine, Prof. Thomas Mason, Prof. Peter Felker, Prof. Arlene Russell, Prof. Maher Henary, and Prof. Johnny Pang, for their help, support, encouragement, and inspiration under various interactions. My special thanks also goes to Dr. Jane Strouse, Dr. Robert Taylor, Dr. Dafni Amirsakis, and Nanette Jarenwattananon in UCLA MIC, for their continuous supports towards our experiments. In addition, I want to take this opportunity to thank Prof. Ren Sun, Chair of the CSST program at UCLA, and Ms. Helen Chien, Ms. Angie Platt, and Dr. Jiaying Feng of the program.

My gratitude goes to my fellow labmates in the Lin group -- Dr. Stephanie Wolahan, Dr. Chao-Hsiung Hsu, Nikolay Dimitrov, DPharm. Raymond Ngo, Ryan Quiroz, Chencai Wang, Sayoni Ray, Fang-Chu Lin, Huimin Yang, and Tanya Kim, and all our collaborators.

Last but not least, I want to thank my parents, for everything they have been doing for me. I always consider myself as the luckiest daughter in the world.

VITA

Zhao Li

Education

- B.E. in Polymer Science and Engineering, Wu Yuzhang Honors College, Sichuan University, Chengdu, China, July 2010

Awards & Distinctions

- Distinguished Undergraduate Research Award, Sichuan University, April 2010
- Excellence in Second Year Academics and Research, Department of Chemistry and Biochemistry, UCLA, November 2012
- Roy and Dorothy John Fellowship, Division of Physical Sciences, UCLA, August 2014
- Distinguished Teaching Award for Teaching Assistants, Academic Senate, UCLA, April 2015

Chapter 1

Introduction, Objective, and Highlight

1.1 PhD Research Theme

The common theme of my 5-year PhD research is to channel progress in spin physics and nano-bio-materials into meaningful improvements in the theoretical studies, methodological developments, and advanced applications of magnetic resonance to:

1) "Molecular Imaging": to detect lesions (especially cancers) at early stages through imaging the existence and locations of physiologically important biomarkers; and

2) "Nano Medicine": to cure diseases (especially cancers) by targeted therapy through nanodrugs and hyperthermia.

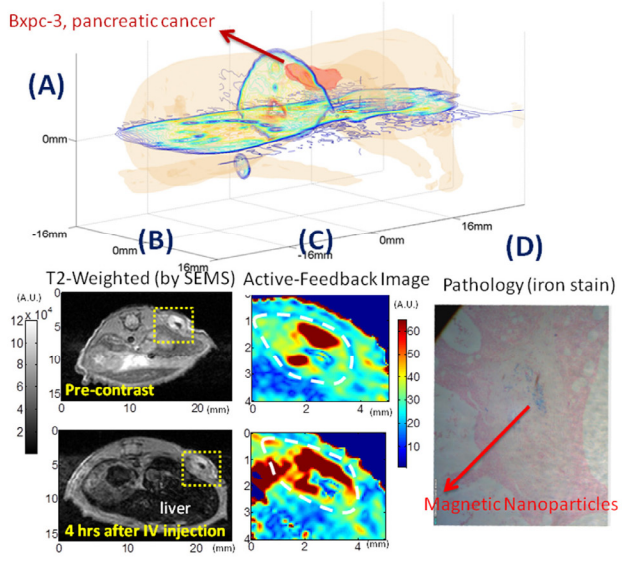

Fig. 1: Detection of pancreatic cancers in subcutaneous xenograft PC mouse models (**A**) by sensitive imaging of the dipolar fields induced by magnetic nanoparticles (**D**). The active feedback images show much improved post-injection contrast (**C**), compared with spin echo T2W images (**B**).

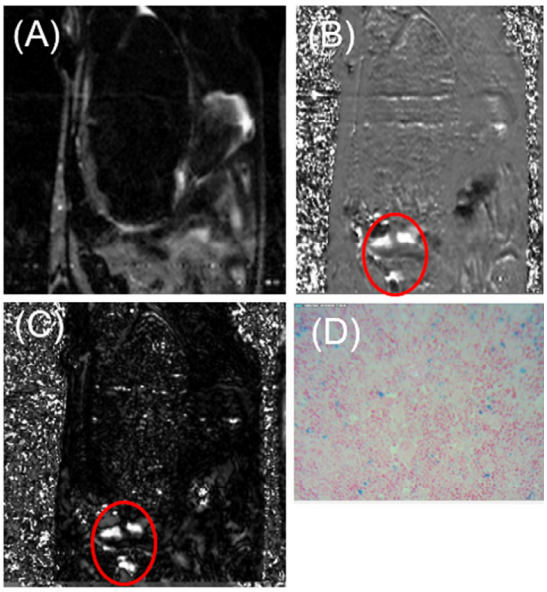

Fig. 2: In vivo images of orthotopic mouse model bearing human PC (from CA 19-9 positive BxPC3 cell lines) labeled by SPIO were acquired. While CPMG-T2 weighted image cannot clearly locate the SPIOs (**A**), the "Active Feedback MR" images shown in (**B**) and (**C**) (acquired with two different active feedback pulse sequences) successfully highlight the SPIO distribution with positive contrast and a close correlation with iron-stained histopathology (**D**).

1.2 Research Highlight

My major research projects and achievements with my coworkers under the supervision of Prof. Yung-Ya Lin includes:

1) Developed original MR method, "Active-Feedback Fixed-Point Imaging", for early cancer detection, with both quantum and classical formulation of the spin dynamics.

2) Demonstrated 3-5 times of enhancement in the contrast-to-noise ratio (CNR) of early pancreatic cancers which were targeted and labeled by CA19-9 conjugated magnetic nanoparticles by our "Spin Avalanche Amplification" method, based on statistics from 7 orthotopic pancreatic cancer mouse models (Figs. 1 and 2)

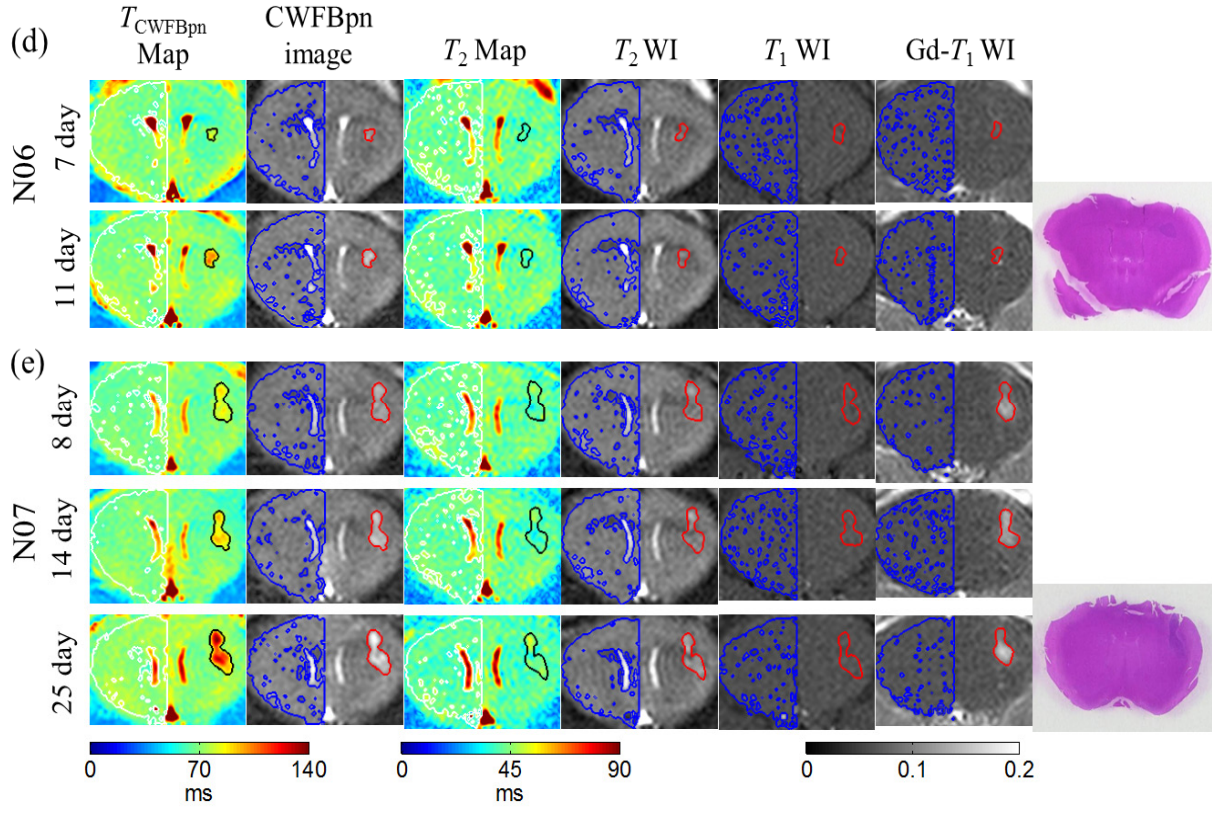

Figure 3. Representative early brain tumor images from Mouse N06 and N07 (out of 20 mouse cancer models) by our "Active-Feedback Fixed-Point Imaging" method (left two columns) and by conventional popular T2, T1, and T1 with Gd methods.

3) Demonstrated 4-10 times of enhancement in the CNR of early GBM (glioblastoma multiforme, the most common and aggressive form of brain cancers) by our "Active-Feedback Fixed-Point Imaging" method, based on statistics from 20 orthotopic GBM mouse models. (Fig. 3 shows representative brain images from two mice, and Fig. 4 shows statistics. Please note the significant improvement in GBM CNR at early stage, Day 0-10, over conventional MR methods)

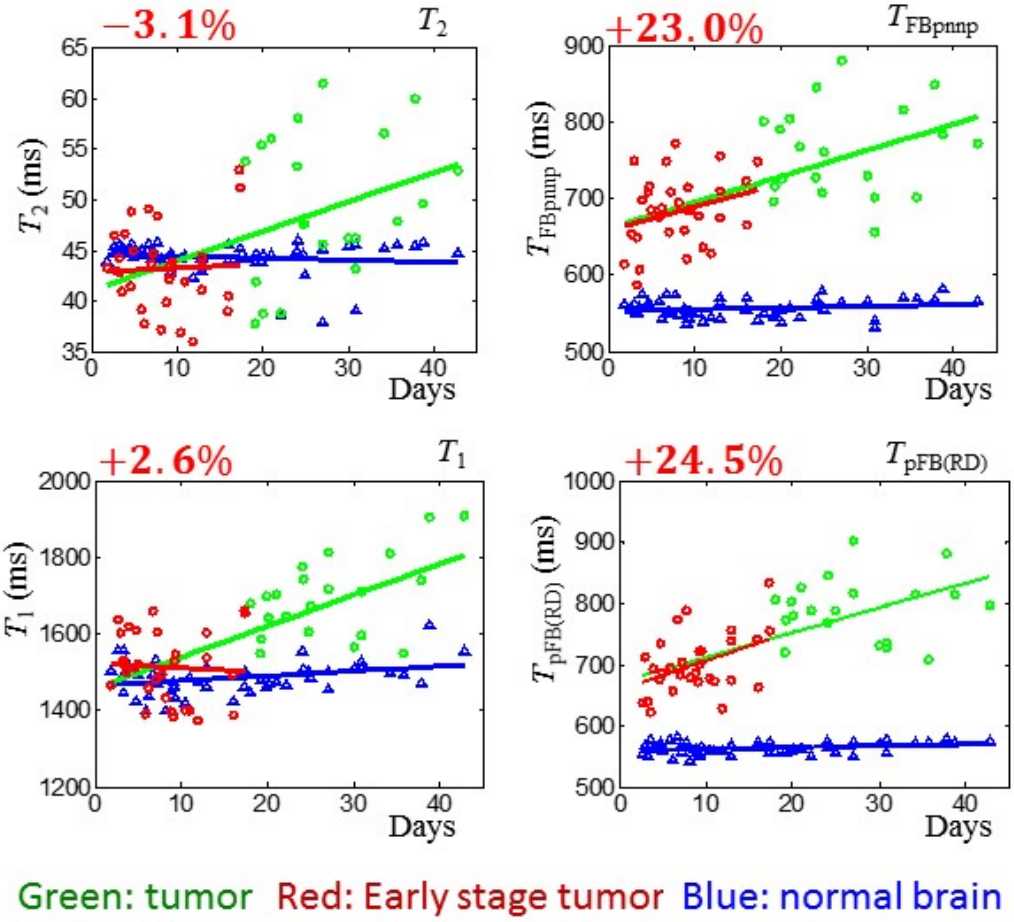

Figure 4. Statistical results of time constants in healthy brain tissues and GBM tissues by our "Active-Feedback Fixed-Point Imaging" method (right columns) and by conventional MR methods, based on 20 orthotopic GBM mouse cancer models.

4) Developed novel multifunctional, theranostic, smart nanoparticles, called "UCS-Gd-Dox" for

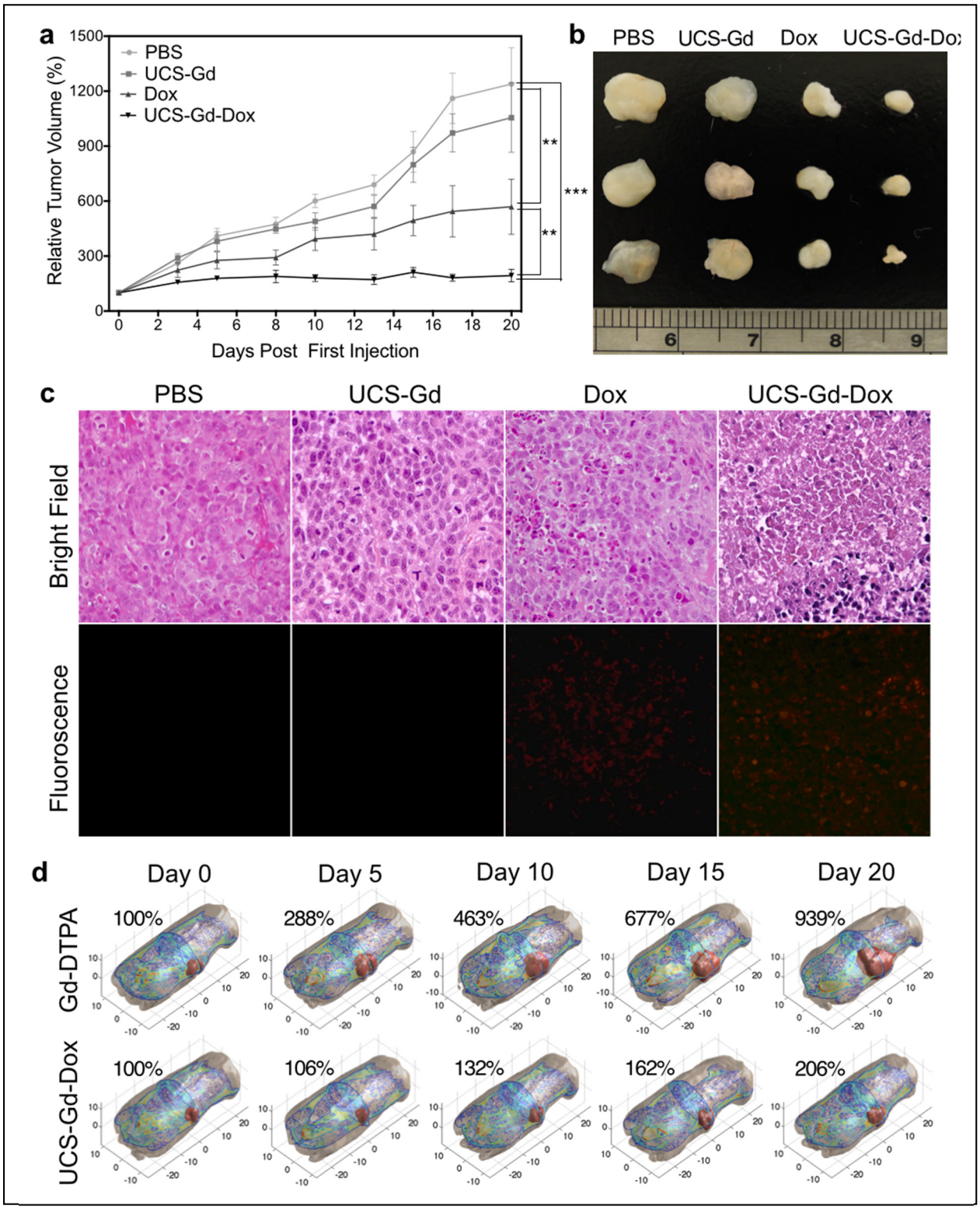

Figure 5. Evaluation of *in vivo* therapeutic efficacy. (a) Anti-cancer efficacy against human cervical cancer in xenograft mouse models after intravenous administration of PBS, UCS-Gd, free Dox and UCS-Gd-Dox over the course of the treatment (20 days). Error bars represent means ± standard deviation (n = 6 mice). Statistical significance: $^{**}P < 0.01$; $^{***}P < 0.001$. (b) Tumor images harvested from mice cancer models at 20 days post-injection of PBS, UCS-Gd, free Dox and UCS-Gd-Dox. (c) Pathological examination of tumor specimens by H&E staining, magnification x400. H&E staining showed wide areas of necrosis in tumor tissues of the UCS-Gd-Dox treated group, but cancer cells grew abundantly in the groups of PBS and UCS-Gd-Dox. (d) Therapeutic effect assessed from the MR images on days 0, 5, 10, 15, and 20. The 3D MR images of Gd-DTPA and UCS-Gd-Dox were reconstructed using MATLAB. The relative tumor volume was shown on the left side of each image.

MR imaging and targeted cancer therapy. By conjugating Gd^{3+} at the stable core of unibody core-shell polymer (UCS) and encapsulating doxorubicin (Dox) at the shell in a pH-sensitive manner, we achieved a selective drug release (75% difference between pH 7.4 and 5.5) and MR imaging (r1 = 0.9 and 14.5 $mM^{-1}s^{-1}$ at pH 7.4 and 5.5, respectively). The anti-cancer effect is significantly better than free cancer drugs in tumor-bearing mouse models, presumably due to enhanced permeability and retention effect and pH-triggered release (Fig. 5).

5) Formulated more accurate theoretical description to magnetic resonance hyperthermia, including aggregation/disruption of monomers/clusters and nonlinear response under strong external magnetic field.

Chapter 2

Active Feedback MR for Sensitive Imaging of Magnetic Nanoparticles for Cancer Detection

2.1 Introduction

In MR imaging and molecular imaging, early lesion detection can be achieved by sensitive imaging of superparamagnetic nanoparticles or aggregates. Superparamagnetic nanoparticles serve as the "molecular beacons" in molecular imaging and have found popular applications because of the following properties: the contrast in T_2- or T_2*-weighted images is stronger than that of the paramagnetic nanoparticles (such as lanthanide oxide nanoparticles and manganese oxide nanoparticles, which may serve as T1 and/or T2 contrast agents) [1], magnetic properties can be manipulated by controlling the sizes of core and coating surface, and iron-oxide nanoparticles show improved biocompatibility and biodegradability. Sensitive detection of superparamagnetic molecular aggregates may improve medical diagnosis by MR imaging. For examples, pathologically, Alzheimer's Disease is characterized by aggregates (called plaques) of amyloid-beta protein that are high in ferritin, an iron storage protein found in the brain [2]. Hemoglobin is the most important component of red blood cells, which is composed of heme and iron. Studies showed that hemoglobin level and its oxygen-carrying capacity strongly correlates with the degree of infarction in acute ischemic stroke patients [3]. Moreover, early-stage tumors are characterized by the formation of new blood vessels to supply tumors with oxygen and nutrients. Therefore, the challenges of early detection of Alzheimer's Disease, stroke, and tumor

may be rendered into sensitive detection of the dipolar fields induced by magnetic nanoparticles or iron-containing molecular aggregates.

In the presence of the Zeeman field, a dipolar field is induced by the superparamagnetic nanoparticles. Such dipolar field creates a spatial and temporal (due to water diffusion) variations to the precession frequency of the near-by water ^{1}H magnetization. The strong local magnetic-field gradient around the dipole center enhances the reversible inhomogeneous and irreversible homogeneous dephasing mechanisms to generate signal void and negative contrast in T_2- or T_2*-weighted images. Improved imaging specificity and identification can be achieved through highlighting the dipole center with positive contrast. For this purpose, Cunningham et al. utilized spectrally selective radio-frequency (RF) pulses to excite and refocus the off-resonance water ^{1}H magnetization surrounding the dipole center to get a positive contrast [4]. Zurikya and Hu presented a diffusion-mediated off-resonance saturation (ORS) method to generate contrast [5]. Seppenwoolde et al. proposed the "white marker" technique and achieved positive contrast by dephasing the background signal with an unmatched gradient echo, while near the dipole center the signal is conserved because the induced dipolar field compensates the dephasing gradient [6]. Mani et al. also achieved a positive contrast using gradient echo acquisition [7].

In this work, a conceptually new approach, termed "active feedback magnetic resonance", was developed to sensitively image superparamagnetic nanoparticles or aggregates with enhanced, robust, and positive contrast for cancer detection. This approach is based on the feedback-induced nonlinear and chaotic spin dynamics that we discovered earlier [8-15]. In summary, an active feedback electronic device was home-built and active feedback pulse sequences were devised to generate avalanching spin amplification, which enhances the weak

dipolar-field perturbations from magnetic nanoparticles in phantom samples, blood clots, and tumors.

The new contributions by this work are two folds. First, it was demonstrated for the first time that feedback-induced contrast enhancement can be achieved in low-field MRI conditions by using home-built active-feedback electronic devices. Second, to motivate potential translational research, active-feedback images from *in vivo* subcutaneous mouse colon cancer models with and without magnetic-nanoparticle labeling are used to evaluate the performance, value, and biomedical applicability of this new approach and to compare with popular T_2- and T_2*-weighted images.

2.2 Theory and Method

2.2.1 Active Feedback Fields

Superparamagnetic nanoparticles or aggregates produce a local magnetic field inhomogeneity, resulting from the difference in magnetic susceptibility with respect to the background materials. The field distribution outside the nanoparticles or aggregates is described by a magnetic dipole, as given by:

$$B_{dip,z}(x,y,z) = c\frac{x^2+y^2-2z^2}{(x^2+y^2+z^2)^{5/2}}$$
$$c = \frac{B_o \Delta\chi V}{4\pi} \quad (1)$$

where B_o is the Zeeman field strength oriented along the +z-axis, and $\Delta\chi V$ describes the local magnetic dose of the dipole as the product of the difference of volume susceptibilities to the environment and the dipole volume [16]. The induced dipolar field changes the precession frequency of the near-by water ^{1}H according to $\Delta\omega=\gamma B_{dip,z}$ where γ is the gyromagnetic ratio of

^{1}H. The water ^{1}H experiences fluctuating magnetic fields due to diffusion within the dipolar field.

Sensitive imaging of magnetic nanoparticles or aggregates may be achieved by manipulating the intrinsic spin dynamics by "selective self-excitation" and "fixed-point dynamics" under active feedback fields, as shown in this work below. Following current MR hardware design, an active feedback field can be generated from the induced free induction decay (FID) current by electronic feedback circuits, as described by the equation

$$\gamma B_{AF,+}(t) = \frac{1}{\tau_{AF}} \left\langle i m_+(\boldsymbol{r},t) \right\rangle e^{-i\psi} = \frac{1}{\tau_{AF}} \{[< m_x > \sin\psi - < m_y > \cos\psi)] + i[< m_x > \cos\psi + < m_y > \sin\psi)]\} \quad (2)$$

where the active feedback field $B_{AF,+} \equiv B_{AF,x} + iB_{AF,y}$, magnetization $\boldsymbol{m}(\boldsymbol{r},t) = \boldsymbol{M}(\boldsymbol{r},t)/M_0$ is normalized with respect to the equilibrium magnetization density M_0 of pure water, and the transverse magnetization $m_+ \equiv m_x + im_y$ [17-23]. Consequently, the equilibrium magnetization vector corresponds to $\boldsymbol{m}$ = [0 0 1] in the (standard) normalized units. The feedback phase, ψ, is related to the angle between the active feedback field vector, $B_{AF,+}(t)$, and the averaged transverse magnetization vector, $<m_+(r,t)>$. For examples, ψ = 0° when feedback field vector, $B_{AF,+}(t)$, lags behind the averaged transverse magnetization vector, $<m_+(r,t)>$, by 90°. In this case, the active feedback field will drive the magnetization towards the stable fixed point along the +z-axis, just as the natural radiation damping effect. On the other hand, when ψ = 180°, the active feedback field vector, $B_{AF,+}(t)$, lags behind the averaged transverse magnetization vector, $<m_+(r,t)>$, by 270° (or equivalently, leads ahead by 90°) and drives the magnetization towards the stable fixed point along the –z-axis [17-23]. The feedback time constant, τ_{AF}, provides a convenient estimate on the time scale of the active feedback spin dynamics, in a way similar to the T_1 or T_2 time constant provides a convenient estimate to the time scale of the relaxation

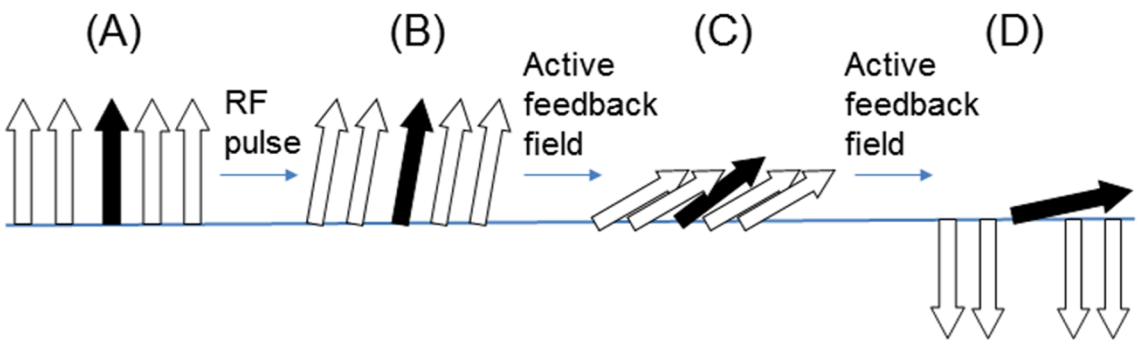

Figure 1. Contrast mechanism by "selective self-excitation" and "fixed-point dynamics" under active feedback fields. Black arrows denote the water ^{1}H magnetization near the center of the dipolar field, while the white arrows denote the bulk water ^{1}H magnetization far away from the dipole center. (A) Under equilibrium condition, all magnetization lines up with external Zeeman field. (B) A small flip-angle (β=5-10^o) RF pulse tilts the sample equilibrium magnetization. (C) Since the averaged transverse magnetization is mainly contributed from the bulk water ^{1}H spins, the resulting active feedback field generated by the active-feedback electronic device possesses a frequency closer to that of the bulk water ^{1}H spins which are distant from the dipole center. By "selective self-excitation", the feedback field tilts the bulk water ^{1}H spins more effectively towards the stable fixed-point, –z-axis (assume feedback phase 180^o), while the ^{1}H spins near the dipole center are less affected due to resonance mismatch. (D) This "selective self-excitation" process continues and enlarges the contrast between the longitudinal magnetization of the ^{1}H spins in bulk water and those near the dipole center. Maximum contrast in the longitudinal magnetization can be achieved and locked when the bulk water spin magnetization evolves to the fixed point: all align along –z in this case.

dynamics. As shown in Eq. (2), the inverse of the feedback time constant, $1/\tau_{AF}$, characterizes the feedback strength, as it is proportional to $B_{AF,+}$. The shorter τ_{AF} is, the stronger the active

feedback field. The radiation damping effect in high-field MR systems with high-Q probes is a passive feedback field with feedback phase $\psi = 0^o$, driving magnetization towards the stable fixed point along the +*z*-axis.

2.2.2 Contrast Mechanism by "Selective Self-Excitation" and "Fixed-Point Dynamics"

The contrast mechanism by "selective self-excitation" and "fixed-point dynamics" under active feedback fields is illustrated by diagram (Fig. 1). First, a small-angle radio-frequency (RF) pulse ($\beta=10^o$ in Fig. 5) tilts the equilibrium magnetization (Fig. 1A). Since the averaged transverse magnetization vector $<m_+(r,t)>$ is mainly contributed from the bulk water ^{1}H magnetization, the resulting active feedback field generated by the active feedback device [Eq. (2)] possesses a frequency much closer to the precession frequency of the bulk water ^{1}H that is far away from the dipole center. By "selective self-excitation", the feedback field self-excites the bulk water magnetization more effectively towards the –z-axis (assume feedback phase $\psi = 180^o$), while the ^{1}H magnetization near the dipole center is less affected due to resonance mismatch (Fig. 1B). This "selective self-excitation" process continues and enlarges the contrast between the longitudinal water ^{1}H magnetization in bulk water and that near the dipole center (Fig. 1C).

The spin dynamics freezes and the contrast gets locked when the bulk water ^{1}H magnetization reaches the fixed point along the –z-axis (with $\psi = 180^o$) and therefore diminish the active feedback fields. In biomedical samples, the strong T_2/T_2* dephasing mechanisms can also crush the averaged transverse magnetization of the bulk water when it is self-excited to rotate to the xy plane from +z axis (with $\psi = 180^o$) and diminish the active feedback field, leaving the magnetization near SPIO along the +z direction to generate enhanced, positive

contrast. This process is termed "fixed-point dynamics". Following a strong z-gradient to spoil the transverse magnetization, the longitudinal water 1H magnetization, $m_z(\boldsymbol{r})$, is excited and spatially encoded using an existing imaging method.

The contrast mechanism by selective self-excitation and fixed-point dynamics under active feedback fields is experimentally robust: the spin dynamics freezes and the contrast gets locked when the bulk water ^{1}H magnetization reaches the fixed point along the –z-axis (with $\psi = 180^o$) and therefore diminish the active feedback fields. In biomedical samples, the strong T_2/T_2* dephasing mechanisms can also crush the averaged transverse magnetization of the bulk water when it is self-excited to rotate to the xy plane from +z axis (with $\psi = 180^o$) and diminish the active feedback field, leaving the magnetization near SPIO along the +z direction to generate enhanced, positive contrast. Similar contrast mechanism can be achieved in MR systems with strong radiation damping, which is a passive feedback field with feedback phase $\psi = 0^o$. In this case, a large flip angle RF pulse ($\beta=170^o$) tilts the equilibrium magnetization close to –z-axis, and then contrast develops on its way back to the +z-axis stable fixed-point by "selective self-excitation" from the passive feedback field of radiation damping ($\psi = 0^o$).

2.2.3 Active Feedback Device

The principle behind the active feedback electronic device is to filter, phase-shift, and amplify the signals from the receiver coils and then re-transmit the modified signal into the RF transmitter coils. Two major objectives in home-building the active feedback electronic device are: a (i) strong and (ii) controllable active feedback field. To fulfill this goal, digitally controlled phase shifter and amplifier were included in the feedback circuit so that the spectrometer hardware can control the trigger signal and the phase, gain, and duration of the active feedback

fields. As a result, we are able to create active feedback pulse sequences that include regular RF fields and active feedback fields at a separate channel, allowing us to utilize the active feedback fields in novel ways. The tunable and programmable feedback phase and gain open new possibilities in pulse sequence design for innovative spin dynamics and applications.

2.2.4 Phantom and *In Vitro* Experiments

In this work, all phantom and *in vitro* experiments were performed on a 14.1-T spectrometer (Bruker Avance 600) equipped with a Micro5 gradient system with maximal gradient strength of 192 G/cm in three orthogonal directions. A 10-mm saddle coil optimized for proton sensitivity was used for RF transmission and reception. The active feedback time constant τ_{AF} was estimated by fitting the FIDs following a 10^{o} RF pulse, taking into account the static field inhomogeneity. The active feedback images were acquired using the sequence shown in Fig. 5, with $\beta = 10°$, feedback phase $\Psi = 180^{o}$, a crusher z-gradient GT = 20 G·ms/cm, and RARE (Rapid Acquisition with Relaxation Enhancement, ref. 24) acquisition (TE = 4.2 ms, TR = 10 s). Conventional T_2*-weighted images by GEFI (gradient-echo fast imaging, ref. 25) pulse sequence (Figs. 6C and 7B, TE = 20 ms, TR = 3 s) and conventional T_2-weighted images by spin-echo RARE pulse sequence (Figs. 6B and 7C, TE = 4.2 ms, TR = 10 s) were acquired for comparison. All images were acquired with the following parameters: sagittal 1-mm thick slices, 512 × 128 voxels zero-filled to 512 × 256 voxels, FOV 1.5 cm.

The 10-mm cylindrical phantom sample, shown in Figs. 5 and 6A, consists of agar with an inner capillary of superparamagnetic nanoparticles (OceanNanotech, 20nm diameter, coated with dextrin) with various degrees of aggregation. Care was taken to avoid the formation of air

bubbles. The concentration of the superparamagnetic nanoparticles injected into the agar solution is 4.8 mg/mL.

For the *in vitro* brain tissue experiments shown in Fig. 7, samples were obtained from a patient undergoing intracranial surgery for glioblastoma multiforme (male, age 6). A 10-mm-diameter block was excised (not needed for immediate pathology examinations) and placed in a 10-mm MR sample tube filled with 0.9% sodium chloride solution.

In imaging processing and imaging simulations, "simulated visibility", VIS_{SIM}, is often used to evaluate the visibility of image features to human eyes, which incorporates not only the contrast but also the spatial extent of the features [26]. It is defined as $VIS_{SIM} = Contrast_{SIM} \times \sqrt{n_{SIM}}$ where "simulated contrast", $Contrast_{SIM}$, is the average contrast of pixels and n_{SIM} is the number of pixels that exceeds a threshold value. To make an objective comparison, the images of the phantom samples shown in Fig. 6 were acquired with pulse sequence parameters and experimental conditions that optimize VIS_{SIM}.

2.2.5 *In Vivo* Experiments

The COLO 205 cells, a human colon adenocarcinoma cell line expressing surface CA19-9 antibody, were purchased from American Type Culture Collection (Manassas, VA) and cultured in RPMI1640 medium (Gibco), supplemented with 10% heat-inactivated fetal bovine serum in a humidified atmosphere at 37 °C with 5% CO_2.

To generate SPIO-labeled cells, COLO 205 cells were incubated for 24 h at 37°C in the serum-free RPMI medium which contains 75 μg SPIO (OceanNanotech, 20nm diameter, coated with dextrin) and 0.75 μg poly-Llysine (PLL, Sigma) per ml. After SPIO was engulfed by the

cells, we washed out residual extracellular SPIO or PLL with fresh phosphate-buffered saline (PBS) three times.

Animal experiments were performed in accordance with the institutional guidelines. The left flank of a nude mouse BALB/cAnN.Cg-Foxn1nu/CrlNarl (National Laboratory Animal Center, Taipei, Taiwan) was injected subcutaneously with COLO 205 cells in 100ul PBS (10^6 cells) , while the other side was injected subcutaneously with SPIO-labeled COLO 205 cells. During the scanning, vital signs of the mouse under anesthesia (about 5% isoflurane induction, 2% for maintenance in air) was monitored and recorded. The flow rate of isoflurane was carefully adjusted to maintain stable heart rate and respiratory rate.

All *in vivo* images in this chapter were acquired on a Varian INOVA 7-T NMR microimaging spectrometer (Varian Inc., CA, USA) with an external home-built active feedback device. All images were acquired with matrix = 128x128, FOV (field of view) = 30x30 mm, slice thickness = 1mm. T2*-weighted images were acquired at Ernst condition with flip angle = 26^o, TR = 150 ms, number of scan = 16 and various TE = 5~15 ms. For spin-echo T2-weighted images, TR = 7.5 s, TE = 10~50 ms. Inversion-recovery T1 and active feedback images were acquired with fast spin echo sequence with echo spacing = 10 ms, number of echo = 4, and TR = 7.5 s.

2.3 Result

2.3.1 Computer simulation

The spin dynamics described in “Theory” is first carried out by computer simulations (Fig. 2 and 3) to further illustrate and confirm the joint effect of “selective self-excitation” and “fixed-point dynamics”. The magnetic nanoparticle was modeled as a magnetized impenetrable

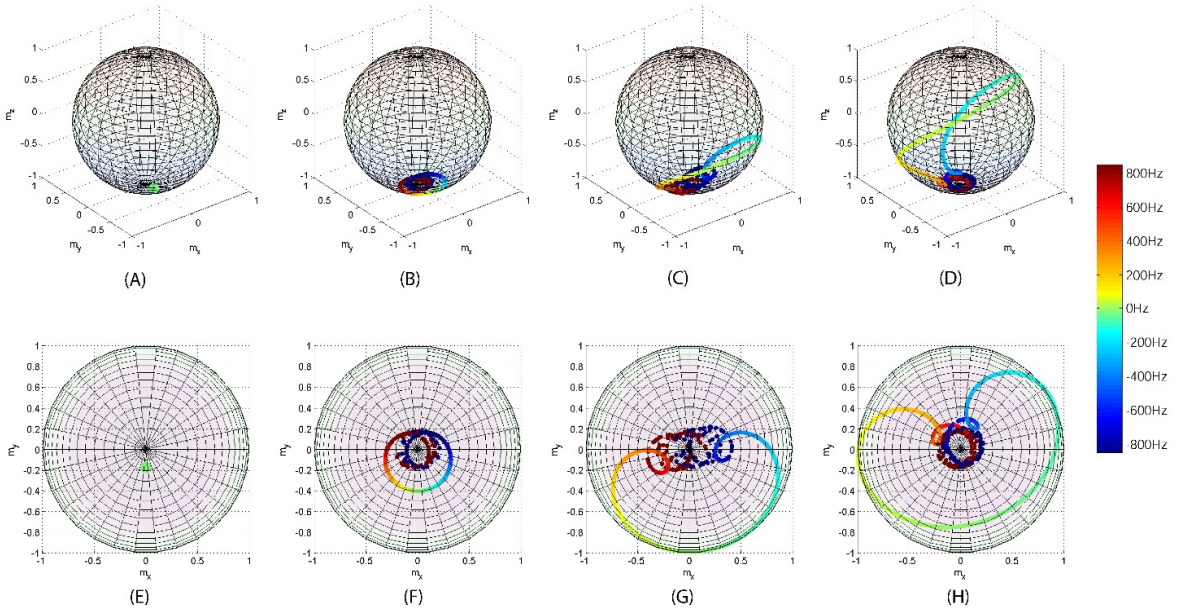

Figure 2. Computer simulations of the spin dynamics under the joint effect of "selective self-excitation" and "fixed-point dynamics" for magnetizations randomly located around a magnetic nanoparticle. The magnetic nanoparticle was modeled as a magnetized impenetrable sphere of 112 nm radius with volume fraction 1×10^{-5}. The time evolution of magnetizations were then shown by plotting their vector tips on a 3-D sphere (A) 0 ms, (B) 1 ms, (C) 3 ms, and (D) 5 ms after all the magnetizations are tilted by a big flip-angle (β=170°) RF pulse from the equilibrium position and then evolve under the active feedback fields. (E) to (H) are corresponding x-y plane projections.

sphere of 112 nm radius. The sphere was placed at the center of a cube with volume fraction equals 1×10^{-5}. Proton spins were located stochastically, and the z-component of the magnetic field experienced by each spin was calculated using Eq. (1). Following an initial 170° RF pulse, the magnetization evolutions of 2000 non-diffusing magnetic moments were calculated by numerical integration of the Bloch equation: $\partial \boldsymbol{m}(\boldsymbol{r},t)/\partial t = \boldsymbol{m}(\boldsymbol{r},t) \times \{ \boldsymbol{B}_{AF} + \Delta\omega(r)\mathbf{k} \}$, where $\Delta\omega(\boldsymbol{r}) \equiv \gamma B_{\mathrm{dip,z}}(\boldsymbol{r})$ represents the resonance offset from the rotating frame due to the dipolar field

induced by the super-paramagnetic nanoparticle [ref. Eq. (1)], **k** is the unit vector in z-axis, and $\boldsymbol{B}_{AF}$ is the active-feedback field [ref. Eq. (2)]. The time evolution of magnetizations were then shown by plotting their vector tips on a 3-D sphere, as shown in Fig. 2. The color of the dot shows the strength of the dipolar field experienced by the magnetizations due to the magnetic nanoparticle.

As shown in Fig. 2, the ^{1}H spins that are close to the magnetic nanoparticle experience high amplitude of dipolar field, while the ^{1}H spins that are distant from the magnetic nanoparticle (bulk water ^{1}H spins) experience a close-to-zero magnetic field. The feedback field with feedback phase 0^o exerts a torque to bring the magnetization back to the stable +z-axis at a rate proportional to the magnitude of the net transverse magnetization. Since bulk water dominates, the feedback field is mainly contributed from the bulk water ^{1}H. Based on the concept of selective excitation, it is then resonant better with the bulk water proton themselves and self-excites the bulk water magnetization more effectively, while the magnetization near magnetic nanoparticles is less affected.

Since the active feedback method acquires the z-magnetization when it reaches the fixed-point, the image is a spatial mapping of $|m_z(r)|$ at the acquisition time. Generally, m_z evolves from $m_z < 0$ (after the initial 170^o RF pulse) to $m_z > 0$ in time under the active feedback fields, as shown from Fig. 2A to Fig. 2D. At a specific evolution time, say 5ms in Fig. 2D, there is a spatial distribution of m_z values over space, depending on its spectral packet frequency relative to the bulk water's central frequency. If an active feedback image, $|m_z(r)|$, is acquired at this time, the voxels between $m_z(r) < 0$ and $m_z(r) > 0$ voxels will form signal voids. This is the physical origin for the dark voxels shown in Figs. 5 and 6.

Figure 3 also shows the time-dependent active feedback field, $B_{AF,+} \equiv B_{AF,x} + iB_{AF,y}$, and its power spectrum (i.e., Fourier Transform of the time-dependent active feedback field, $B_{AF,+} \equiv B_{AF,x} + iB_{AF,y}$) for the simulations shown in Fig. 2. The time-dependent active feedback field, $B_{AF,+} \equiv B_{AF,x} + iB_{AF,y}$, is calculated according to Eq. (2). As shown in Figs. 2 and 3, since the averaged transverse magnetization vector $\langle m_+(r,t) \rangle$ is mainly contributed from the bulk water ^{1}H magnetization, the resulting active feedback field generated by the active feedback device possesses a frequency much closer to the precession frequency of the bulk water ^{1}H that is far away from the dipole center. By "selective self-excitation", the feedback field self-excites the bulk water magnetization more effectively towards the +z-axis (assume feedback phase $\psi = 0^o$), while the ^{1}H magnetization near the dipole center is less affected due to resonance mismatch. This "selective self-excitation" process continues and enlarges the contrast between the longitudinal water ^{1}H magnetization in bulk water and that near the dipole center.

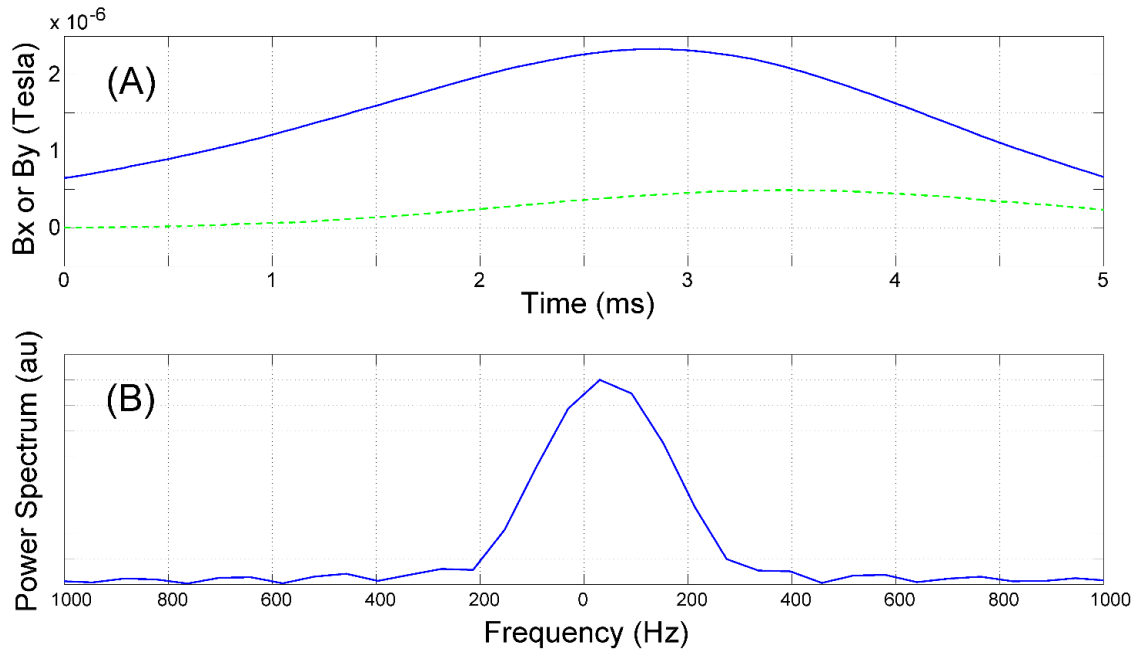

Figure 3. The time-dependent active feedback field, $B_{AF,+} \equiv B_{AF,x} + iB_{AF,y}$, (A) and its power spectrum (B) (i.e., Fourier Transform of the time-dependent active feedback field, $B_{AF,+} \equiv B_{AF,x} + iB_{AF,y}$) for the simulations shown in Fig. 2.

2.3.2 Controlled NMR experiments

To make the spin dynamics more clear, control experiments of NMR inversion recovery on methanol, CH_3OH, with and without active feedback fields were carried out to illustrate and confirm the joint effect of "selective self-excitation" and "fixed-point dynamics". The result is shown in Fig. 4. By setting the active feedback frequency at the Larmor frequency of CH_3, CH_3

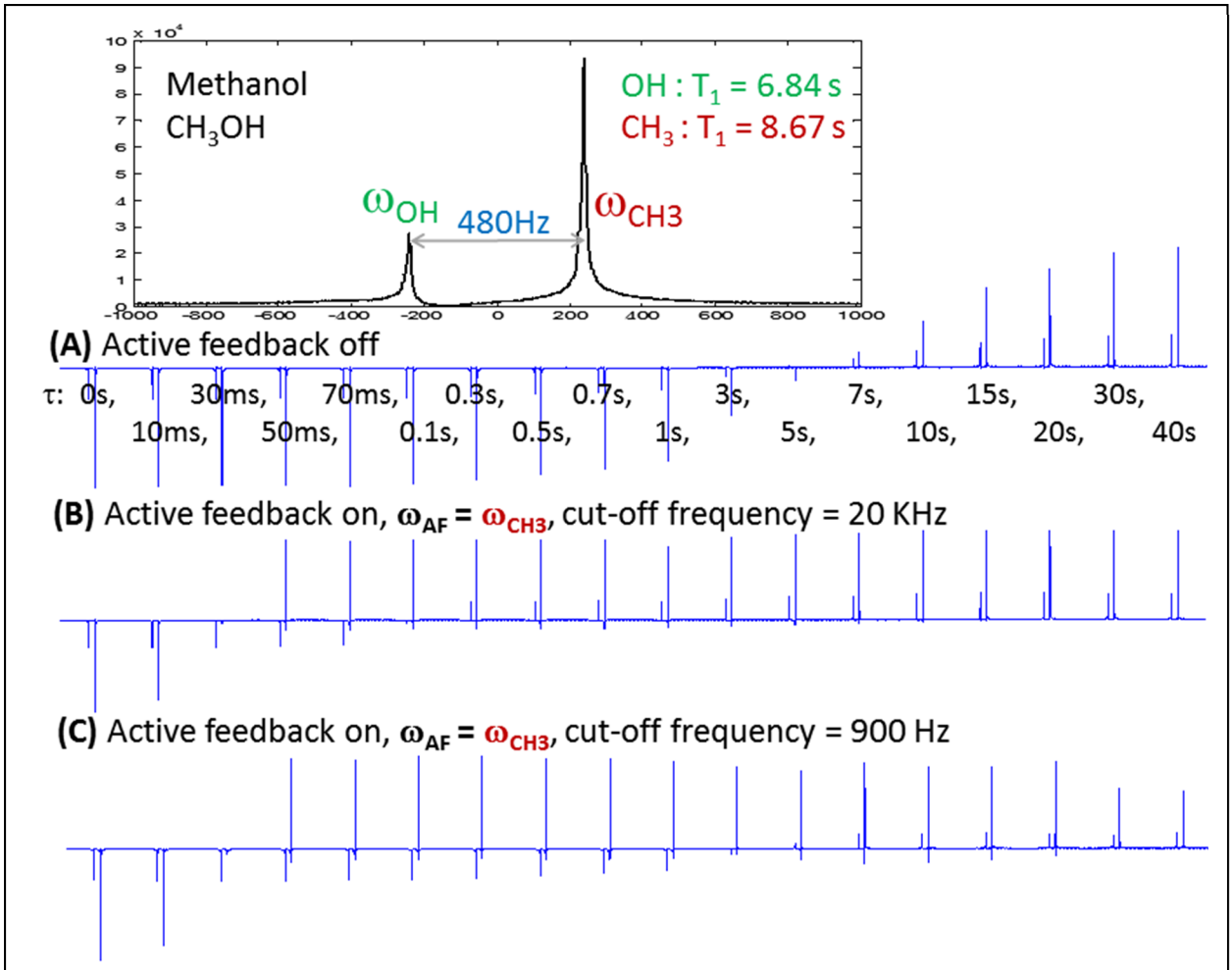

Figure 4. Control experiments of NMR inversion recovery on methanol, CH_3OH, (A) without (B) and (C) with active feedback fields to illustrate and confirm the joint effect of "selective self-excitation" and "fixed-point dynamics". Here the cut-off frequency of the low-pass filter used in the active-feedback electronic device is defined by a 3 dB attenuation of the output signal.

was selectively excited back to +z by its own active feedback fields much faster than OH, and then was locked in its fixed-point along +z. If the active feedback images were acquired, for example, at evolution time 50ms in Fig. 4B, significant contrast in chemical-shift images can be achieved. Such selective self-excitation becomes even more obvious when the bandwidth of the band-pass filter in the active feedback device becomes narrower, as shown in Fig. 4C.

2.3.3 Phantom MRI experiments

The spin dynamics described in "Theory" is confirmed by a phantom sample consisting of superparamagnetic nanoparticle aggregates in agar solution. Images of the absolute value of the longitudinal water ^{1}H magnetization, $|m_z(r)|$, at various evolution time under the active feedback fields with feedback phase $\Psi=180^o$ and feedback strength τ_{AF} = 1.2 ms are shown in Fig. 5. While the contrast develops continuously over time, the positive contrast of the water ^{1}H magnetization surrounding the dipole center is most obvious when the bulk water ^{1}H magnetization lies on the transverse plane (e.g., when evolution time τ = 7.5 ms). The void magnetization, $m_z(r) = 0$, around the dipole center shows that the longitudinal magnetization inside ($m_z(r) > 0$) and outside ($m_z(r) < 0$) the dark boundary possesses opposite signs. It is illustrated that active feedback imaging can sensitively and selectively highlight the different dipolar strength c [ref. Eq. (1)] corresponding to various sizes of superparamagnetic nanoparticle aggregates.

Sensitivity and contrast of the active feedback imaging to magnetic nanoparticles, compared with conventional T_2- and T_2*-weighted imaging, are shown in Fig. 6, using the same sample as in Fig. 5. The significantly larger VIS_{SIM} in Figs. 6D and 6E, due to larger spatial extent and contrast of the imaged dipolar field, reflects the superior "simulated visibility" in

imaging magnetic nanoparticle by active feedback MR than conventional T_2- and T_2*-weighted imaging.

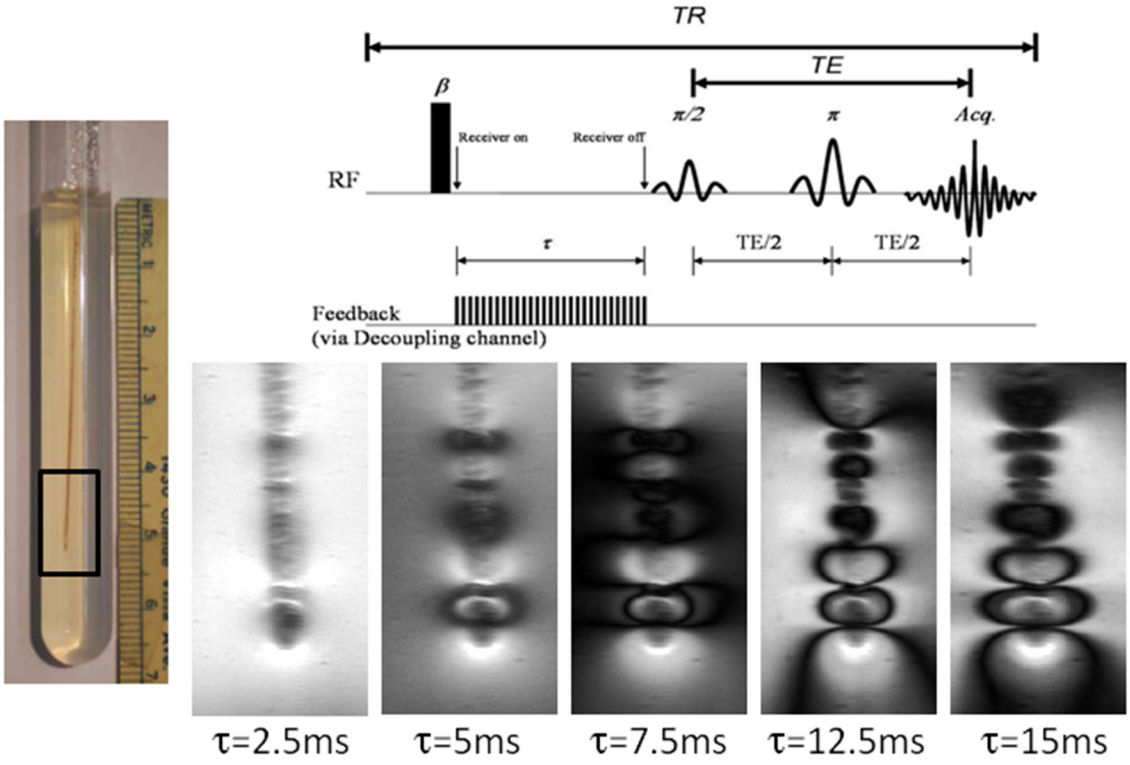

Figure 5. The active feedback pulse sequence for sensitive imaging of magnetic nanoparticles. Here shows the development of contrast in active feedback images, as demonstrated by a 10-mm cylindrical phantom sample consisting of agar with an inner capillary of 20-nm superparamagnetic nanoparticles with various degrees of aggregation. The parameters used in the pulse sequence are: initial RF pulse flip angle $\beta=10^{o}$, feedback strength τ_{AF} = 1.2 ms, and feedback phase $\psi = 180^{o}$ [ref. Eq. (2)]. The evolution time under the active feedback field, τ, is noted under the corresponding images.

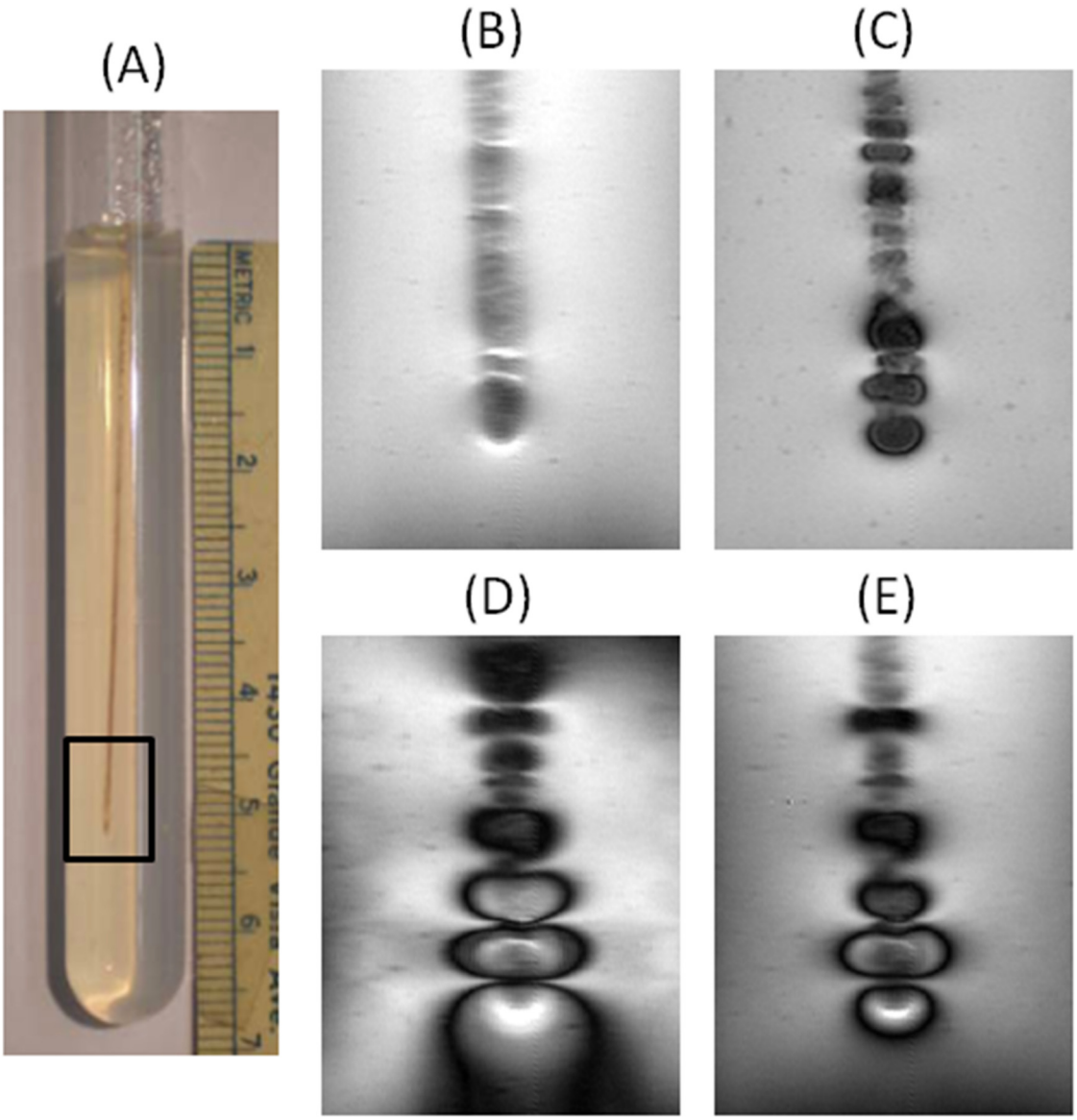

Figure 6. Sensitivity and contrast of the active feedback images to magnetic nanoparticles, compared with conventional T_2- and T_2*-weighted images, as demonstrated by a 10-mm cylindrical phantom sample consisting of agar with an inner capillary of 20-nm superparamagnetic nanoparticles with various degrees of aggregation, shown in (A). (B) T_2-weighted images acquired by spin-echo RARE pulse sequence. (C) T_2*-weighted images acquired by gradient-echo fast imaging (GEFI) pulse sequence. (D) and (E) Active feedback images acquired with feedback strength τ_{AF} =1.2 ms and 4.5 ms, respectively. The active feedback pulse sequence is shown in Fig. 5, followed by a spoiled gradient and spin-echo RARE acquisition (TE = 4.2 ms and TR = 10 s).

2.3.4 *In Vitro* MRI Experiments

Figure 7 shows the *in vitro* active feedback images of brain tissue removed from the left posterior parietal occipital lobe of a 6-year-old boy with glioblastoma multiforme. The active feedback image shows intense positive contrast in regions with greater concentrations of

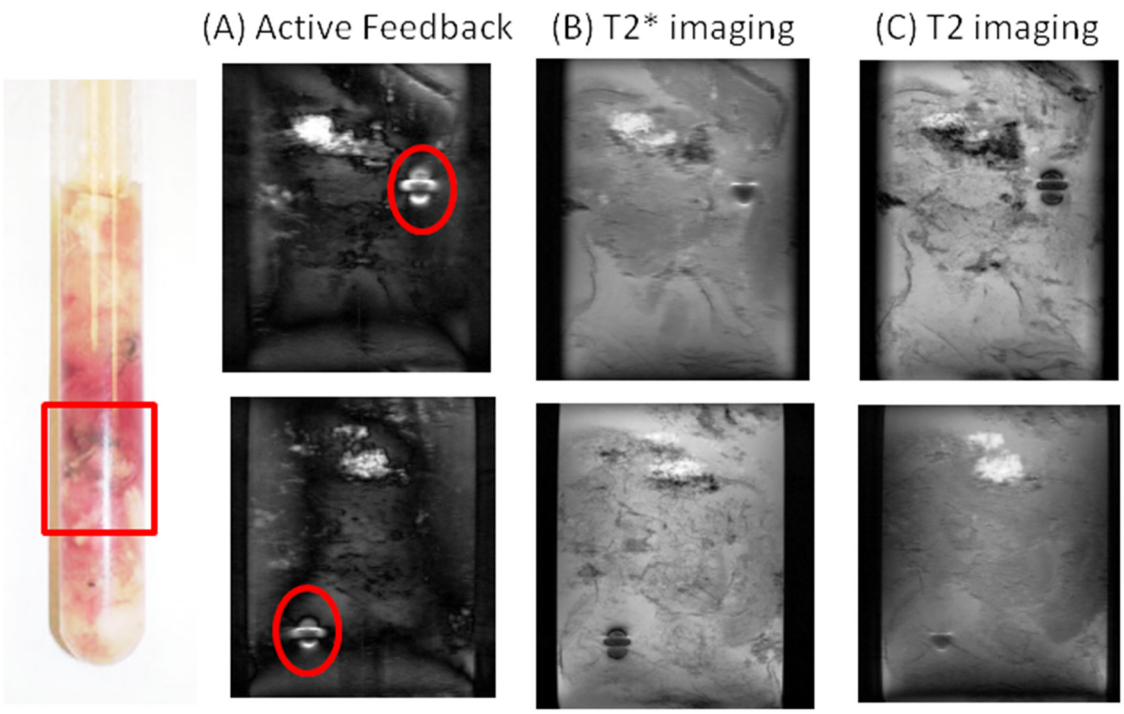

Figure 7. Demonstration of the potential applicability of the active feedback images for early stroke detection by lighting up the micro blood clots. Here show the active feedback images of *in vitro* brain tissue in a 10-mm tube excised from a patient undergoing intracranial surgery for glioblastoma multiforme, compared with conventional T_2- and T_2*-weighted images. (A) Active feedback images with feedback strength τ_{AF} =1.2 ms, evolution time τ = 10 ms, and the pulse sequence is shown in Fig. 5, followed by a spoiled gradient and RARE acquisition with TE = 10.2 ms and TR = 10 s. (B) T_2*-weighted images acquired by gradient-echo fast imaging (GEFI) pulse sequence. (C) T_2-weighted images acquired by spin-echo RARE pulse sequence.

deoxyhemoglobin from blood clots, consistent with the darker regions in the $T2^*$-weighted and T2-weighted images corresponding to increased dephasing.

2.3.5 *In Vivo* MRI Experiments

Mouse models injected with human colon cancer cell line COLO 205 were imaged. Representative results are shown in Figs. 8 and 9. As a control, the tumor at right flank is labeled with magnetic nanoparticles, while the other is not. ROIs that represent muscles, unlabeled tumor, and labeled tumor are first defined (Fig. 8A). The existence and distribution of magnetic nanoparticles is confirmed by Perls' Prussian blue iron-stain histology. Active feedback image intensity, acquired with initial RF flip angle $\beta=170^o$ and feedback phase $\psi = 0^o$, for various active feedback evolution time τ is fitted by T_1 inversion recovery formula to detect the existence and significance of "selective self-excitation" at the locations of muscles, SPIO-labeled tumor, and unlabeled tumor. As described in "Theory", due to resonance mismatch, the SPIO-labeled tumor at right flank can resist "selective self-excitation" from the active feedback fields generated by the bulk water and the active feedback device. Therefore, the dynamics of its longitudinal magnetization is mainly T_1 relaxation with a longer T_1 time (as there is no "selective self-excitation" to help rotate the magnetization back to +z) and higher T_1 fitting-correlation-coefficient (as the dynamics is well described by T1 inversion recovery). On the other hand, for muscles and unlabeled tumors, "selective self-excitation" rapidly rotates the bulk water magnetization back to the stable +z fixed-point with $\psi = 0^o$ (as if T1 is short), creating spin dynamics very different from simple T1 inversion recovery (lower T1 fitting correlation coefficient). While conventional T_2* parameter mapping (Fig. 9A) and T_2 parameter mapping (Fig. 9B) can hint at the location of the SPIO-labeled tumor, the T_1 parameter mapping and

fitting-correlation-coefficient mapping (Fig. 9D) from active feedback images clearly highlight the tumor mass with a close correlation of the size with iron-stain histopathology.

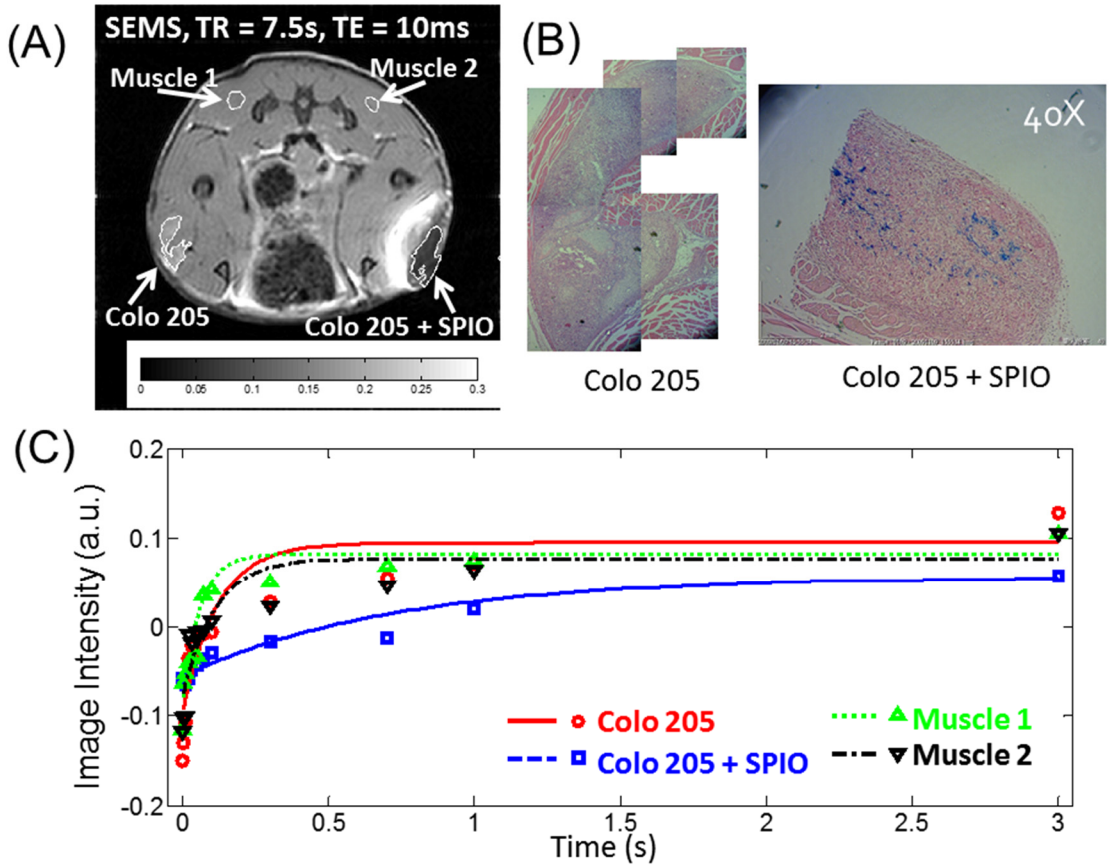

Figure 8. *In vivo* images of human colon cancers (COLO 205 human colon adenocarcinoma cell line) from nude mouse xenografts with magnetic nanoparticles (SPIO) labeled tumor cells at right flank and unlabeled tumor at left flank. (A) Locations of the selected ROIs representing muscles, unlabeled tumor, and labeled tumor. (B) Histological section of both tumors at left and right flanks with Perls' Prussian blue to confirm the existence and distribution of SPIO. (C) Image intensity of active feedback imaging at various ROIs and active feedback evolution time (τ in the active feedback pulse sequence in Fig. 5), as fitted by T_1 inversion recovery formula, $m_z(t) = 1 - 2*\exp(-t/T_1)$, to examine the extra contributions of "selective self-excitation" by active feedback fields in regions without SPIO to rotate the magnetization back to +z. Also see caption in Fig. 9.

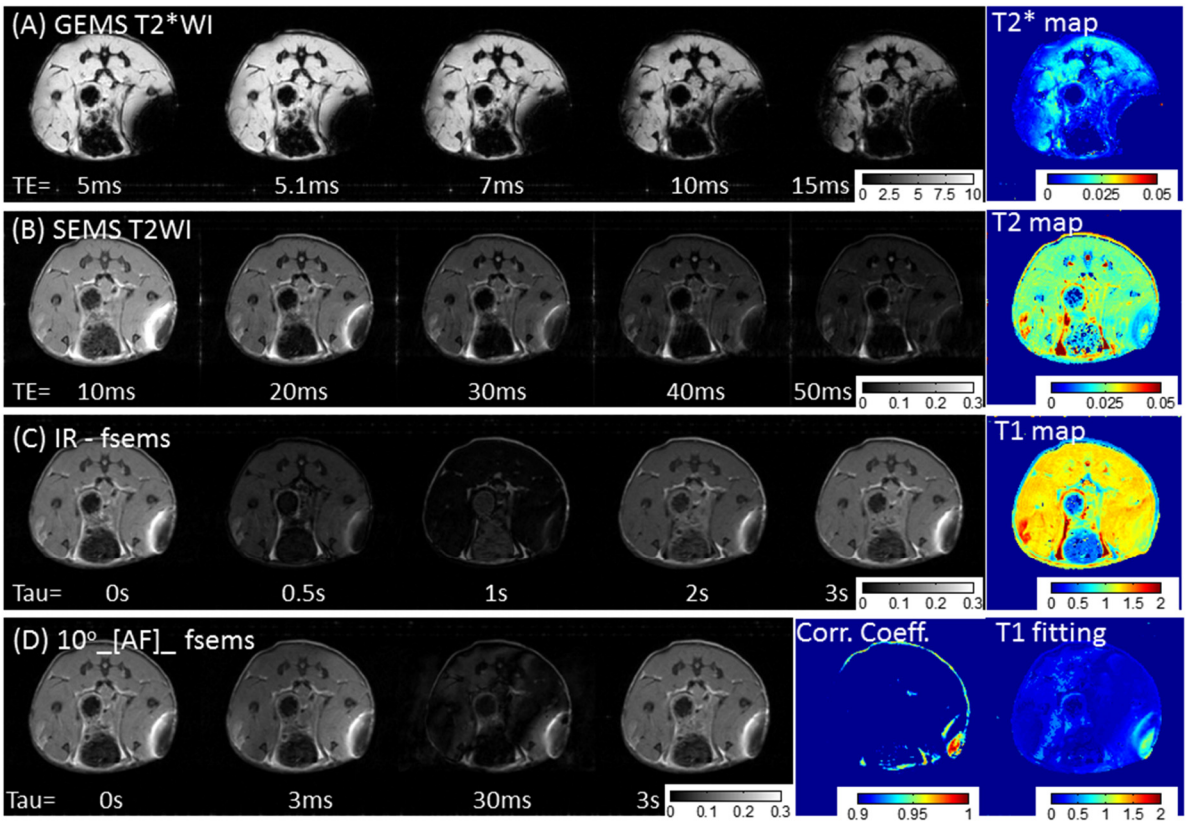

Figure 9. *In vivo* images and parameter mapping of human colon cancers (COLO 205 human colon adenocarcinoma cell line) from nude mouse xenografts with magnetic nanoparticles (SPIO) labeled tumor cells at right flank and unlabeled tumor at left flank, FOV = 3 cm × 3 cm, and thickness = 1 mm. (A) T_2*-weighted image and T_2* parameter mapping. (B) T_2-weighted image and T_2 parameter mapping. (C) Inversion recovery T_1-weighted image and T_1 parameter mapping. (D) Active-feedback image, T_1 parameter mapping, and fitting-correlation-coefficient mapping (colorbar 0.9-1).

Early-stage tumors are characterized by the formation of extensive new blood vessels to supply tumors with oxygen and nutrients. Hemoglobin, which is composed of heme and iron, is the major chemical component of red blood cells and blood. Consequently, the capability to sensitively image magnetic nanoparticles and aggregates may by itself improve the detection of

cancers without external magnetic-nanoparticle labeling. This is demonstrated in mouse colon cancer models without magnetic-nanoparticle labeling, imaged on a 7-T wide-bore magnet using a home-built active feedback device and a small animal monitoring system (Fig. 10). During the image acquisition, the pulse sequence parameters were optimized to ensure that each method is performing to maximal contrast-to-noise ratio (CNR) between the colon cancer and its surrounding healthy shank muscle tissue. The CNR is estimated to be +1.8 (Fig. 10B, T_1-weighted image), +3.2 (Fig. 10C, T_2-weighted image), -0.8 (Fig. 10D, T_2*-weighted image), and +16.1 (Fig. 10E, active-feedback image). While the proton dentistry, T_1-weighted, T_2-weighted, and T_2*-weighted images show no indication of a tumor, the active-feedback method is successful in highlighting the tumor mass with a close correlation of the size with histopathology (Fig. 10G).

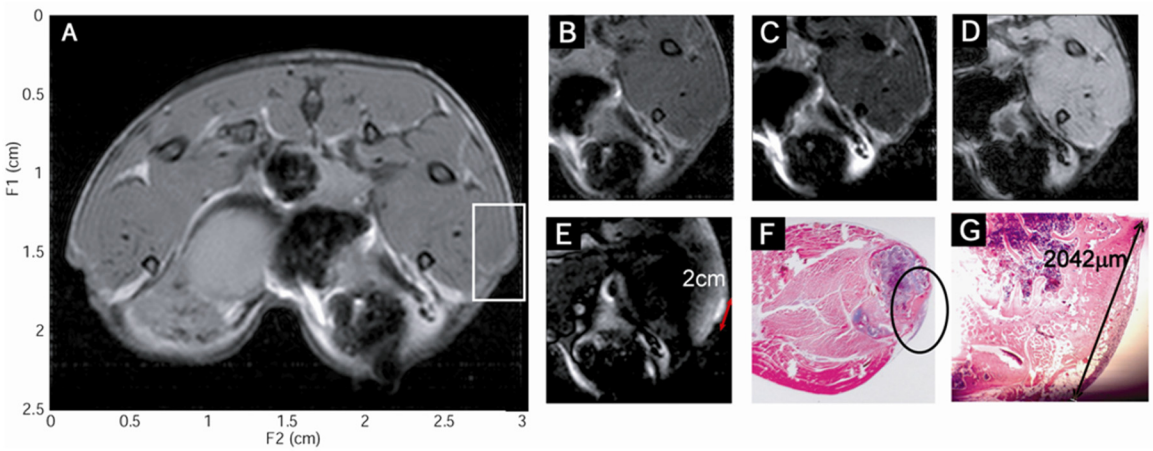

Figure 10. *In vivo* images of human colon cancers (COLO 205 human colon adenocarcinoma cell line) from nude mouse xenografts without magnetic-nanoparticle labeling, FOV = 3 cm × 3 cm, and thickness = 1 mm. (A) Proton density image. (B) T_1-weighted image. (C) T_2-weighted image. (D) T_2*-weighted image. (E) Active-feedback image. (F) Histopathology with section of colon cancers circled. (G) Magnified region of interest containing tumor mass.

2.4 Discussion

The observed contrast by selective self-excitation and fixed-point dynamics under active feedback fields can also be understood by considering the dependence of this contrast mechanism on the frequency offsets of different water ^{1}H frequency components (also called "spectral packets") as well as the relative contribution of each frequency component to the total magnetization, as applied to a dipolar field distribution. Such dipolar fields taper off quickly as a function of $1/r^3$ and span several voxels. Consequently, magnetization in the immediate vicinity of the dipole experiences a larger frequency shift and wider distribution of resonance frequencies, compared with the smaller shift and narrower distribution of frequencies for magnetization farther from the center of the dipole. Following a 10° RF pulse, the magnetization farther away from the dipole center is nutated by the active feedback field (with feedback phase $\Psi=180^o$) toward $-z-$axis more quickly, crossing the transverse plane earlier. On the other hand, the magnetization closer to the dipole center experiences significantly different field strength and is much less excited by the dynamics under active feedback fields. The resulting absolute-value longitudinal-magnetization image, $|m_z(r)|$, thus displays the magnetization surrounding the dipole as regions of bright contrast with darkened boundary, as shown in Figs. 5 and 6.

Active feedback excitation differs fundamentally from externally applied RF pulses in that the interplay between the magnetization and the feedback fields allows the spins to direct their own evolution. For examples, selective self-excitation and fixed-point dynamics under active feedback fields show promises in generating enhanced, robust, and positive contrast, reflecting microscopic field variations such as those induced by local dipolar fields, e.g., in cells labeled with superparamagnetic nanoparticles. This is in distinction to the negative contrast seen in T_2-weighted or T_2*-weighted images, which can hinder the direct evaluation of surrounding

tissues and discrimination between target molecules/cells and susceptibility artifacts. As active feedback fields can be viewed as selective RF fields generated by the magnetization itself, mediated through coupling with the receiver coil and then controlled by the electronic feedback circuits, the feedback fields may be used to highlight off-resonance water ^{1}H magnetization surrounding a dipole to yield more detailed, bright contrast, as demonstrated experimentally on aggregates of superparamagnetic nanoparticles (Figs. 5 and 6), on blood clots in freshly excised brain tissue (Fig. 7), on SPIO-labeled colon cancers (Figs. 8 and 9), and on extra hemoglobin from the formation of extensive new blood vessels in early-stage tumors (Fig. 10).

Compared with other positive-contrast magnetic-nanoparticle imaging methods, the major advantages of the active-feedback method are three folds. First, the dynamics of selective self-excitation and fixed-point dynamics under active feedback fields can resist distortions to image contrast due to broad bulk water linewidth, while remaining sensitive to microscopic, intra-voxel field variations originating from internal, tissue-specific sources. This feature is particularly important for MRI where significant macroscopic field variation is present due to statistic field inhomogeneity and/or susceptibility variations across the sample. After a small flip-angle RF pulse tilts the bulk water magnetization, The spectral packets of the bulk water which are further away from its central frequency dephase more rapidly in a rotating frame with frequency equal to the central frequency of the bulk water. Consequently, at a later time, the feedback field is mainly contributed from the spectral packets near the central frequency of the bulk water, resulting in narrower bandwidth of selective self-excitation. Repetition of this process essentially converges the selection excitation profile to a δ-like function sitting at bulk water's central frequency. The sensitivity of the active feedback field to microscopic, intra-voxel frequency variations in the presence of broad bulk water linewidth also depends on the time-

scale over which the feedback field acts relative to the time-scale on which the bulk water begins to dephase. Consequently, stronger active-feedback field (i.e., shorter τ_r) can improve the contrast of voxels with stronger local gradients (e.g., from magnetic nanoparticles, as shown in Figs. 5 and 6), while weaker active-feedback field (i.e., longer τ_r) can help optimize the contrast of voxels with weaker local gradients (e.g., from blood hemoglobin, as shown in Fig. 7). Second, active-feedback imaging is experimentally robust. The spin dynamics freezes in time and the optimal contrast in z-magnetization gets locked when the bulk water ^{1}H magnetization reaches the fixed point along the –z-axis (with $\Psi=180^o$) and therefore diminish the active feedback fields. Third, the contrast in m_z originates from various degree of nutation, not saturation, from -z to +z by selective self-excitation, which makes possible contrast enhancement even in the "motion narrowing regime" where average diffusion length is comparable or larger than the SPIO size and spectral packets exchange rapidly to make lock-in saturation infeasible.

2.5 Conclusion

In conclusion, active feedback fields generated by electronic devices not only extend the applicability of the feedback-enhanced contrast enhancement to low-field MRI conditions, but also provide added flexibility by altering the functional dependence of the feedback fields on the averaged transverse magnetization. The device is to filter, phase shift, and amplify the signal from the receiver coils and then retransmit the modified signal into the RF transmission coil, with adjustable and programmable feedback phases, ψ, and gains, τ_{AF} [ref. Eq. (2)].

As such, active feedback fields introduce a conceptually new approach to practicing magnetic resonance by adding a new line to the pulse sequences and by allowing for additional control over the spin dynamics. For example, the spin dynamics originated from selective self-

excitation and fixed-point dynamics under active feedback fields have been shown to be sensitive to dipolar fields generated by magnetic nanoparticles. Phantom, *in vitro*, and *in vivo* experimental results indicate that this approach generates enhanced, robust, and positive contrast, reflecting microscopic field variations induced by strong local dipole fields, such as those created by superparamagnetic nanoparticles or iron-containing molecular aggregates.

2.6 Reference

[1] Kim D, Hong KS, Song J. The present status of cell tracking methods in animal models using magnetic resonance imaging technology. Mol Cells 2007; 23: 132–137.

[2] Jellinger K, Paulus W, Grundke-Iqbal I, Riederer P, Youdim MB. Brain iron and ferritin in Parkinson's and Alzheimer's diseases. J Neural Transm Park Dis Dement Sect. 1990; 2: 327-340.

[3] Kimberly WT, Wu O, Arsava EM, Garg P, Ji R, Vangel M, Singhal AB, Ay H, Sorensen AG. Lower hemoglobin correlates with larger stroke volumes in acute ischemic stroke. Cerebrovasc Dis Extra. 2011; 1: 44–53.

[4] Cunningham CH, Arai T, Yang PC. Positive contrast magnetic resonance imaging of cells labeled with magnetic nanoparticles. Magn Reson Med 2005; 53: 999-1005.

[5] Zurkiya O, Hu X. Off-resonance saturation as a means of generating contrast with superparamagnetic nanoparticles. Magn Reson Med 2006; 56: 726-732.

[6] Seppenwoolde JH, Viergever MA, Bakker CJ. Passive tracking exploiting local signal conservation: the white marker phenomenon. Magn Reson Med 2003; 50: 784-790.

[7] Mani V, Briley-Saebo KC, Itskovich VV. Gradient echo acquisition for superparamagnetic particles with positive contrast (GRASP): sequence characterization in membrane and glass

superparamagnetic iron oxide phantoms at 1.5 T and 3 T. Magn Reson Med 2006; 55: 126-135.

[8] Lin YY, Lisitza N, Ahn S, Warren WS. Resurrection of crushed magnetization and chaotic dynamics in solution NMR spectroscopy. Science 2000; 290: 118-121.

[9] Huang SY, Wolahan SM, Mathern GW, Chute DJ, Akhtari M, Nguyen ST, Huynh MN, Salamon N, Lin YY. Improving MRI differentiation of gray and white matter in epileptogenic lesions based on nonlinear feedback. Magn Reson Med 2006; 56: 776-786.

[10] Datta S, Huang SY, Lin YY. Contrast enhancement by feedback fields in magnetic resonance imaging. J. Phys. Chem. B 2006; 110: 22071-22078.

[11] Datta S, Huang SY, Lin YY. The transient dynamics leading to spin turbulence in high-field solution magnetic resonance: a numerical study. J Chem Phys 2006; 124: 154501.

[12] Huang SY, Furuyama JK, Lin YY. Designing feedback-based contrast enhancement for in vivo imaging. Magn Reson Mater Phy 2006; 19: 333-346.

[13] Datta S, Huang SY, Lin YY. Understanding spin turbulence in solution magnetic resonance through phase space dynamics and instability. Concepts Magn Reson 2006; 28A: 410-421.

[14] Huang SY, Chung AP, Lin YY. Visualizing feedback-enhanced contrast in magnetic resonance imaging. Concepts Magn Reson 2007; 30A: 378-393.

[15] Huang SY, Yang SS, Lin YY. Sensitivity of feedback-enhanced MRI contrast to macroscopic and microscopic field variations. Magn Reson Med 2009; 61: 925-936.

[16] Broekaer P, Jeener J. Suppression of radiation damping in NMR in liquids by active electronic feedback. J Magn Reson A 1995; 113: 60-64.

[17] Warren WS, Hammes SL, Bates JL. Dynamics of radiation damping in nuclear magnetic resonance. J Chem Phys 1989; 91: 5895-5904.

[18] Augustine MP. Transient properties of radiation damping. Prog Nucl Magn Reson Spectrosc 2002; 40: 111-150.

[19] Khitrin AK, Jerschow A. Simple suppression of radiation damping. J Magn Reson 2012; 225: 14-16.

[20] Krishnan VV, Murali N. Radiation damping in modern NMR experiments: progress and challenges. Prog Nucl Magn Reson Spectrosc 2013; 68: 41-57.

[21] Huang SY, Anklin C, Walls JD, Lin YY. Sizable concentration-dependent frequency shifts in solution NMR using sensitive probes. J Am Chem Soc 2004; 126: 15936-15937.

[22] Walls JD, Huang SY, Lin YY. Excitation of magnetization using a modulated radiation damping field. J. Phys. Chem. B 2006; 110: 19985-19989.

[23] Walls JD, Huang SY, Lin YY. Spin amplification in solution magnetic resonance using radiation damping. J. Chem. Phys. 2007; 127: 054507.

[24] Hennig J, Nauerth A, Friedburg H. RARE imaging - a fast imaging method for clinical MR. Magn Reson Med 1986; 3: 823-833.

[25] Haase A, Frahm J, Matthaei D, Hänicke W, Merboldt KD. FLASH imaging: rapid NMR imaging using low flip-angle pulses. J Magn Reson 2011; 213:533-41.

[26] Boxerman JL, Hamberg LM, Rosen BR, Weisskoff RM. MR contrast due to intravascular magnetic susceptibility perturbations. Magn Reson Med 1995; 34: 555-566.

Chapter 3

Active Feedback MR for Early Lesion Imaging

3.0 Abstract

Noninvasive contrast in conventional magnetic resonance imaging (MRI) is often limited by the dependence of the magnetization on intrinsic MR parameters that may not vary significantly throughout the sample. We demonstrate a new method for enhancing MRI contrast due to slight variations in endogenous MR parameters, with applications in improved differentiation between diseased and healthy tissue. This amplification scheme exploits two emergent nonlinear feedback interactions, radiation damping and the distant dipolar field. Instability of the magnetization configuration under the individual or joint feedback fields provides avalanching amplification of MRI contrast sensitive to small spin density or resonance frequency differences that are not detectable by conventional MRI techniques. Feedback-based contrast enhancement is demonstrated in phantoms and *in vitro* brain tissue excised from epileptogenic lesions and tumors, suggesting applications in improved tissue characterization and assessment of epilepsy and cancer.

3.1 Introduction

The ability to generate adaptable soft-tissue contrast without ionizing radiation is one of magnetic resonance imaging's (MRI) greatest strengths. In particular, intrinsic or endogenous contrast renders MRI noninvasive while allowing visualization of virtually all tissue anatomies. However, limitations in endogenous contrast can pose challenges to the early detection of

diseases like cancer by MRI [1]. If the underlying pathology only causes a slight change in the corresponding MR parameters, conventional MRI methods may not be able to distinguish between diseased and neighboring normal tissues. Delineating the exact extent of lesions is especially important, for example, in epileptogenic diseases requiring careful identification of the affected tissue prior to resective surgery [2]. A new approach to enhancing endogenous MR contrast would thus aid in the improved characterization and treatment of such diseases.

Here, we develop nonlinear feedback interactions known to emerge in aqueous media into flexible, general contrast enhancement mechanisms sensitive to versatile endogenous MR contrast sources. These feedback fields include radiation damping-like [3] active feedback field and the distant dipolar field (DDF) [4]. Under the individual or joint feedback fields, contrast enhancement may be triggered by the smallest changes in the magnetization distribution to reflect the underlying MR parameters and is thus referred to as avalanching amplification. Avalanching amplification of MRI contrast due to slight variations in MR parameters, such as proton density and resonance frequency, is demonstrated and applied to characterize brain lesions involved in epilepsy and cancer.

3.2 Theory and Method

The physical origin of contrast in MRI can be understood through the classical formulation of spin dynamics in liquids, known as the Bloch equations. In a rotating frame precessing with the Larmor frequency $\omega_0=\gamma B_0$ (γ is the gyromagnetic ratio and B_0 is the magnetic flux density of an external Zeeman field along the z-axis), the dynamics of the normalized magnetization, $\boldsymbol{m}(\boldsymbol{r},t) \equiv \boldsymbol{M}(\boldsymbol{r},t)/M_0$, ($M_0$ is the equilibrium magnetization) in a voxel at position $\boldsymbol{r}$ can be described as

$$\frac{\partial \boldsymbol{m}(\boldsymbol{r},t)}{\partial t} = \gamma \boldsymbol{m}(\boldsymbol{r},t) \times \left[\frac{\delta\omega(\boldsymbol{r})}{\gamma} \hat{\boldsymbol{z}} + \boldsymbol{B}(\boldsymbol{r},t) \right] - \frac{m_x(\boldsymbol{r},t)\hat{\boldsymbol{x}} + m_y(\boldsymbol{r},t)\hat{\boldsymbol{y}}}{T_2} - \frac{m_z(\boldsymbol{r},t) - 1}{T_1} \hat{\boldsymbol{z}} + D\nabla^2 \boldsymbol{m}(\boldsymbol{r},t) \qquad (1)$$

where $\delta\omega \equiv \omega - \omega_0$ is the resonance offset, $\boldsymbol{B}(\boldsymbol{r},t)$ represents the effective field, T_1 and T_2 are the longitudinal and transverse relaxation times, respectively, D is the diffusion coefficient, and $\{\hat{\boldsymbol{x}}, \hat{\boldsymbol{y}}, \hat{\boldsymbol{z}}\}$ are the Cartesian basis vectors. MRI contrast arises from the dependence of $\boldsymbol{m}(\boldsymbol{r},t)$ on the MR parameters in Eq. (1). Pulse sequence parameters, such as pulse excitation profiles or variable delays, may be flexibly engineered to impart weighting on $\boldsymbol{m}(\boldsymbol{r},t)$ for specific MR properties or combinations of properties. Still, the contrast provided by conventional MRI sequences is often limited by the explicit dependence of $\boldsymbol{m}(\boldsymbol{r},t)$ on MR parameters that may not vary significantly throughout the sample.

On the other hand, the dependence of $\boldsymbol{m}(\boldsymbol{r},t)$ on specific MR properties may be heightened if the local field $\boldsymbol{B}(\boldsymbol{r},t)$ becomes a function of $\boldsymbol{m}(\boldsymbol{r},t)$, rendering Eq. (1) nonlinear. For solutions at high field with abundant high-γ nuclei, e.g., ^{1}H, magnetization-dependent contributions to $\boldsymbol{B}(\boldsymbol{r},t)$ mainly come from the distant dipolar field (DDF), $\boldsymbol{B}_d(\boldsymbol{r},t)$, and/or the radiation damping field, $\boldsymbol{B}_r(t)$. Under these feedback fields (also called reaction fields), a simple pulse sequence prepares the magnetization in an unstable configuration. Subsequent evolution of $\boldsymbol{m}(\boldsymbol{r},t)$ under the MR parameters generates small variations in the magnetization distribution that are fed back to $\boldsymbol{m}(\boldsymbol{r},t)$ through $\boldsymbol{B}(\boldsymbol{r},t)$. $\boldsymbol{B}(\boldsymbol{r},t)$ acts on $\boldsymbol{m}(\boldsymbol{r},t)$ to bring it away from its initial unstable state with ever-increasing efficiency, such that differences in $\boldsymbol{m}(\boldsymbol{r},t)$ across the sample are amplified in a positive feedback cycle. Such "avalanching amplification" of MRI contrast under $\boldsymbol{B}_d(\boldsymbol{r},t)$, $\boldsymbol{B}_r(t)$, and their joint action is shown through numerical simulations of simple phantoms in Fig. 1 (following the method in [15] while neglecting T_1, T_2, and diffusion processes for simplicity) and explained as follows. Feedback-based contrast enhancement is then demonstrated

experimentally in Figs. 2-4 for *in vitro* human brain tissue samples excised from epileptogenic and cancerous lesions.

The first feedback field, the DDF, arises from long-range residual dipolar couplings that survive motional averaging in solution [8]. In liquids, diffusion only averages out dipolar couplings between spins separated by distances less than the average diffusion length, typically microns on the solution MR time scale (~s). Due to the angular dependence of the dipolar interaction, the vector sum of the DDF from uniform magnetization in a spherical sample vanishes. This spherical symmetry can be broken, however, by sample geometry or spatial modulation of the magnetization by gradients, thereby reintroducing the DDF. Under the strong external magnetic fields used in MR imaging and spectroscopy, $\boldsymbol{B}_d(\boldsymbol{r}, t)$ can be approximated as (*Deville 1979*):

$$\gamma \boldsymbol{B}_d(\boldsymbol{r},t) = \frac{1}{4\pi\tau_d}\int d^3\boldsymbol{r}' \frac{3\cos^2\theta_{rr'}-1}{2\,|\boldsymbol{r}-\boldsymbol{r}'|^3}\left[3m_z(\boldsymbol{r}',t)\hat{\boldsymbol{z}} - \boldsymbol{m}(\boldsymbol{r}',t)\right], \quad \tau_d = \frac{1}{\gamma\mu_0 M_0}\,(\text{SI units}) \qquad (2)$$

where $\cos\theta_{rr'}=(z-z')/|\boldsymbol{r}-\boldsymbol{r}'|$. The characteristic DDF time constant τ_d is approximately 65 ms for pure water at 14.1 T and 300 K. While $\boldsymbol{B}_d(\boldsymbol{r},t)$ is a global microscopic reaction field [3], for magnetization that is fully modulated along a single spatial direction $\boldsymbol{s}$, $\boldsymbol{B}_d(\boldsymbol{r},t)$ becomes a function of the local magnetization $\boldsymbol{m}(s,t)$, where $s \equiv \boldsymbol{r}\cdot\hat{\boldsymbol{s}}$ (in SI units) [9]:

$$\gamma \boldsymbol{B}_d(s,t) = \frac{1}{4\pi\tau_d}\Delta_s \begin{pmatrix} \frac{1}{3}\left[m_x(s,t) - \langle m_x\rangle\right] \\ \frac{1}{3}\left[m_y(s,t) - \langle m_y\rangle\right] \\ -\frac{2}{3}\left[m_z(s,t) - \langle m_z\rangle\right] \end{pmatrix}, \quad \Delta_s = \frac{\left[3(\boldsymbol{s}\cdot\boldsymbol{z})^2 - 1\right]}{2}. \qquad (3)$$

The DDF has been shown to produce dynamical instabilities in liquids [5]. Here, we apply the instability of the DDF to generate enhanced contrast between regions with small differences in spin density. Consider a simple, concentric cylindrical phantom containing water with a slight

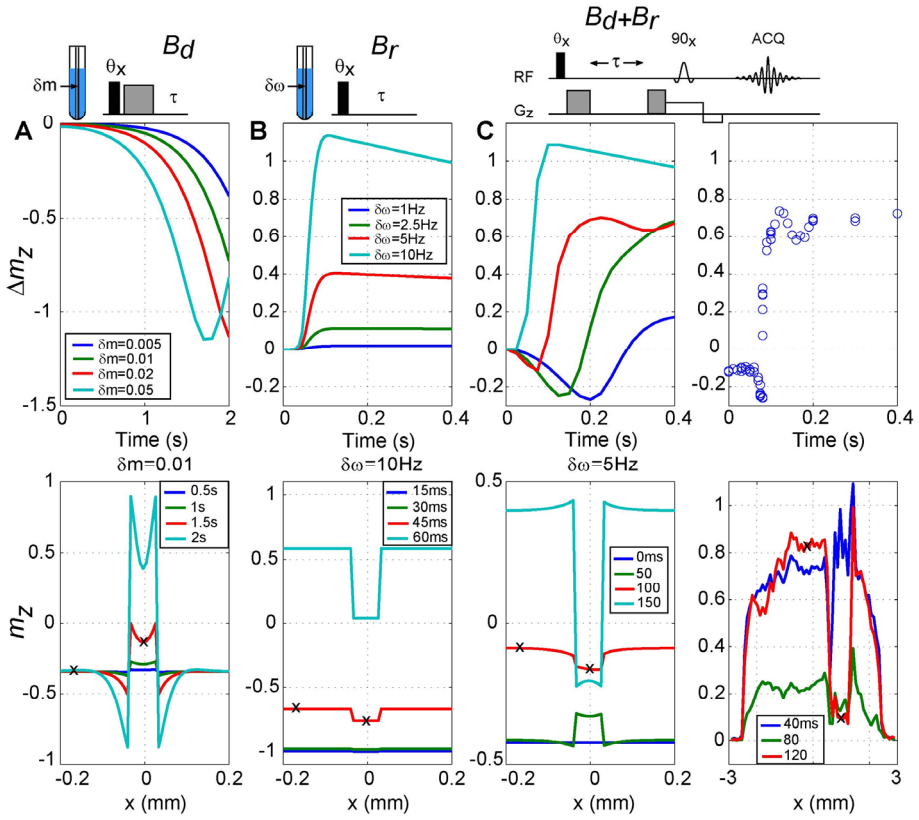

Figure 1. Avalanching amplification of MRI contrast by the individual and joint feedback fields of radiation damping ($\boldsymbol{B}_r$) and the DDF ($\boldsymbol{B}_d$), demonstrated in simple phantoms. (A) DDF only, with spin density difference δm in the inner region. θ=110°, $(GT)_z$=5G·ms/cm. Top: Contrast Δm_z, defined as the difference in m_z between representative voxels taken from the two regions, marked by "x" in the bottom figure. Bottom: Cross-sections of m_z averaged along the z-axis, corresponding to the line of magnetization in the x-direction located midway across the y-axis. (B) Radiation damping only, with resonance frequency difference $\delta\omega$. θ=179°. (C, left) Joint reaction fields, with resonance frequency difference $\delta\omega$. θ=95° ($\delta\omega$=1 Hz), 100° ($\delta\omega$=2.5 Hz), 115° ($\delta\omega$=5 Hz), 179° ($\delta\omega$=10 Hz), using the pulse sequence shown in (A). Legend for top figure is the same as in (B). For the bottom figure, θ=115°, $\delta\omega$=5 Hz. (C, right) Experimental results showing contrast enhancement under the joint reaction fields for water in a 5 mm tube with a 1-mm inner capillary containing 5% ethanol solution.

difference in proton density, δm, between the inner and outer compartments (Fig. 1A), used to

model differences in water content between distinct tissues. Dynamics were simulated by numerically integrating the nonlinear Bloch equations without relaxation and diffusion effects (τ_r = 10 ms, τ_d = 69 ms). Phantom sample was 0.47^3 mm^3 sampled by 64×64×16 points. Diameter of inner region was 0.073 mm, sampled by 10 voxels across. The details of the numerical simulation are described in reference [15]. Phantoms are modeled by ^{1}H from water in the outer region (spin density $|\boldsymbol{m}(\boldsymbol{r},t=0)|$=1, resonance offset $\delta\omega$=0) and ^{1}H with a slight difference in MR properties in the inner region. Experimental pulse sequence is shown in (C), where θ=120°, GT=5G·ms/cm for the first gradient (second gradient is a spoil gradient), and echo-planar imaging (FID mode) was used to image the sample (128×128 voxels).

Following the preparation sequence $[\theta_x\text{-}(GT)_z]$, the transverse magnetization vectors $\boldsymbol{m}_+(\boldsymbol{r},t)\equiv m_x(\boldsymbol{r},t)+\mathrm{i}m_y(\boldsymbol{r},t)$ are modulated along the z-axis in a helical configuration. For samples with uniform proton density, following the z-gradient, $\boldsymbol{m}_+(\boldsymbol{r},t)$ is aligned with $\boldsymbol{B}_{d,+}(\boldsymbol{r},t)\equiv B_{d,x}(\boldsymbol{r},t)+\mathrm{i}B_{d,y}(\boldsymbol{r},t)$ for all voxels in the same xy plane along the z-axis, and the total magnetization precesses uniformly under $B_{d,z}$ [Eq. (3)]. However, for the spatial distribution of proton densities considered here, $\boldsymbol{m}_+(\boldsymbol{r},t)$ in the inner and outer cylinders precess at slightly different rates under respective $B_{d,z}$ fields whose difference is proportional to δm. As $\boldsymbol{m}_+(\boldsymbol{r},t)$ in the two regions evolve out of phase, the phases of the corresponding $\boldsymbol{B}_{d,+}(\boldsymbol{r},t)$ fields also change accordingly. The phase angles between $\boldsymbol{B}_{d,+}(\boldsymbol{r},t)$ and $\boldsymbol{m}_+(\boldsymbol{r},t)$ in the two regions adopt opposite signs as a result of δm [7]. Consequently, $\boldsymbol{B}_{d,+}(\boldsymbol{r},t)$ tilts $\boldsymbol{m}(\boldsymbol{r},t)$ in the inner region toward the $+z$-axis while rotating $\boldsymbol{m}(\boldsymbol{r},t)$ in the outer region toward $-z$. The growing difference in $m_z(\boldsymbol{r},t)$ between the inner and outer cylinders enhances the difference in $B_{d,z}(\boldsymbol{r},t)$ between the two regions, such that the precession frequencies of $\boldsymbol{m}(\boldsymbol{r},t)$ in the two regions diverge accordingly. As a result, the phase of $\boldsymbol{B}_{d,+}(\boldsymbol{r},t)$ with respect to $\boldsymbol{m}_+(\boldsymbol{r},t)$ increases in each region, forcing $m_z(\boldsymbol{r},t)$

even farther apart in a positive feedback cycle. The linear instability of the original magnetization configuration under the DDF produces exponentially increasing contrast in time, as measured through $\Delta m_z(t)$ ($\Delta m_z \equiv \langle m_z(\mathbf{r}_{out},t)\rangle - \langle m_z(\mathbf{r}_{in},t)\rangle$, averaged along the z-axis) [7]. In comparison, when the spin densities in the two cylinders differ by as little as 1%, small spatial variations in m_z may be difficult to detect by conventional spin density imaging due to noise. In practice, contrast enhancement by the DDF feedback mechanism may be more applicable to samples with long T_2 relaxation times.

Contrast between regions differing in resonance frequency may be more readily amplified through the radiation damping feedback field (Fig. 1B). Radiation damping is a macroscopic field that is fed back to the spins through the induced current in the receiver coil, as governed by Lenz's law [3, 16]. This reaction field creates a torque that rotates the magnetization vector back to the $+z$-axis at a rate proportional to the transverse magnetization and faster than T_1 relaxation. When the sample is on resonance in a perfectly tuned probe, the radiation damping field $\mathbf{B}_r(t)$ can be described by

$$\gamma\mathbf{B}_r(t) = \frac{1}{\tau_r}\begin{pmatrix} -\langle m_y(\mathbf{r},t)\rangle \\ \langle m_x(\mathbf{r},t)\rangle \\ 0 \end{pmatrix}, \quad \tau_r = \frac{2}{\gamma\mu_0\eta M_0 Q}. \tag{4}$$

For typical high-Q probes ($Q \approx 500$), the radiation damping time constant τ_r is on the order of 10 ms. For superconducting probes or cryoprobes, Q values as large as 10,000 may be achieved [19], reducing τ_r to 1 ms or less. A well-known phenomenon in high-resolution liquid-state MR, radiation damping commonly interferes with solvent suppression in spectroscopic measurements [16].

Contrast enhancement under the radiation damping field $\mathbf{B}_r(t)$ in MRI is simulated in Fig. 1B for a concentric cylindrical phantom containing solutions with slightly different resonance

frequencies in the two compartments, *e.g.*, due to differences in bulk magnetic susceptibility. Following a large flip-angle pulse (θ=179°), $\boldsymbol{B}_r(t)$ is triggered by the small net transverse magnetization $\langle \boldsymbol{m}_+ \rangle$ and rotates $\boldsymbol{m}(\boldsymbol{r},t)$ toward the +z-axis. As $\boldsymbol{m}_+(\boldsymbol{r},t)$ in the two regions with different resonance frequency both contribute to $\langle \boldsymbol{m}_+ \rangle$, $\boldsymbol{B}_r(t)$ is initially not on resonance with $\boldsymbol{m}_+(\boldsymbol{r},t)$ in either region [Eq. (4)]. However, as the region with greater total magnetization has a greater weighted contribution to $\langle \boldsymbol{m}_+ \rangle$, $\boldsymbol{B}_r(t)$ evolves to be more closely on-resonance with $\langle \boldsymbol{m}_+ \rangle$ in this region compared to $\langle \boldsymbol{m}_+ \rangle$ in the other region. As a result, $\boldsymbol{m}(\boldsymbol{r},t)$ in the region with greater total magnetization nutates toward the +z-axis more quickly, creating still more transverse magnetization, which in turn causes $\boldsymbol{B}_r(t)$ to excite the spins in this region even more effectively while $\boldsymbol{m}(\boldsymbol{r},t)$ in the other region remains comparatively off-resonance with respect to $\boldsymbol{B}_r(t)$. The increasing selectivity of $\boldsymbol{B}_r(t)$ is reflected in Fig. 1B, which shows that $\boldsymbol{B}_r(t)$ is highly selective for resonance frequency differences $\delta\omega$ as small as 5 Hz, with the resulting contrast growing as a power law in time [7]. Such avalanching amplification of MRI contrast by radiation damping is also demonstrated experimentally on samples of human brain tissue for lesion characterization (Figs. 2-4).

For very small differences in resonance frequency, the dynamics under the joint feedback fields of radiation damping and the DDF may provide even better contrast enhancement than that generated under either feedback field alone. In the presence of the joint feedback fields, the local field is described by a nonlinear Bloch equation that combines Eqs. (1), (2), and (4) [6]. Recent studies have revealed that radiation damping and the DDF combine to generate dynamical instability [5] leading to chaotic spin dynamics [6, 7] in high-field MR experiments. Following $[\theta_x\text{-}(GT)_z]$, $\boldsymbol{m}(\boldsymbol{r},t)$ evolves primarily under $\boldsymbol{B}_d(\boldsymbol{r},t)$ at short times, since $\boldsymbol{B}_r(t)$ is initially weak due to the spatial modulation of $\boldsymbol{m}_+(\boldsymbol{r},t)$ by the dephasing gradient. As $\boldsymbol{m}(\boldsymbol{r},t)$ in the inner cylinder

precesses at a different frequency from $\boldsymbol{m}(\boldsymbol{r},t)$ in the outer cylinder, the nonuniform distribution of resonance frequencies in the transverse plane causes $m_+(\boldsymbol{r},t)$ to deviate from the net transverse magnetization $\langle m_+ \rangle$. As a result, $B_{d+}(\boldsymbol{r},t)$ follows the precession of $m_+(\boldsymbol{r},t)$ and assumes different signs in each region [Eq. (2)]. The different directions of $B_{d+}(\boldsymbol{r},t)$ relative to $m_+(\boldsymbol{r},t)$ cause m_z to tilt in opposite directions in the two regions, in close analogy with the mechanism responsible for enhancing contrast under $\boldsymbol{B}_d(\boldsymbol{r},t)$ due to differences in proton density (Fig. 1A). At the same time, residual $\langle \boldsymbol{m}_+ \rangle$ surviving the crusher gradient activates $\boldsymbol{B}_r(t)$, which rotates the modulated $\boldsymbol{m}(\boldsymbol{r},t)$ toward $+z$ to varying extents, depending on the phase of $\boldsymbol{B}_r(t)$ with respect to $\boldsymbol{m}_+(\boldsymbol{r},t)$. The resulting modulation in $m_z(\boldsymbol{r},t)$ creates a nonlinear gradient through the DDF, which distorts the magnetization helix to refocus more $\langle \boldsymbol{m}_+ \rangle$. As $\boldsymbol{B}_r(t)$ excites $\boldsymbol{m}(\boldsymbol{r},t)$ more effectively in the region with greater total magnetization (Fig. 1B), the modulation in m_z becomes more significant and reinforces the effect of the joint reaction fields on this region [24]. On the other hand, the frequency component with smaller total magnetization remains largely off-resonance with respect to the joint reaction fields. The feedback fields intensify until $\langle \boldsymbol{m}_+ \rangle$ reaches a maximum, accompanied by the steep rise in m_z in the outer region and Δm_z (Fig. 1C). Contrast enhancement by the joint feedback fields is confirmed through experimental results for a simple water/ethanol phantom (Fig. 1C).

3.3 Result and Discussion

The choice of which avalanching amplification mechanism in Fig. 1 to use experimentally depends on the contrast origin of interest (i.e., proton density or resonance frequency), reaction field strengths, and physical constraints (e.g., relaxation times). A more complete description of the contrast enhancement mechanisms due to $\boldsymbol{B}_d(\boldsymbol{r},t)$ and $\boldsymbol{B}_r(t)$ separately,

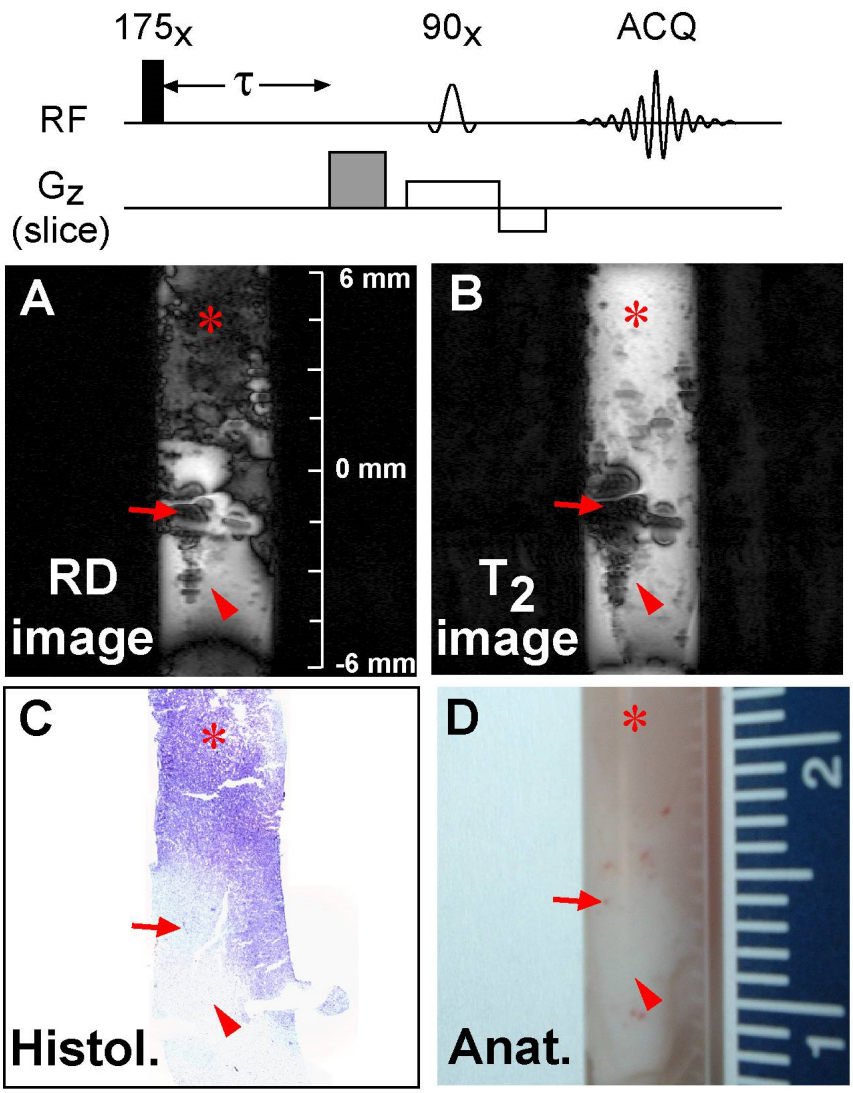

Figure 2. (A) Radiation damping-enhanced and (B) T_2-weighted MR images at 14.1 T of brain tissue excised from the left posterior parietal-occipital lobe of a pediatric patient with cortical dysplasia. Feedback-enhanced images show amplified contrast between gray matter (asterisk) and white matter (arrowhead) in mildly dysplastic tissue, verified through comparison with (C) histology and (D) gross anatomy. The field distortion due to iron in hemoglobin creates imaging artifacts surrounding the blood vessels (A) and (B) (arrow). Pulse sequence at top was used to enhance MRI contrast through the radiation damping feedback field (θ=175°, GT=5G·ms/cm) in (A).

as well as their joint effect, may be found in reference [7, 14]. The short T_2 relaxation times in biological systems (~0.1 s) favor the mechanism depicted in Fig. 1B: avalanching amplification of small variations in resonance frequency by radiation damping, as demonstrated in the following experiments on samples of brain tissue.

We apply avalanching amplification of MRI contrast under radiation damping to improve tissue differentiation in various brain lesions, as shown in Figs. 2-4. For example, focal cortical dysplasia, linked to medically intractable epilepsy in children, is characterized by blurring of the junction between gray and white matter due to abnormal neuronal migration [25]. Figure 2 compares radiation damping-enhanced and conventional T_2-weighted contrast images of mildly dysplastic *in vitro* brain tissue excised from the left posterior parietal-occipital lobe of a patient with cortical dysplasia. In (A) and (B), the sample was imaged by a gradient-echo sequence [vertical 1-mm thick slice, 512 × 128 voxels zero-filled to 512 × 256 voxels, field of view 1.6 cm, echo time of 4.2 ms in (A) and 20 ms in (B)]. MR images of all tissue samples were brightened through nonlinear scaling of the colormap intensity without changing the actual signal intensity values. The field distortion due to the presence of iron in hemoglobin creates imaging artifacts surrounding the blood vessels. While the T_2-weighted image (Fig. 2B) provides better contrast than the proton density or T_1-weighted images, the conventional images fail to differentiate the gray and white matter, which is essential in identifying subtle malformations in cortical development. On the other hand, the feedback-enhanced image shows a clear change in contrast at the junction between the two types of tissue (Fig. 2A). The radiation damping field following the initial 175° pulse selectively excites the magnetization in different regions based on differences in resonance frequency between the abundant nerve cells in gray matter and lipids in myelinated white matter.

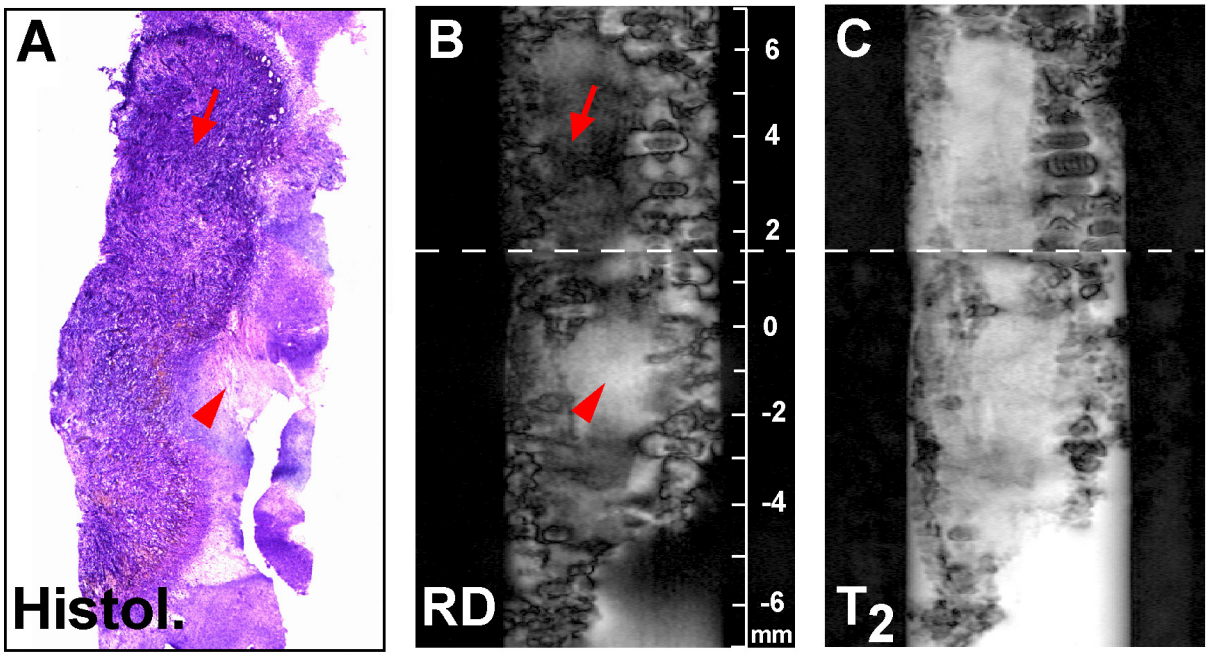

Figure 3. (A) Histology, (B) radiation damping-enhanced, and (C) T_2-weighted images of brain tissue excised from the left temporal lobe of a patient with glioblastoma multiforme (GBM). Histopathology reveals large regions of geographic necrosis (arrowhead) intermixed with tumor tissue (arrow). These features are also highlighted in (B). In (B) and (C), images of the upper and lower halves of the tissue sample were taken separately (field of view 0.8 cm each, total length 1.4 cm), then merged at their interface (indicated by the dashed line). Pulse sequence, parameters, and MR image processing are the same as in Fig. 2.

The contrast highlighted by the radiation damping feedback field correlates with pathology seen in tissue sections. For example, two features of glioblastoma multiforme (GBM), the most common malignant primary brain tumor, are necrosis and microvascular proliferation [26]. These features are reflected in microscopic MR images of three separate brain tissue sections taken from the left temporal lobe of a patient with GBM, shown in Fig. 3 and Fig. 4. Areas of necrosis caused by vascular thrombosis in general appear hyperintense in proton density images due to the breakdown of proteinaceous tumor tissue [27]. The rupture of poorly formed tumor vessels enhances signal intensity in T_1- and T_2-weighted images by releasing paramagnetic extracellular methemoglobin into the necrotic zone. These features are observed in proton density, T_1-, and T_2-weighted images of the tumor sample, consistent with the tissue differentiation shown in the corresponding radiation damping-enhanced image and pathology. On the other hand, the conventional images of the tumor sample in Fig. 3 do not reflect the difference between necrotic and tumor tissues shown in pathology (Fig. 3A). In comparison, the radiation damping-enhanced image in Fig. 3B is sensitive to resonance frequency differences arising from bulk magnetic susceptibility (χ) variations in hypointense, actively dividing tumor cells (varying amounts of oxyhemoglobin and deoxyhemoglobin, $\Delta\chi \approx$-0.0147 ppm and 0.265 ppm, respectively, relative to bulk water) [28, 29] and hyperintense necrotic tissue (extracellular methemoglobin, $\Delta\chi \approx 0.301$ ppm). Necrosis is considered to be an anaplastic feature of astrocytoma and is associated with a poorer prognosis. Thus, by providing a better distinction between necrotic and tumor tissues, feedback-enhanced MR contrast may aid in the diagnosis and assessment of malignant brain tumors before and after surgery and/or radiation therapy.

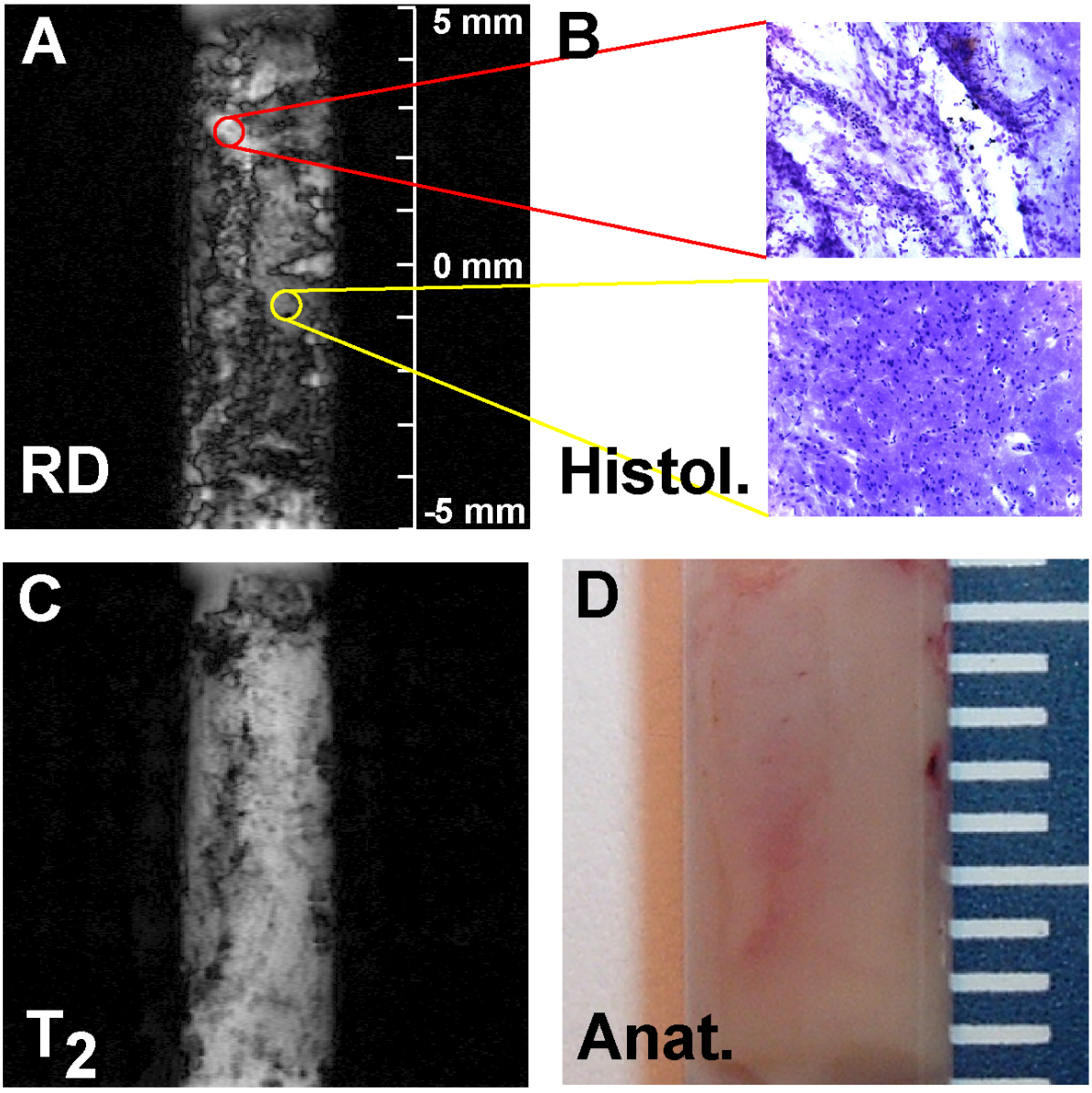

Figure 4. (A) Radiation damping-enhanced MR image of another brain section taken from the same GBM patient as in Fig. 3. (B) Comparison with histology reveals that regions of enhanced signal intensity correspond to tumor cells surrounding the microvasculature (red) compared to normal tissue (yellow). (C) Corresponding T_2-weighted image. (D) Gross anatomy for comparison. Pulse sequence, parameters, and MR image processing are the same as in Fig. 2, except field of view is 1.2 cm (only 1 cm is shown here).

The radiation damping feedback field can also be used to distinguish tumor growth from

the surrounding healthy tissue. Tumor cells surrounding necrosis are intimately involved in the proliferation of microscopic blood vessels [26]. Cross-sections of hyperplastic vasculature appear adjacent to the necrosis in Fig. 3, and blood vessels are seen running longitudinally in another section of the same tumor (Fig. 4). Deoxyhemoglobin in residual blood markedly shortens T_2, which manifests in T_2-weighted images as signal loss (Fig. 4C). In the corresponding radiation damping-enhanced image (Fig. 4A), the hyperintense signal associated with the blood vessels may derive from pronounced variations in resonance frequency caused by paramagnetic deoxyhemoglobin. Furthermore, tumor cells surrounding the microvasculature are highlighted in the radiation damping-enhanced image as amplified, hyperintense regions corresponding to differences in bulk susceptibility originating from variations in blood oxygenation level and increased water content in the compact extracellular space of the tumor (Fig. 4A) [27]. These clusters of malignant cells are not obvious in the proton density image and may not be sufficiently vascular to enhance on T_1- or T_2-weighted images.

Avalanching amplification by the individual or joint feedback fields causes image contrast from spatial variations in MR parameters to grow exponentially before reaching a steady, significant value. During the nonlinear amplification process, larger differences in MR parameters that reflect the underlying physiology or anatomy are highlighted first and, in the absence of relaxation, small fluctuations due to noise or non-uniform experimental perturbations are eventually enhanced at long times [14]. Knowledge of the stability of magnetization configurations under radiation damping and/or the DDF can guide the design of RF pulse sequences that further amplify desired contrast while suppressing the growth of noise [30].

The simple preparation sequences shown here belie the complexity of the underlying dynamics and introduce a novel approach to designing MR pulse sequences. In this new

approach, evolution under the reaction fields allows the spins themselves to play an active role in determining and differentiating their subsequent evolution, thereby improving the distinction between regions with different MR properties. For example, the contrast in the feedback-enhanced images (Figs. 2-4) exceeds that seen in conventional chemical-shift selective images (results to be reported elsewhere), which may be masked by the typically large field inhomogeneity in biological samples [31]. Furthermore, as radiation damping is simply an RF field generated by the receiver coil, this selective feedback mechanism may inspire the design of complex continuous-wave pulse sequences that mimic or even improve upon the resulting contrast, particularly in cases in which the radiation damping field is weak or absent.

Feedback-based contrast enhancement can be generalized to imaging at lower fields through careful consideration of the experimental system, pulse sequence design, and hardware. The DDF has been applied in MRI to image the structural characteristics of materials at varying length scales [10] and to generate imaging contrast via intermolecular multiple quantum coherences (iMQCs) [11] down to field strengths of 1.5 T in clinical scanners [12]. The presence of dipolar instabilities in systems with high spin polarization [13] suggests that the DDF effect can be enhanced in low-field MRI with hyperpolarized nuclei. In addition, the T_2 relaxation becomes less effective at lower fields, which may compensate the weaker DDF effect by allowing it to act for a longer time.. The radiation damping feedback field has been observed in *in vivo* MR spectroscopy [17] as well as *in vitro* and *in vivo* perfusion imaging experiments at 4.7 T [18]. Hardware modifications can also bolster the radiation damping effect at low fields. For example, high-Q and cryogenic probes with short τ_r values are finding increasing applications in MR microscopy and clinical imaging at both high and low fields [20, 21]. Furthermore, radiation damping can also be heightened or suppressed through active electronic feedback to the induced

current in modified circuits, which are already integral components of many commercial spectrometers [22, 23].

3.4 Conclusion

Contrast enhancement under the feedback fields is sensitive to small differences in endogenous MR parameters that correlate with versatile physiological origins. For example, gray and white matter in dysplastic tissue are differentiated through amplified contrast sensitive to differences in chemical composition, and hence precession frequency. This might lead to improved surgical outcomes in patients with intractable epilepsy. Limited variations in the concentrations of oxyhemoglobin, deoxyhemoglobin, and methemoglobin in necrotic, tumor, and healthy tissues are highlighted based on differences in bulk susceptibility, which could aid in tumor characterization and detection. Other applications may include: enhancing functional MRI (fMRI) contrast based on the blood oxygenation level-dependent (BOLD) effect [32]; distinguishing the penumbra zone of stroke (*i.e.*, reversibly injured tissue) from irreversible infarction through amplified pH-dependent contrast [33]; and improving tumor characterization by sensitive detection of amide-proton exchange rate variations between normal and cancerous tissue [34]. The observed illumination of paramagnetic hemoglobin in the feedback-enhanced images suggests that this amplification scheme may be also integrated with targeted magnetic nanoparticles in molecular imaging to achieve better disease specificity and lower detection limits of molecular events.

3.5 References

[1] A. P. Pathak et al., *Methods Enzymol.* **386**, 3 (2004).

[2] S. W. Cook *et al.*, *J. Neurosurg.* (Suppl. S) **100**, 125 (2004).

[3] N. Bloembergen, R. V. Pound, *Phys. Rev.* **95**, 8 (1954).

[4] G. Deville, M. Bernier, J. M. Delrieux, *Phys. Rev. B* **19**, 5666 (1979).

[5] J. Jeener, *J. Chem. Phys.* **116**, 8439 (2002).

[6] Y.-Y. Lin, N. Lisitza, S. Ahn, W. S. Warren, *Science* **290**, 118 (2000).

[7] S. Datta, S. Y. Huang, Y.-Y. Lin, *J. Chem. Phys.* (submitted).

[8] W. S. Warren, W. Richter, A. H. Andreotti, B. T. Farmer II, *Science* **262**, 2005 (1993).

[9] W. S. Warren, S. Lee, W. Richter, S. Vathyam, *Chem. Phys. Lett.* **247**, 207 (1995).

[10] R. Bowtell, P. Robyr, *Phys. Rev. Lett.* **76**, 4971 (1996).

[11] W. S. Warren *et al.*, *Science* **281**, 247 (1998).

[12] J. H. Zhong, Z. Chen, E. Kwok, *Magn. Reson. Med.* **43**, 335 (2000).

[13] M. P. Ledbetter, I. M. Savukov, M. V. Romalis, *Phys. Rev. Lett.* **94**, 060801 (2005).

[14] S. Datta, S. Y. Huang, Y.-Y. Lin, *J. Chem. Phys.* (submitted).

[15] T. Enss, S. Ahn, W. S. Warren, *Chem. Phys. Lett.* **305**, 101 (1999).

[16] M. P. Augustine, *Prog. Nucl. Magn. Reson. Spectrosc.* **40**, 111 (2002).

[17] P. C. M. van Zijl, C. T. W. Moonen, *NMR Basic Princ. Progr.* **26**, 67 (1992).

[18] J. Zhou, S. Mori, P. C. M. van Zijl, *Magn. Reson. Med.* **40**, 712 (1998).

[19] R. D. Black *et al.*, *Science* **259**, 793 (1993).

[20] Q. Y. Ma *et al.*, *Acad. Radiol.* **10**, 978 (2003).

[21] A. C. Wright, H. K. Song, F. W. Wehrli, *Magn. Reson. Med.* **43**, 163 (2000).

[22] P. Broekaert, J. Jeener, *J. Magn. Reson., Ser. A* **113**, 60 (1995).

[23] A. Louis-Joseph, D. Abergel, J.-Y. Lallemand, *J. Biomol. NMR* **5**, 212 (1995).

[24] S. Y. Huang, J. D. Walls, Y. Wang, W. S. Warren, Y.-Y. Lin, *J. Chem. Phys.* **121**, 6105 (2004).

[25] D. C. Taylor, M. A. Falconer, C. J. Bruton, J. A. Corsellis, *J. Neurol. Neurosurg. Psychiatry* **34**, 369 (1971).

[26] P. Kleihues *et al.*, in *Pathology and Genetics of Tumours of the Nervous System*, P. Kleihues, W. K. Cavenee, Ed. (IARC Press, Lyon, 2000), pp. 29-39.

[27] R. A. Zimmerman, L. T. Bilaniuk, in *Neuroimaging: Clinical and Physical Principles*, R. A. Zimmerman, W. A. Gibby, R. F. Carmody, Ed. (Springer, New York, 2000), pp. 986-991.
W. G. Bradley, Jr., *Radiology* **189**, 15 (1993).

[28] W. M. Spees, D. A. Yablonskiy, M. C. Oswood, J. J. H. Ackerman, *Magn. Reson. Med.* **45**, 533 (2001).

[29] M. Zborowski *et al.*, *Biophys. J.* **84**, 2638 (2003).

[30] S. Y. Huang *et al.*, in preparation.

[31] E. M. Haacke, R. W. Brown, M. R. Thompson, R. Venkatesan, *Magnetic Resonance Imaging: Physical Principles and Sequence Design* (Wiley & Sons, New York, 1999), pp. 421-449.

[32] S. Ogawa, T. M. Lee, A. R. Kay, D. W. Tank, *Proc. Natl. Acad. Sci. USA* **87**, 9868 (1990).

[33] J. Y. Zhou, J. F. Payen, D. A. Wilson, R. J. Traystman, P. C. M. van Zijl, *Nat. Med.* **9**, 1085 (2003).

[34] J. Y. Zhou, B. Lal, D. A. Wilson, J. Laterra, P. C. M. van Zijl, *Magn. Reson. Med.* **50**, 1120 (2003).

Chapter 4

Fixed-Point Imaging for Early Cancer Detection: Quantum Description

4.0 Abstract

The use of weak continuous wave (CW) irradiation in the presence of passive or active feedback fields is shown to produce unique stable fixed points (or constants of motion). The location of the fixed points as well as the quantum dyanmics *en route* to the fixed points are investigated within a density operator framework. Applications for imaging contrast enhancement for early tumor detection are discussed and demonstrated.

4.1 Introduction

With regards to biomedical diagnostics, magnetic resonance imaging (MRI) has a great advantage due to its employment of low-energy, non-ionizing radio-frequency (RF) radiation [7]. Unfortunately, this increase in safety and applicability comes at the expense of the immense specificity that is present in other imaging modalities that make use of ionizing radiation, such as Computed Tomography (CT) and Positron Emission Tomography (PET) [3]. Contrast in MRI is currently dependent on the molecular dynamics of differing tissues, resulting in variety of relaxation times of the signal. This can be very limiting when trying to differentiate between tissues or materials with only a slight difference in relaxation parameters, as is the case in trying to distinguish between early tumors and healthy tissue. The advent of early tumors can be

marked by a slight shift in magnetic susceptibility. This meager shift in the local field is independent of molecular dynamics and is thus essentially invisible to the conventional, relaxation-based imaging mechanisms. There has thus been an interest in the development of robust imaging techniques that are sensitive to the local susceptibility variations across a sample [14, 4, 9, 8].

In this work, it is shown that the use of weak continuous wave (CW) radiation in the presence of the passive or active feedback fields is sensitive to the small magnetic susceptibility differences of a sample, producing unique and fortuitous fixed-points on opposite sides of the Bloch sphere. The evolution of the magnetization *en route* to the fixed points was shown to be useful in the detection of early tumors in mice, having a much improved contrast-to-noise (CNR) ratio over conventional imaging methods. Here we lay forth a theoretical foundation for the development of the fixed points, and analyze the quantum dyanmics and how they can be useful for the development of imaging contrast.

The passive feedback field of radiation damping was discovered and characterized in the early days of NMR [1]. By Lenz's law, an induced oscillating current in a coil will be met by an opposing oscillating field. This reactionary field can then act back onto the sample, accelerating the magnetization back towards the equilibrium $+z$ position, shortening the FID. The decreased signal lifetime thus corresponds to a significantly broadened solvent peak in the sample spectrum, obscuring important peaks, especially in high-field biomolecular NMR. Feedback fields can also be generated from homebuilt active feedback-controlled electronic device. The device is to filter, phase shift, and amplify the signal from the receiver coils and then retransmit the modified signal into the RF transmission coil, with adjustable and programmable feedback phases and gains. The MR console computer can execute the active-feedback pulse sequences to

control the trigger signal, feedback phase/gain, and the duration of the feedback fields, allowing us to utilize the active feedback fields in novel ways. The inherent dependence of the feedback field on the instantaneous state of the sample causes the evolution of the magnetization to be nonlinear and even chaotic [2, 13, 11].

With the advent of pulsed Fourier NMR [6], the use of a CW in both spectroscopy and imaging has been reserved for secondary dynamics such as decoupling or presaturation [5]. In other experiments, a CW is used to tilt the effective field in order to study relaxation behaviors in different frames of reference [10]. The constant perturbation of the CW coupled with the non-linear evolution resulting from the passive or active feedback fields would thus not be expected to produce stable fixed-points of the magnetization that are not at the equilibrium $+z$ position. While the dynamics surrounding both a CW and passive/active feedback fields can be modeled classically [13, 11], the physical origin behind the fixed points is much more transparent within a density operator formalism. The following theory can thus be recast within the more familiar classical framework, but with less intuition and prediction as to the nature of the fixed points themselves.

4.2 Theory and Method

The Hamiltonian for a spin system in the laboratory frame can be given by

$$\hat{H}_{lab}(t) = \hat{H}_0 + \hat{H}_1(t) \tag{1}$$

where $\hat{H}_0$ and $\hat{H}_1$ represent the static and interaction Hamiltonians, respectively. The static Hamiltonian is the familiar Zeeman interaction, $\hat{H}_0 = \hbar\omega_0\hat{I}_z$. The interaction Hamiltonian

contains information regarding any resonance offset as well as the static excitation of the radio-frequency field

$$\hat{H}_I = \hbar\omega_1\left(e^{-i\hat{I}_z\omega_0 t}\hat{I}_x e^{i\hat{I}_z\omega_0 t}\right) + \hbar\delta\omega\hat{I}_z \tag{2}$$

where $\hbar\delta\omega$ represents the resonance offset from the Larmor frequency ω_0. The Rabi frequency ω_1 [12] is proportional to the strength of the excitation field. The equation of motion for the density operator under a particular Hamiltonian is thus given by the Liouville-von Neumann equation:

$$\frac{\partial\hat{\rho}(t)}{\partial t} = -\frac{i}{\hbar}\left[\hat{H}_0 + \hat{H}_I, \hat{\rho}(t)\right] \tag{3}$$

By simple unitary transformation, using $\hat{U}(t) = e^{i\hat{I}_z\omega_0 t}$, Eq. 3 can be transformed to the Dirac picture (or rotating frame of reference at frequency ω_0) such that

$$\frac{\partial\hat{\rho}^*(t)}{\partial t} = -\frac{i}{\hbar}\left[\hat{H}_I^*, \hat{\rho}^*(t)\right] \tag{4}$$

where $\hat{H}_I^* = \hbar\delta\omega\hat{I}_z + \hbar\omega_1\hat{I}_x$. For the sake of brevity, the asterisks and interaction subscripts are dropped as the rest of the discussion is within the Dirac picture.

For a two-component uncoupled system, the total Hamiltonian for both spins is simply the sum of the individual Hamiltonians, $\hat{H}_{ij} = \hat{H}_i + \hat{H}_j$, where the subscript notation refers to the i th and j th spins. These two components differ only in their resonance offset such that $\Delta\omega_{ij} = \delta\omega_i - \delta\omega_j \neq 0$. For simplicity, assume that the offset for both components is equal in magnitude such that $\delta\omega_i = -\delta\omega_j = \delta\omega$. The total Hamiltonian for these two spins can thus be simplified to

$$\hat{H}_{ij} = \hbar\omega_1\hat{I}_{x,ij} + \hbar\delta\omega\hat{I}_{z,ij} \tag{5}$$

where $\hat{I}_{x,ij} = \hat{I}_{x,i} + \hat{I}_{x,j}$, and $\hat{I}_{z,ij} = \hat{I}_{z,j} - \hat{I}_{z,i}$. While the time evolution of the system under this Hamiltonian is not of any particular interest, the constants of motion (or called "fixed points" of the dynamics) are worth investigating, as the results are somewhat surprising in the presence of feedback fields.

4.2.1 Existence and location of the fixed points

The constants of motion can be solved by simply setting Eq. (4) equal to zero. These can be seen to simply be the density matrices that commute with $\hat{H}_{ij}$. Since the Hamiltonian can be simply expanded as a vector in Liouville space, the constants of motion, $\hat{\rho}_{ij} = \hat{\rho}_i + \hat{\rho}_j$, are just the vectors in the same space that lie either parallel or anti-parallel to $\hat{H}_{ij}$. The four physically relevant constants of motion are thus

$$\begin{aligned}
\hat{\rho}_{++} &= \frac{1}{4}\hat{\mathbf{1}} + \hat{H}_i + \hat{H}_j \\
\hat{\rho}_{+-} &= \frac{1}{4}\hat{\mathbf{1}} + \hat{H}_i - \hat{H}_j \\
\hat{\rho}_{-+} &= \frac{1}{4}\hat{\mathbf{1}} - \hat{H}_i + \hat{H}_j \\
\hat{\rho}_{--} &= \frac{1}{4}\hat{\mathbf{1}} - \hat{H}_i - \hat{H}_j
\end{aligned} \tag{6}$$

where $\hat{\mathbf{1}}$ is the identity operator, and the $\pm$ subscript notation is used in reference to the sign in front of each respective Hamiltonian term. Physically, it can be seen that the $\hat{\rho}_{++}$ state has both components aligned with the effective field, with the $\hat{\rho}_{--}$ state with both components anti-parallel to the effective field. Likewise, both of the $\hat{\rho}_{+-}$ and $\hat{\rho}_{-+}$ states have one component aligned with the effective field, and one aligned anti-parallel. Energetically, since $E_{ij} = Tr[\hat{H}_{ij}\hat{\rho}_{ij}]$, it can be seen that the $\hat{\rho}_{++}$ state is lowest in energy and the $\hat{\rho}_{--}$ state being the highest in

energy, with both the $\hat{\rho}_{+-}$ and $\hat{\rho}_{+-}$ states in between, as would be expected. In the event that the frequency difference between the two components is small, it would be near impossible to selectively excite one component over the other, making the $\hat{\rho}_{+-}$ and $\hat{\rho}_{-+}$ states practically inaccessible, and thus not very interesting. This is not the case, however, in the presence of feedback fields.

In order to analyze the constants of motion in the presence of feedback fields, a semi-classical coupling term needs to be added to Eq. (5) for each component of the form

$$\hat{H}_{FF,i} = \hbar\omega_r\left(\Re\left[\langle i\hat{I}_{ij}^{+}\rangle(t)\right]\hat{I}_{x,i} + \Im\left[\langle i\hat{I}_{ij}^{+}\rangle(t)\right]\hat{I}_{y,i}\right) \tag{7}$$

where ω_r is the strength of the passive/active feedback fields, $\Re$ and $\Im$ represent the real and imaginary component of $\langle i\hat{I}_{ij}^{+}\rangle(t) = iTr[\hat{I}_{ij}^{+}\hat{\rho}_{ij}(t)]$, and $\hat{I}_{ij}^{+} = p_i\hat{I}_i^{+} + p_j\hat{I}_j^{+}$ with $p_i + p_j = 1$. In this particular case, $p_i = p_j = 1/2$. The imaginary number in Eq. 7 represents a complex rotation of $\langle\hat{I}_{ij}^{+}\rangle(t)$ such that the feedback fields is always applied 90° out of phase with total transverse magnetization, or that $\hat{H}_{FF} \perp \langle\hat{I}_{ij}^{+}\rangle(t)$. The total Hamiltonian, $\hat{H}_{ij}' = \hat{H}_{ij} + \hat{H}_{FF}$, for the sample thus becomes

$$\hat{H}_{ij}' = \hbar\delta\omega\hat{I}_{z,ij} + \left(\Re\left[\langle i\hat{I}_{ij}^{+}\rangle(t)\right] + \hbar\omega_1\right)\hat{I}_{x,ij} + \Im\left[\langle i\hat{I}_{ij}^{+}\rangle(t)\right]\hat{I}_{y,ij} \tag{8}$$

It can be seen that the functional form of Eq. (7) contains pseudo-bilinear terms such as $\langle\hat{I}_{ij}^{+}\rangle\hat{I}_{x,i}$, which differ significantly from the familiar two-spin coupling terms, but nonetheless represent a coupling of each spin with the rest of the sample.

From Eq. (6), it can be seen that since the constants of motion align either parallel or anti-parallel to the uncoupled Hamiltonian, then $\langle\hat{I}_{ij}^{+}\rangle\mathsf{P}\hat{H}_{ij} \perp \hat{H}_{FF}$. Thus $[\hat{H}_{ij}, \hat{H}_{FF}] \neq 0$ unless $\hat{H}_{FF} = 0$, which can only be the case when $\langle\hat{I}_{ij}^{+}\rangle = 0$. For both of the $\hat{\rho}_{++}$ and $\hat{\rho}_{--}$ states, it can

be seen that $\langle \hat{I}^{+}_{\pm\pm} \rangle \propto \pm 2\omega_1 \neq 0$, and so $[\hat{H}_{ij}', \hat{\rho}_{\pm\pm}] \neq 0$ meaning that both the $\hat{\rho}_{++}$ and $\hat{\rho}_{--}$ states are annihilated as constants of motion with the addition of feedback fields. This is not the case, however, with the $\hat{\rho}_{+-}$ and $\hat{\rho}_{-+}$ states, where it can be seen that $\langle \hat{I}^{+}_{\pm\mp} \rangle = 0$ because both components are anti-parallel to each other, and so $\hat{H}_{FF} = 0$. Consequently, $\hat{H}_{ij} = \hat{H}_{ij}'$, and thus both of the anti-parallel states are preserved as constants of motion, since they already commute with the uncoupled Hamiltonian.

Thermodynamically, the $\hat{\rho}_{+-}$ and $\hat{\rho}_{-+}$ states are energetically favored over the $\hat{\rho}_{++}$ and $\hat{\rho}_{--}$ states, which are no longer constants of motion. From Eq. (7), it can be seen that for $\langle \hat{I}^{+}_{ij} \rangle \neq 0$, the feedback-field term is going to be in direct competition with the uncoupled interaction Hamiltonian since they are applied perpendicular to each other. As the feedback-field term becomes larger, it begins to draw each component away from the uncoupled Hamiltonian, subsequently raising the total Zeeman energy of the system. Consequently, the system will naturally adopt the configuration that can minimize $\langle \hat{I}^{+}_{ij} \rangle$, thus reducing $\hat{H}_{FF}$. When $\Delta p_{ij} = | p_i - p_j | = 0$, it is easy to see that the components can align to perfectly cancel each other out such that $\langle \hat{I}^{+}_{ij} \rangle = 0$, and thus $\hat{H}_{FF} = 0$. In the event that each component does not have equal contribution to the feedback fields, $\Delta p_{ij} \neq 0$, and so $\hat{H}_{FF} \neq 0$. Since $\hat{H}_{FF} \perp \hat{H}_{ij}$, the total energy for both the $\hat{\rho}_{+-}'$ and $\hat{\rho}_{-+}'$ states raises because these states are no longer aligned with the total field.

The degree in which the $\hat{\rho}_{+-}'$ and $\hat{\rho}_{-+}'$ states shift can be quite challenging to determine analytically. One method could be to treat $\hat{H}_{ij}' = \hat{H}_{ij} + \hat{H}_{FF}$ in a perturbative sense where $\hat{H}_{ij}$ is the unperturbed Hamiltonian for which we have the constants of motion, and $\hat{H}_{FF}$ is the

perturbation for which the corrections can be solved for. This approach is significantly complicated by the fact that the perturbation is dependent on many factors, including the density matrix itself. Understandably, any non-zero feedback fields will tilt $\hat{\rho}_{+-}$' and $\hat{\rho}_{-+}$' away from the original axis in order to minimize the total energy. However, in doing so, the direction of the feedback fields will then change requiring $\hat{\rho}_{+-}$' and $\hat{\rho}_{-+}$' to tip away even further from the original axis. Eventually, the amount of energy that the system can gain from tipping $\hat{\rho}_{+-}$' and $\hat{\rho}_{-+}$' will be balanced out by the energy cost of rotating $\hat{\rho}_{+-}$' and $\hat{\rho}_{-+}$' away from the static field, $\omega_1 \hat{I}_x$. Additionally, in order to minimize $\langle \hat{I}_{ij}^{+} \rangle$, the system could tip both components away from the transverse plane. Again, this comes at the cost of tipping the components away from $\omega_1 \hat{I}_x$, which raises the total energy of the system. Thus, there is a direct competition between the resonance offset, $\delta\omega$, the excitation field, ω_1, and the feedback field, $\hat{H}_{FF} \propto \Delta p_{ij} \omega_r$. The orientations of $\hat{\rho}_{+-}$' and $\hat{\rho}_{-+}$' that minimize the energy can thus be determined using a variational approach.

By setting $\sqrt{\omega_1^2 + (\Delta p_{ij} \omega_r)^2} >> \delta\omega$, an approximation can be made for how much $\hat{\rho}_{+-}$' and $\hat{\rho}_{-+}$' need to shift in order to minimize the total energy. This constraint ensures that the reorientation of $\hat{\rho}_{+-}$' and $\hat{\rho}_{-+}$' be dominated by the interplay between ω_1 and $\Delta p_{ij} \omega_r$. The constraint is reasonable because the origin of the fixed points is a direct consequence of mixing the excitation field and the feedback fields, and less dependent on the magnitude of the actual resonance offset of each component. Considering that the total energy is minimized when $\langle \hat{I}_{ij}^{+} \rangle \| (\hat{H}_{ij} + \hat{H}_{FF})$ along with the fact that $\langle \hat{I}_{ij}^{+} \rangle \perp \hat{H}_{FF}$, by simple geometric argument one can

show that the angle, θ_t, both $\hat{\rho}_{+-}$' and $\hat{\rho}_{-+}$' need to be rotated to minimize the energy can be given as

$$\theta_t \cong \tan^{-1}\left[\frac{\Delta p_{ij}\omega_r \cos(\theta_t)}{\omega_1 - \Delta p_{ij}\omega_r \sin(\theta_t)}\right] = \sin^{-1}\left[\frac{\Delta p_{ij}\omega_r}{\omega_1}\right] \tag{9}$$

where this can be seen to only be valid for $\omega_1 \geq \Delta p_{ij}\omega_r$. It can thus be seen that when both components do not contribute equally to the feedback fields, the $\hat{\rho}_{+-}$' and $\hat{\rho}_{-+}$' states become

$$\hat{\rho}_{\pm\mp}' \cong e^{i\hat{I}_z\theta_t}\hat{\rho}_{\pm\mp}e^{-i\hat{I}_z\theta_t} \tag{10}$$

In the limit that either $\Delta p_{ij} \to 0$ or $\omega_r \to 0$, the orientations of the $\hat{\rho}_{+-}$' and $\hat{\rho}_{-+}$' states converge to the original $\hat{\rho}_{+-}$ and $\hat{\rho}_{-+}$ states as expected. While the anti-parallel orientations of the $\hat{\rho}_{+-}$ and $\hat{\rho}_{-+}$ states originate from minimizing the total energy of the system, the development of these fixed-points from equilibrium is not trivial and requires a more in-depth analysis.

4.2.2 Quantum dyanmics *en route* to the fixed points

At equilibrium, the density matrix is given by

$$\hat{\rho}_0 = \frac{1}{4}\hat{\mathbf{1}} + \frac{\mathbf{P}}{4}\left(\hat{I}_{z,i} + \hat{I}_{z,j}\right) \tag{11}$$

where $\mathbf{P} = \tanh(\hbar\gamma B_0/k_B T)$. Evolution of the density matrix in the appropriate frame of reference is governed by the Liouville-von Neumann equation as given in Eq. (4). In the absence of feedback fields, the solution to Eq. (4) for the Hamiltonian given in Eq. (5) is simply

$$\hat{\rho}(t) = \underline{U_{ij}}(t)\hat{\rho}_0 \tag{12}$$

where $\underline{U_{ij}}$ is just the superoperator ($\underline{U_{ij}}A = \hat{U}_{ij} A \hat{U}_{ij}^{-1}$) form of

$$\hat{U}_{ij}(t) = \exp\left\{i\hat{I}_{x,ij}' \omega_e t\right\} \exp\left\{i\hat{I}_{y,ij} \theta_{i/j}\right\} \tag{13}$$

where $\hat{I}_{x,ij}' = \exp\{i\hat{I}_{y,ij}\theta_{i/j}\}(\hat{I}_{x,ij})\exp\{-i\hat{I}_{y,ij}\theta_{i/j}\}$ is a rotation of the excitation field by an angle $\theta_{i/j} = \tan^{-1}\left[\delta\omega_{i/j}/\omega_1\right]$, and the frequency of rotation about the new excitation axis is $\omega_e = (\omega_1^2 + \delta\omega_{i/j}^2)^{1/2}$. This solution is simply a rotation of each component around the effective field.

Solving Eq. (4) with the Hamiltonian in Eq. (8) is not trivial. As previously discussed, the Hamiltonian in Eq. (8) not only varies with time, but has an explicit dependence on the instantaneous state of $\hat{\rho}(t)$, rendering the time evolution as non-linear. The propagator, $\underline{U_{ij}}(\delta t, \hat{\rho}(t'))$, dependent on the density operator at time, t', acts for a short interval, δt, such that the density operator at time $t = t' + \delta t$ can be given as

$$\begin{aligned} \hat{\rho}(t) &= \underline{U_{ij}}(\delta t, \hat{\rho}(t'))\,\hat{\rho}(t') \\ &= \underline{U_{ij}}(\delta t, \hat{\rho}(t'))\underline{U_{ij}}(\delta t, \hat{\rho}(t''))\,\hat{\rho}(t'') \\ &= \underline{U_{ij}}(\delta t, \hat{\rho}(t'))\ldots\underline{U_{ij}}(\delta t, \hat{\rho}(t_0))\,\hat{\rho}(t_0) \end{aligned} \tag{14}$$

where $t' = t'' + \delta t$, until $t^{n-1} = t_0 + \delta t$. As seen in Eq. (7) and Eq. (8), any immediate change in $\hat{\rho}(t)$ is immediately reflected in a new Hamiltonian acting on $\hat{\rho}(t + \delta t)$. This calls for the limit where $\delta t \to 0$, requiring an infinite recursion of propagators from time $t_0 \to t$. This sort of analytical consideration becomes intractable, considering the extreme sensitivity to initial conditions. An approximate solution for $\hat{\rho}(t)$ can be obtained by numerical integration of Eq. (4) using the Hamiltonian in Eq. (8) and initial conditions in Eq. (11). The result is shown in Fig.

1A. Starting from equilibrium, the expectation values for each component can be seen to spiral

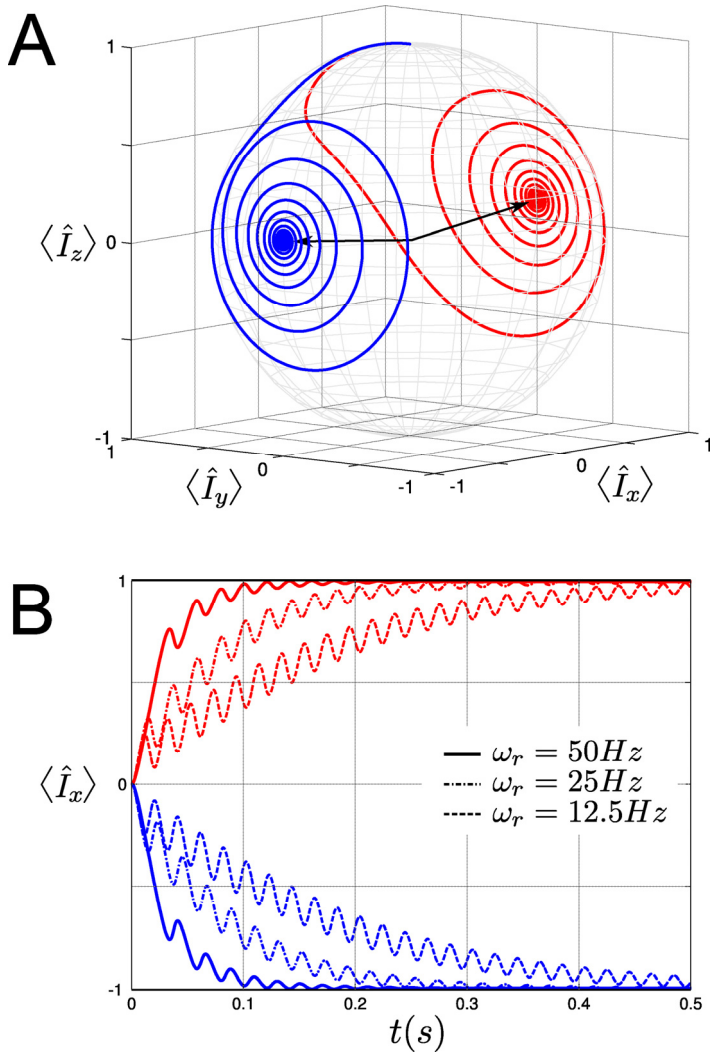

Figure 1. Simulations showing the effect of different feedback-field strengths on the development of the constants of motion. (A) 3D trajectory (corresponding to the 3 observables, $\langle \hat{I}_x \rangle$, $\langle \hat{I}_y \rangle$, and $\langle \hat{I}_z \rangle$), for each of the individual components of the density matrix, $\hat{\rho}(t)$ with $\omega_1 = 50\text{Hz}$, $\omega_r^{-1} = \tau_r = 3\text{ms}$, and $\delta\omega_{i/j} = \pm 5\text{Hz}$. The black arrows show the orientation of the fixed points, corresponding to the $\hat{\rho}_{-+}$ state, as predicted in Eq. (6). (B) Evolution of $\langle \hat{I}_x \rangle$ for each component of $\hat{\rho}(t)$ with the same ω_1 and $\delta\omega_{i/j}$ as in (A), with variable values for ω_r.

away from the other component, towards stable fixed points on opposite poles of the Bloch sphere. The location of these fixed points is consistent with the constants of motion presented in Eq. (6), and this particular orientation represents the $\hat{\rho}_{-+}$ state. Numerical analysis reveals that, while the $\hat{\rho}_{+-}$ state is fixed, it is not stable and thus can only be achieved if the system starts in this specific state. The development of these states is understandably a result of the competition between the excitation field, and the feedback fields.

In the absence of feedback fields, the effect the excitation field is to invert the populations of the density matrix on a time scale of $\tau = (2\omega_1)^{-1}$, or one half of the inverse Rabi frequency. The populations are then inverted a second time on the same time scale, bringing the density matrix back to $\hat{\rho}_0$. In the presence of feedback fields, a different time scale can be predicted because population inversion requires the creation of coherences, $\langle \hat{I}_{ij}^{+} \rangle$, which activates Eq. (7). The net effect of Eq. (7) is to create an imbalanced Rabi cycle, where the feedback fields destructively interfere with the initial population inversion, requiring a time scale of $\tau_1 > (2\omega_1)^{-1}$, and constructively interferes with the second inversion, reducing the time scale to $\tau_2 < (2\omega_1)^{-1}$.

In the presence of the $\delta\omega_{i/j}\hat{I}_{z,i/j}$ terms, the $\langle \hat{I}_{i/j}^{+} \rangle$ part of each component will acquire a phase during the initial inversion, and a negative phase during the second inversion of the populations. Without feedback fields, the required time to invert the populations is equal, and so after one full cycle, the net acquired phase for each component is zero. In the presence of feedback fields, the time required for both inversions is different, and so it can be easily seen that the magnitude of the acquired phase during the first inversion will be greater than that of the second inversion, resulting in a net phase accumulation after one full cycle. In this example,

since $\delta\omega_i = -\delta\omega_j$, it can be seen that there will be a net phase difference between both components after one full rotation. Subsequent inversion cycles allows for the process to repeat itself indefinitely until the total system arrives at its constant of motion, or fixed points.

The rate at which the system evolves towards the fixed points depends on the extent of the imbalanced Rabi cycle. Increasing ω_r with respect to ω_1 creates a larger imbalance, allowing for a greater phase accumulation between each component for a given cycle. Consequently, fewer cycles are required in order for each component to obtain a maximum phase separation. Conversely, reducing ω_r with respect to ω_1 decreases the imbalance, diminishing the total phase accumulation for each cycle, thus increasing the amount of time required to reach the fixed points, as can be seen in Fig. 1B. The time required to reach the fixed points is inversely proportional to the imbalance in the Rabi cycle. Of course, in the limit that $\omega_1 >> \omega_r$, the imbalance becomes negligible, and there will be effectively no phase accumulation between each component. On the same note, in the limit that $\omega_1 = \omega_r$, the feedback fields prevents any possible inversion, hindering any phase accumulation. So it can be seen that the condition that $\omega_1 : \omega_r$ must be met in order for the constants of motion to develop on any reasonable time scale.

The development of the fixed points is rather straight forward in the case where $\Delta p_{ij} = 0$ because of the even symmetry between both components. There is a significant shift in dynamics when the symmetry is broken ($\Delta p_{ij} \neq 0$) as can be seen in Figs. 2B-D. The effect of simply changing $p_i = p_j$ (Fig. 2A) to $p_i = 3p_j$ (Fig. 2B) tilts the location of the fixed points as expected from Eq. (9). Despite the change in evolution, some of the basic principles in the even-symmetry case still apply. The broken symmetry is clearly displayed in the differing evolution of each component. The component with a greater contribution to the Eq. (7) is clearly the component

that races towards its fixed point more rapidly, where the component with lesser contribution takes more time to stabilize.

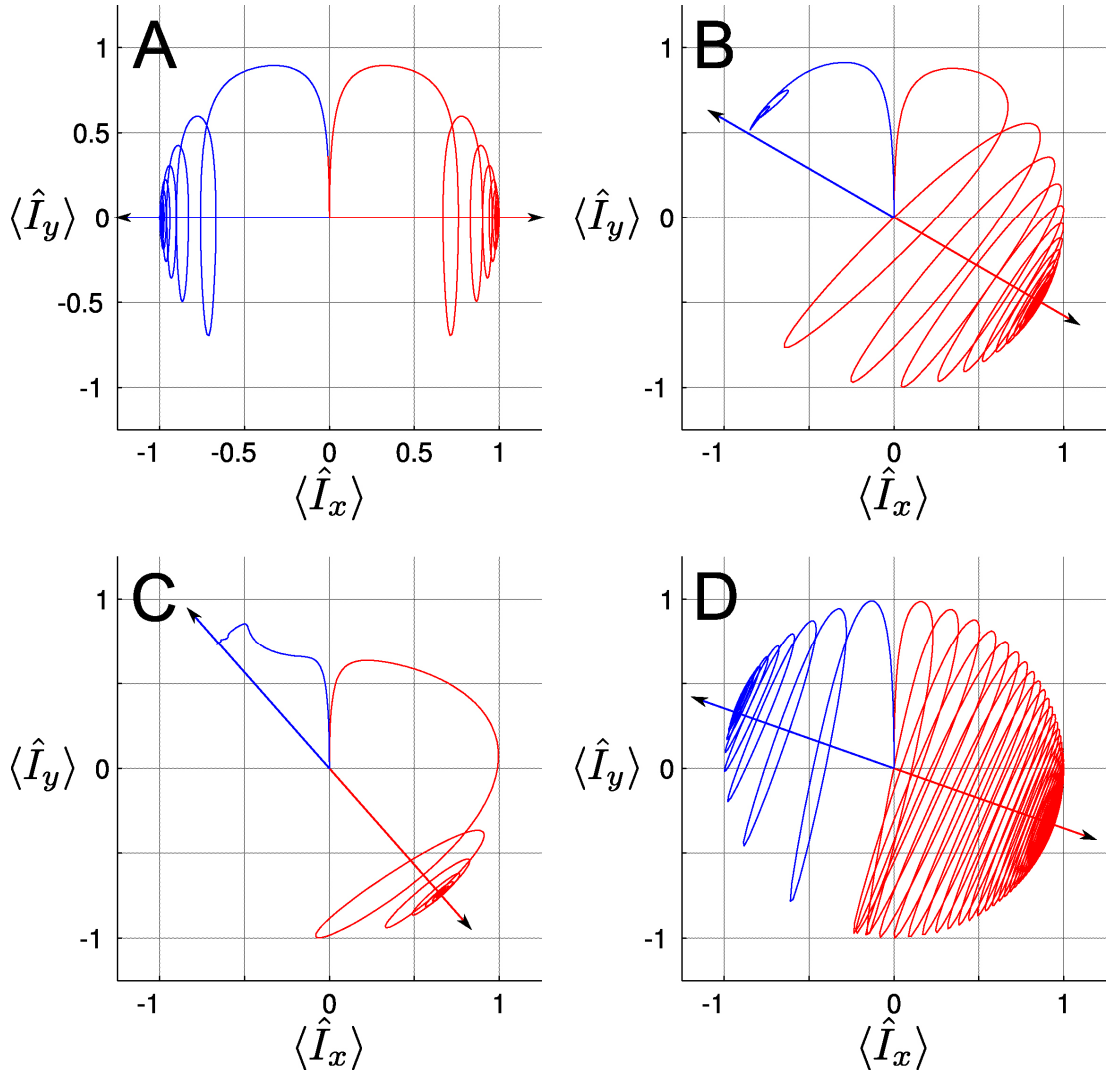

Figure 2. 2D trajectories, showing the off-diagonal terms of $\hat{\rho}(t)$ (corresponding to $\langle \hat{I}_x \rangle$ and $\langle \hat{I}_y \rangle$), where (A) $\omega_1 = 50\text{Hz}$, $\omega_r = 50\text{Hz}$, and $\delta\omega_{ij} = 5\text{Hz}$, and $p_i = p_j$, (B) $\omega_1 = 50\text{Hz}$, $\omega_r = 50\text{Hz}$, and $\delta\omega_{ij} = 5\text{Hz}$, and $p_i = 3p_j$, (C) $\omega_1 = 50\text{Hz}$, $\omega_r = 75\text{Hz}$, and $\delta\omega_{ij} = 5\text{Hz}$, and $p_i = 3p_j$, (D) $\omega_1 = 75\text{Hz}$, $\omega_r = 50\text{Hz}$, and $\delta\omega_{ij} = 5\text{Hz}$, and $p_i = 3p_j$, The arrows correspond to the $\hat{\rho}_{-+}$ state as predicted by Eq. (10).

While the evolution is highly dependent on $\delta\omega$, ω_1 ω_r, and Δp_{ij}, a simplistic model can be presented to provide insight behind the parameter-sensitive dynamics. The evolution of the entire system can be understood by simple independent analysis of each component. The evolution of the component with larger contribution to Eq. (7) will experience a feedback field that is primarily dependent on itself. As a result, its evolution is going to be largely independent of the lesser component, which has only a minor contribution to Eq. (7). The development of a stable fixed point for a singular component in the presence of feedback field has been previously characterized [13], and so it is expected that the larger component will rapidly attempt to stabilize itself in the lowest-energy configuration.

The evolution for the component with lesser contribution to Eq. (7) will experience a different environment. Because the lesser component has only a minor contribution to the feedback fields, it will be predominantly influenced by the evolution of the larger component. Once the larger component reaches its fixed point, the feedback fields become largely static and so the lesser component evolves under a new effective field with a new effective Rabi frequency $\omega_1' = \sqrt{\omega_1^2 + (\Delta p_{ij}\omega_r)^2}$, where the diminished strength of the feedback fields can be given by $\omega_r' = p_j \omega_r$. Since $\omega_1' >> \omega_r'$ the imbalance in the Rabi cycle is not very significant, and so the lesser component requires a significant number of cycles in order to reach the fixed point on the opposite side of the Bloch sphere. This shift in fixed points in the transverse plane is in good agreement with the approximation set forth in Eq. (9), as shown by the solid vectors in each panel.

As was the case when $\Delta p_{ij} = 0$, the number of cycles required can be reduced by increasing ω_r, as can be seen in Fig. 2C. As expected, this comes at the expense of rotating the

fixed points further away from $\omega_1 \hat{I}_x$, again in agreement with prediction. Conversely, the fixed points can be tilted back towards $\omega_1 \hat{I}_x$ by increasing ω_1 as can be seen in Fig. 2D. This increase in ω_1 further reduces the imbalance in the Rabi cycle, and consequently increases the number of required cycles before reaching the fixed points predicted in Eq. (9). While the model is crude, the evolution for each individual component can be predicted with reasonable degree of accuracy. The location of each set of fixed points can be manipulated with the competetive nature between ω_1 and ω_r, as well as the amount of time required to reach the fixed points.

4.3 Result and Discussion

The joint interaction of the CW with the feedback fields would thus be expected to generate significant contrast between two components with only a slight difference in magnetic susceptibility or resonance offset, provided the CW is placed on resonance with the average of the two components, and $\omega_1 \tau_r \sim 1$. The performance of using a CW with the active feedback circuit at 300MHz with a micro-imaging probe can be seen on the imaging of a mouse with an early tumor, grown on its right leg. The appearance of the tumor in the image (Fig. 3F) shows up much clearer than it does in the other forms of conventional imaging (Fig. 3A-D). The supposed susceptibility difference between the healthy and tumor tissues would thus be expected to be visible in a susceptibility weighted image (SWI), which weighs certain parts of an image by the acquired phase during a free evolution of the magnetization prior to acquisition. From the SWI (Fig. 3E) image, it is difficult to determine the location of the tumor from simply applying the phase mask. One explanation is because there are specific limitations in producing an effective high-frequency filter in the creation of the SWI. Unless the change in resonance offset is rapid

enough (constructed from high frequency components in Fourier space), any phase change in the magnetization runs the risk of being filtered out as background inhomogeneity. This can be remedied by allowing for longer evolution times to acquire more phase separation, at the expense of signal dephasing from T_2^* decay as well as phase wrapping of the magnetization, which requires additional imaging processing algorithms to handle the aliasing artifacts. While

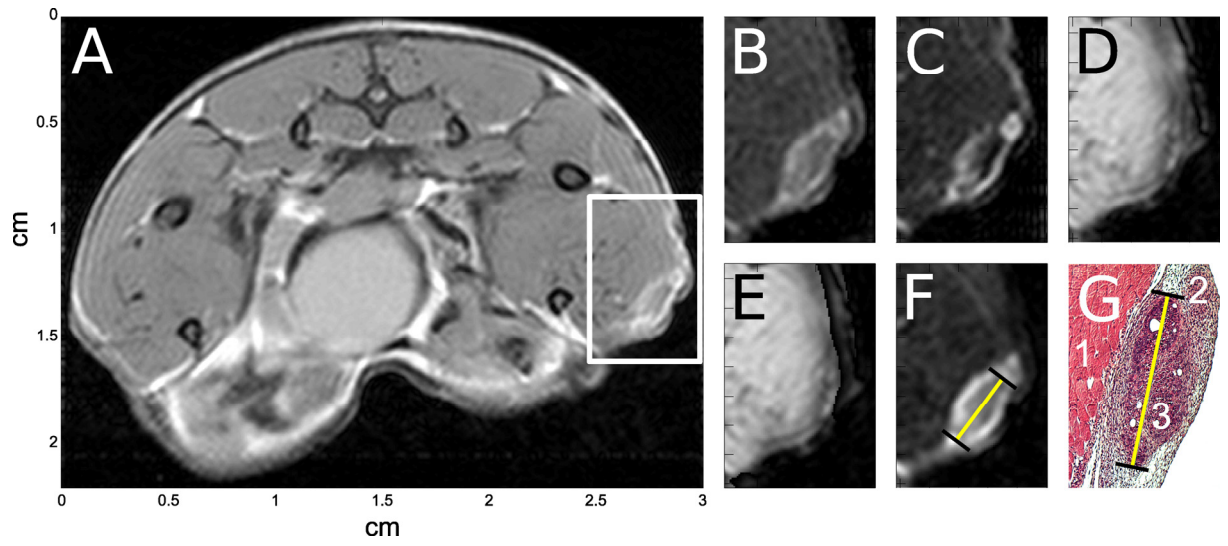

Figure 3. *In vivo* tumor imaging of a mouse implanted with human pancreatic cancers, comparing conventional imaging with imaging done with a CW in the presence of an active feedback feedback from electronic feedback-controlled circuit. (A) Proton density image, SE, TE = 10ms, (B) T_1-weighted image, SE, TI = 500ms, (C) T_2-weighted image, SE, TE = 20ms, (D) T_2^*-weighted image, GE, TE = 5ms, (E) SWI, weighting the T_2^* image by the phase mask, and (F) Active-feedback fixed-point image, with ω_1: 250Hz, and τ_r: 3ms, and τ: 50ms (G) Pathology report verifying both the presence as well as the shape and size of the tumor tissue imaged in (F) with (1) showing healthy tissue, (2) showing alive tumor tissue and (3) showing dead tumor tissue, all features that appear to be visible clearly in the active-feedback fixed-point imaging.

susceptibility information may be available from processing phase information, that sort of approach does not appear to be very robust as there are multiple concerns in the post-processing of the phase data.

4.4 Conclusion

The dynamics surrounding the evolution of a sample in the presence of feedback fields has been examined for simple two-component systems. The phase difference between both components can be encoded into the phase of the sample magnetization, and measured via standard MRI techniques. Understanding the quantum dynamics and how to manipulate them can be useful for imaging purposes where the relaxation behavior of the sample destroy the long term stability of the fixed points. Despite the destructive nature of relaxation, the system will still evolve in such a way as to minimize the total energy of the system. As a result, the dynamics *en route* to the fixed points can still be useful for imaging contrast as each component is seen to repel each other because of the passive/active feedback fields. The use of a CW in the presence of feedback fields can thus be used to highlight regions or tissues with only a slight difference in magentic susceptibility or resonance offset. The amplitude of the feedback fields can be arbitrarily set to interfere with the CW in such a way as to optimize the contrast. In vivo MR images from mice cancer models suggest that this new approach successfully finds early-stage tumors more consistently than the other conventional imaging modalities, including conventional susceptibility weighted imaging.

4.5 Reference

[1] N. Bloembergen, R. V. Pound, *Phys. Rev.* **95**, 8 (1954).

[2] S. Bloom, *J. Appl. Phys.* **28**, 800 (1957).

[3] G. Brownell, W. Sweet, *Nucleonics* **11**, 40 (1953).

[4] S. Datta, S. Y. Huang, Y.-Y. Lin, *J. Phys. Chem. B.* **110**, 22071 (2006).

[5] R. R. Ernst, G. Bodenhausen, A. Wokaun, *Principles of Nuclear Magnetic Resonance in One and Two Dimensions* (Oxford Science, 1987).

[6] R. R. Ernst, W. A. Anderson, *Rev. Sci. Inst.* **37**, 93 (1966).

[7] E. Haacke, R. Brown, M. Thompson, R. Venkatesan, *Magnetic Resonance Imaging: Physical Principles and Sequence Design* (Wiley, 1999).

[8] S. Y. Huang, *et al.*, *Magn. Reson. Med.* **56**, 776 (2006).

[9] S. Y. Huang, J. K. Furuyama, Y.-Y. Lin, *Magn. Reson. Mater. Phy.* **19**, 333 (2006).

[10] G. P. Jones, *Phys. Rev.* **148**, 332 (1966).

[11] Y.-Y. Lin, N. Lisitza, S. Ahn, W. S. Warren, *Science* **290**, 118 (2000).

[12] I. I. Rabi, *Phys. Rev.* **51**, 652 (1937).

[13] W. S. Warren, S. L. Hammes, J. L. Bates, *J. Chem. Phys.* **91**, 5895 (1989).

[14] W. S. Warren, *et al.*, *Science* **281**, 247 (1998).

Chapter 5

Fixed-Point Imaging for Early Cancer Detection: Classical Description

5.0 Abstract

The competing nature of a continuous wave and the passive or active feedback field is shown to create stable fixed points, which act as attractive basins for spin evolution. These fixed-points have been previously shown to be useful in the early detection of tumors in mice, more effectively than current conventional methodologies. A classical generalized theory is presented to explain the physical origin behind the fixed-points as well as how a system starting from equilibrium arrives at the fixed points. Understanding the origins and development of the fixed points allows for pulse sequence modification to further take advantage of these fixed-points. With the implementation of an active feedback circuit, the development of the fixed points can be strategically moved along a different axis than with the natural radiation damping.

5.1 Introduction

The study of non-linear dynamics spans a wide range of fields, from local animal populations to spin evolution in magnetic resonance. While non-linear dynamics in magnetic resonance have been studied extensively, the mention of fixed-points typically is excluded from discussion. In dynamical analysis, fixed points are locations in phase space where the evolution of a system is said to cease, without any additional external forces. The stability of such fixed points can be rigorously analyzed, providing enriching information behind the nature and origin

of the fixed points themselves. The study of fixed points and stability in magnetic resonance has been used to evaluate the effectiveness of specific iterative excitation schemes [16]. Linear stability analysis has also been used to investigate the instabilities between the distant dipolar field (DDF) and radiation damping [12], which have been shown to jointly produce chaotic dynamics at high fields [13]. Understanding the instability of initial conditions has been used to develop non-linear evolution schemes which can be used to amplify small differences in resonance offset [5], such as is the case between white and gray matter in the brain [11, 10].

It has been recently shown that continuous wave (CW) irradiation conspires with the radiation damping feedback field to produce fixed points which has applications in early tumor detection [6, 7]. While the long-term stability of the fixed-fixed points is obstructed by both longitudinal and transverse relaxation, the magnetization will still evolve towards the attractive fixed-points, typically on opposite sides of the Bloch sphere. In this chapter, we discuss the physical origin and development of the fixed-points, and how understanding of the principles can be useful for pulse-sequence design. Section 2 gives a brief overview of non-linear phenomena, specifically the phenomena surrounding the radiation damping feedback field. Section 3 is split into two parts, one discussing the physical origin of the fixed points, and the other analyzing how the system evolves in order to develop the fixed points when starting from an otherwise unstable state. Finally, section 4 discusses future and potential applications of the fixed-point phenomena with the aid of an active-feedback circuit, which is designed to emulate and manipulate the natural radiation damping field, opening new doors for non-linear analysis. All presented numerical simulations were calculated using the MATLAB (*The Mathworks*, Natick, Massachusetts) software package. Phantom imaging experiments were performed on a Bruker Avance, 600MHz spectrometer equipped with micro-imaging capability.

5.2 Nonlinear Evolution

Within a rotating frame of reference, rotating at the Larmor frequency, $\omega_0 = \gamma B_0$, the macroscopic evolution of a normalized spin component is well-characterized by the modified Bloch equations [2]

$$\frac{\partial \vec{m}(\vec{r},t)}{\partial t} = \gamma \vec{m}(\vec{r},t) \times \left[\frac{\delta\omega(\vec{r})}{\gamma} \hat{\mathbf{z}} + \vec{B}(\vec{r},t) \right] - \frac{m_z - 1}{T_1} \hat{\mathbf{z}} - \frac{m_x \hat{\mathbf{x}} + m_y \hat{\mathbf{y}}}{T_2} + D\nabla^2 \vec{m}(\vec{r},t) \qquad (1)$$

where γ is the gyromagnetic ratio, $\delta\omega = \omega - \omega_0$ is a resonance offset difference from the Larmor frequency, $\vec{B}(\vec{r},t)$ represents the local field within the rotating frame, T_1 and T_2 are the corresponding longitudinal and transverse relaxation times respectively, and D is the self-diffusion constant. Typically the applied magnetic fields are independent of the instantaneous magnetization, rendering Eq. (1) an ordinary linear differential equation, as all terms are of first order with respect to the magnetization. The linearity of Eq. (1) makes it possible to determine analytical solutions for the trajectory of the magnetization. However, in the event that the applied field is dependent on the instantaneous distribution of the sample magnetization, Eq. (1) becomes non-linear, as the cross product is no longer of first order with respect to $\vec{m}(\vec{r},t)$. This makes it practically impossible to find a generalized analytical solution as the entire trajectory is highly dependent on the initial conditions, and is often only solvable by numerical methods. The more familiar magnetization-dependent fields are the DDF and radiation damping. The use of an electronic feedback circuit, which is non-linear by nature, has been shown to be useful in the suppression of radiation damping, in order to prevent instabilities in spin evolution [4, 14]. Additionally, altering the phase of the electronic feedback has been shown to enhance the natural radiation damping effect for contrast enhancement purposes, and under specific conditions, leading to potentially chaotic dynamics for simple-spin systems [1].

Both the radiation damping field and electronic feedback can be modeled as a time-dependent magnetic field, given by [17, 9]

$$\gamma\vec{B}_{+,rd}(t) = \frac{ie^{-i\varphi}}{\tau_r V}\int_V \vec{m}_+(\vec{r},t)\, d^3\vec{r} \tag{2}$$

where $\vec{B}_+ = B_x + iB_y$ and $\vec{m}_+ = m_x + im_y$, φ is the tuning-dependent phase of the applied radiation damping [9], and τ_r is the radiation damping time constant, and represents the strength of the radiation damping. For natural radiation damping, $\tau_r = (2\pi\eta M_0 Q\gamma)^{-1}$, where η and Q are the filling and quality factors of the probe respectively. For a perfectly tuned probe, $\varphi = 0$, corresponding to the radiation damping lagging by a factor of $\pi/2$ behind the total transverse magnetization (compare this with Abergel's notation, which omits the i in front of the exponent, making $\varphi = -\pi/2$ correspond to the natural radiation damping). In the electronic feedback circuit, both φ and τ_r are tunable, giving rise to a whole new subset of non-linear dynamics. In the case limiting that $\varphi = \pi$, the feedback is applied out of phase such that the natural radiation damping can be suppressed, restoring the linearity to Eq. (1). It can be seen that the net effect of Eq. (2) in Eq. (1) is to respond to the net magnetization by rotating it back towards the equilibrium $+z$ orientation.

The physical origin of this effect has been discussed in great detail on many accounts [3, 18, 8, 15] and will only be highlighted in this paper. By Lenz's law, an induced current in a receiver coil creates a reactionary field which acts back onto the sample, nutating it back towards the equilibrium $+z$ position. An alternative explanation for the effect is that the current induced in the receiver coil requires energy that must be supplied by the system. Since the most energetically stable orientation of the magnetization is the $+z$ orientation, as more energy is coupled out of the system, the magnetization is forced back towards the $+z$ axis in order to

conserve energy. Both simplified pictures, one electromagnetic in origin, the other thermodynamic, yield the exact same result, and are both accurately described by Eq. (2). It can be seen that Eq. (2) is modeled as a time-dependent magnetic field, yet is explicitly dependent on $\int \vec{m}_+(\vec{r})d^3\vec{r}$. The net evolution of the system is such that the energy of the system will always be minimized if possible due to the radiation damping. Since the radiation damping is activated when $\int \vec{m}_+(\vec{r})d^3\vec{r} \neq 0$, the system will naturally evolve in order to minimize $\int \vec{m}_+(\vec{r})d^3\vec{r}$.

5.3 Fixed-Points with Passive Feedback Fields

Understanding both the physical origin as well as the development of the fixed points is crucial in order to fully take advantage of these dynamics. While the origin and development can both be explained within the context of Eq. (1), it will be shown that the physical origin and the actual development of the fixed points are completely independent of each other, greatly simplifying the discussion. Though a more thorough density operator treatment is much more transparent regarding the physical origin and derivation of the fixed points, this discussion is limited to a classical treatment in order to keep things as simple as possible.

5.3.1 Physical origin

At a fixed-point, there is said to be no spin evolution. This of course occurs when $\partial\vec{m}/\partial t = 0$ in Eq. (1). Ignoring relaxation terms, it can be seen that $\vec{m}(\vec{r},t)\times\vec{B}(\vec{r},t) = 0$ only when $\vec{m}(\vec{r},t) \,||\, \vec{B}(\vec{r},t)$ or trivially when $\vec{B}(\vec{r},t) = 0$. For a single component, the natural radiation damping ($\varphi = 0$) reduces to $\gamma\vec{B}_{+,rd}(t) \propto i\vec{m}_+(t)$. The imaginary number, i represents a 90° phase shift in the complex plane, making $\vec{B}_{+,rd}(t) \perp \vec{m}_+(\vec{r},t)$. Consequently, it can be seen that in the

absence of any additional fields, $\vec{m}(\vec{r},t)\times\vec{B}(\vec{r},t)=0$ only if $\vec{m}_{+}(\vec{r},t)=0$, which is only the case when $m_z=\pm 1$. Linear analysis (as well as conservation of energy) reveal that the $m_z=-1$ orientation is an unstable fixed-point, whereas $m_z=+1$ is stable, as would be expected at equilibrium. This particular example of a fixed point in the presence of radiation damping is seemingly trivial, as there is little interesting with regards to a system returning to the equilibrium position.

Warren has previously shown that for a single-spin system, the application of a CW in the presence of radiation damping yields unexpected dynamics and shifted fixed points when the CW is placed off-resonance [18]. Within the appropriate frame of reference, a CW can be modeled as a static field vector, $\gamma\vec{B}_{cw}=\omega_1\hat{\mathbf{x}}$, and so the effective field in the rotating frame simply becomes $\gamma\vec{B}_e=\omega_1\hat{\mathbf{x}}+\delta\omega\hat{\mathbf{z}}$. It was shown that in the presence of radiation damping, solutions for $\partial\vec{m}/\partial t=0$ were not for $\vec{m}\,||\,\vec{B}_e$, but rather shifted depending on the strength of the radiation damping and how off-resonance the CW was placed with respect to the magnetization. There were shown to be two fixed-points, one stable, and one unstable, both of which are not aligned with B_0. For one component, Eq. (1) can be broken down into 3 separate equations and solved for simultaneously. Since there is only one component, the integral in Eq. (2) collapses and the additional radiation damping term in Eq. (1) is easy to manage.

The situation becomes increasingly complex as more components are added to the system. Each extra component requires 3 additional equations which need to be solved simultaneously with all the other equations. Even for two simple components, evaluation of the integral in Eq. (2) becomes tricky as the relative volume densities for each component becomes important. For mathematical simplicity, we will start with the most basic two component case in

which each component has equal contribution to the integral in Eq. (2). Each component is distinguished by having a resonance offset difference, $\Delta\omega_{ij} = |\delta\omega_i - \delta\omega_j|$, where the *i*/*j* subscript notation is simply to differentiate between the *i* th and *j* th spins. The CW frequency is placed directly between both components such that $\delta\omega_i = -\delta\omega_j = \delta\omega$, and so $\Delta\omega_{ij} = 2|\delta\omega|$. The corresponding effective field for each component is just

$$\gamma\vec{B}_{e,i/j} = \omega_1 + Re\left[\frac{ie^{-i\varphi}}{\tau_r V}\int_V \vec{m}_+(\vec{r},t)\, d^3\vec{r}\right]\hat{\mathbf{x}} + Im\left[\frac{ie^{-i\varphi}}{\tau_r V}\int_V \vec{m}_+(\vec{r},t)\, d^3\vec{r}\right]\hat{\mathbf{y}} + \delta\omega_{i/j}\hat{\mathbf{z}} \tag{3}$$

In the limit that radiation damping is negligible compared to the CW ($\omega_1\tau_r >> 1$), the integrals in Eq. (3) disappear, and the effective field for two components thus reduces to

$$\gamma\vec{B}_{e,i/j} = \omega_1\hat{\mathbf{x}} + \delta\omega_{i/j}\hat{\mathbf{z}} \tag{4}$$

Ignoring the coupling from the radiation damping, it can be seen that there are two fixed points for each spin component, one that is aligned parallel to $\vec{B}_{e,i/j}$, which will be denoted $\psi_{i/j} = |+\rangle$ and one aligned anti-parallel, denoted as $\psi_{i/j} = |-\rangle$. There are thus four possible sets of fixed points, ψ_{ij}, in the absence of radiation damping, $|{+}{+}\rangle$, $|{+}{-}\rangle$, $|{-}{+}\rangle$, and $|{-}{-}\rangle$. All four of these sets are neither attractive/stable nor repulsive/unstable, as slight perturbations, $\lambda\psi$, do not produce any particularly interesting dynamics. Any given state, $\psi_{ij}' = \psi_{ij}^{(0)} + \lambda\psi$ will simply precess around $\psi_{ij}^{(0)}$ at a frequency of $\gamma\vec{B}_e$, as governed by Eq. (1), which is still linear for uncoupled spins. The superscript (0) notation is used simply to represent the unperturbed fixed-point.

For strong radiation damping (strong enough such that $\omega_1\tau_r \sim 1$), the integral in Eq. (3) cannot be ignored and is thus in direct competition with the CW. The stability of for each fixed-point, ψ_{ij}, can thus be re-evaluated with the full form of Eq. (3). For the remaining discussion,

the state $\psi_{ij} = |{+}{+}\rangle$ will be abbreviated as ψ_{++}, as well as for the other fixed-points. For both ψ_{++} and ψ_{--}, it can immediately be seen that $\int \vec{m}_+(\vec{r}) d^3\vec{r} \neq 0$ since both components have a coherent transverse projection. By Eq. (2), this results in $\vec{B}_{rd,+} \neq 0$, which is applied 90° out of phase with $\int \vec{m}_+(\vec{r}) d^3\vec{r}$, as can be seen in Fig. 1A. Consequently, it can be seen that the fixed-point condition, that $\psi_{ij} \| \vec{B}_e$, no longer holds for either component in both the ψ_{++} and ψ_{--} states, destroying these orientations as fixed-points. The situation is different, however, for the ψ_{+-} and ψ_{-+} states. As can be seen in Fig. 1B, both components are pointed anti-parallel to each other in the transverse plane, resulting in $\int \vec{m}_+(\vec{r}) d^3\vec{r} = 0$. This leaves $\vec{B}_{rd,+} = 0$, and so Eq. (3) reduces to Eq. (4), as is the case for $\omega_1 \tau_r >> 1$ (negligible radiation damping). Consequently, both the ψ_{+-} and ψ_{-+} states are preserved as fixed points with the addition of radiation damping. One particular distinction from the negligible radiation damping case is that for $\omega_1 \tau_r \sim 1$, the ψ_{+-} and ψ_{-+} states become stable and unstable fixed points. For $\delta\omega_i > 0$, the ψ_{+-} state is the stable fixed point whereas the ψ_{-+} state is unstable. This means that for $\psi_{+-}' = \psi_{+-}^{(0)} + \lambda\psi$, the system will evolve in such a way as to converge back towards the $\psi_{+-}^{(0)}$ orientation, making it stable. The opposite is true for the ψ_{-+} state, where for $\psi_{-+}' = \psi_{-+}^{(0)} + \lambda\psi$, any value for which $\lambda \neq 0$, the system will evolve towards the $\psi_{+-}^{(0)}$ state, meaning the system will never be found in the $\psi_{-+}^{(0)}$ state unless it starts there. As a result, the rest of this paper is primarily concerned with the $\psi_{+-}^{(0)}$ state since it is stable, and so the $+/-$ subscript notation will be dropped unless otherwise needed for distinction.

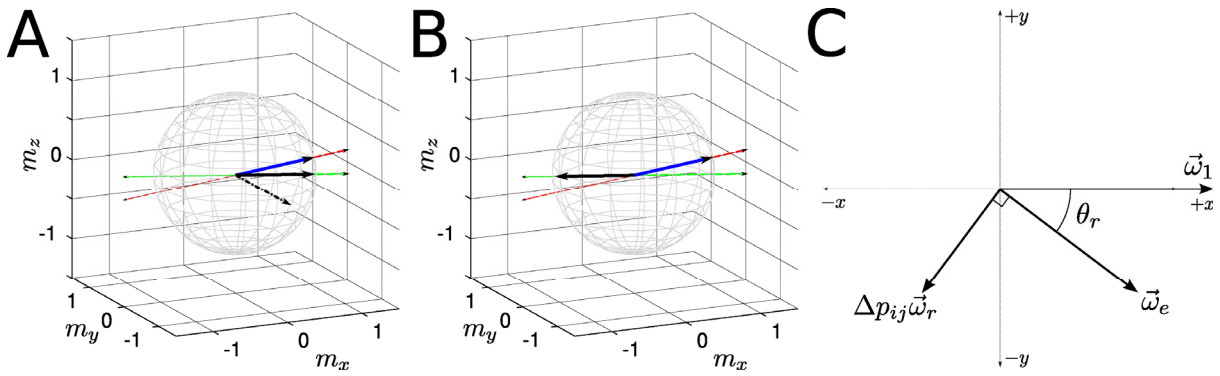

Figure 1. (A) 3-dimensional orientations of the ψ_{++} state with both components (solid vectors) aligned along the effective field denoted by the the dashed vectors. Both components are facing the same direction such that $\int \vec{m}_+(\vec{r})d^3\vec{r} \neq 0$, resulting in the application of an additional magnetic field vector our of phase with $\int \vec{m}_+(\vec{r})d^3\vec{r}$ by a factor of $\pi/2$, shown by the dotted-dashed vector. The addition of the radiation damping vector prevents this ψ_{++} state from being a fixed point. (B) 3-dimensional orientations of the ψ_{-+} state with one component aligned parallel to the effective field, and the other component aligned anti-parallel to the effective field. The transverse projection for both components are anti-parallel to each other such that $\int \vec{m}_+(\vec{r})d^3\vec{r} = 0$, corresponding to $\vec{B}_{+,rd} = 0$. (C) 2-dimensional plot showing the tip-angle, θ_r of the effective field, $\vec{\omega}_e$, in the presence of the reduced radiation damping field, $\Delta p_{ij}\vec{\omega}_r$ away from $\vec{\omega}_1$, the CW. As defined in Eq. (6), increasing $\Delta p_{ij}\omega_r$ with respect to ω_1 increases the tip angle θ_r, or vice versa. Clearly, in the limit that $\Delta p_{ij} \to 0$, $\theta_r \to 0$ as is for the even component cases.

The discussion is further complicated if both components in either the ψ_{+-} or ψ_{-+} states do not have equal contributions to Eq. (2), leaving $|\int \vec{m}_+(\vec{r})d^3\vec{r}| = \Delta p_{ij} \neq 0$, where $\Delta p_{ij} = |p_i - p_j|$ represents the difference in proportion between the two uneven components. A new subscript notation will be introduced to help distinguish between the even component fixed points (ψ_0), and the new fixed points ($\psi_{\Delta p}$) for $\Delta p_{ij} \neq 0$. Since $\int \vec{m}_+(\vec{r})d^3\vec{r} \neq 0$, it can be seen that the effective field is once again described by Eq. (3). It can thus be seen that the effect of the radiation damping rotates $\vec{B}_{+,e}$ away from Eq. (4) by an angle of θ_r, as can be seen in Fig. 1C. Tipping the effective field away from ψ_0 creates a new fixed point where $\psi_0 = \psi_{\Delta p}^{(0)} + \lambda\psi$, implying that the original fixed points are now simply a slight perturbation away from the new fixed points $\psi_{\Delta p}$, and so it would be expected that $\psi_0 \to \psi_{\Delta p}$ since it is stable. The difficulty is thus determining the orientation of $\psi_{\Delta p}$ since it is dependent on ω_1, $\omega_r = \tau_r^{-1}$, and $\delta\omega$. The analysis can be simplified under the constraint that $\sqrt{\omega_1^2 + (\Delta p_{ij}\omega_r^2)} ? \delta\omega$, namely, we are more interested with the interplay between the CW and the radiation damping than we are with any effects resulting from significantly large resonance offsets. Since the CW and radiation damping vectors are only applied in the transverse plane, it can be seen that any rotation of $\vec{B}_{+,e}$ must be accompanied by a rotation of ψ_0 such that

$$\psi_{\Delta p} \cong R_z(\theta_r)\psi_0 \tag{5}$$

where $R_z(\theta_r)$ is simply a rotation around the $+z$ axis by an angle of θ_r. Considering that in order to remain a fixed-point, the condition that $\psi_{\Delta p} \,||\, \vec{B}_e$ must still be met, along with the fact that $\vec{B}_{rd} \perp \int \vec{m}_+(\vec{r})d^3\vec{r}$, it can be seen by simple geometric argument that the value for θ_r must be

$$\theta_r \cong \sin^{-1}\left[\frac{\Delta p_{ij}\omega_r}{\omega_1}\right] \tag{6}$$

As a result, it can be seen that the more uneven the two components are, or the stronger the radiation damping is, $\psi_{\Delta p}$ will be tipped further away from ψ_0. Conversely, tip angle of $\psi_{\Delta p}$ away from ψ_0 can be reduced by increasing the strength of the CW. Balancing these parameters is not only necessary for the determining the orientation of $\psi_{\Delta p}$, but it will be shown in the next section that all of these parameters also influence how the system arrives at these fixed points.

5.3.2 Role of active feedback fields in evolution

The ψ_{+-} state for the even case can be rewritten in Cartesian space $\{\hat{\mathbf{x}}, \hat{\mathbf{y}}, \hat{\mathbf{z}}\}$, as as

$$\psi_{+-} \rightarrow \begin{cases} m_i &= \aleph_i^{-1}\{\omega_1, 0, \delta\omega_i\} \\ m_j &= -\aleph_j^{-1}\{\omega_1, 0, \delta\omega_j\} \end{cases} \tag{7}$$

where $\aleph_{i/j} = \sqrt{\omega_1^2 + \delta\omega_{i/j}^2}$ is simply a normalizing factor. While the formation of the ψ_{+-} state depends explicitly on the presence of radiation damping, it can be seen from Eq. (7) that the orientation of the even-component fixed-point is independent of τ_r. The formation of the fixed points required that the steady-state solution for Eq. (1) minimize $\int \vec{m}_+(\vec{r}) d^3\vec{r}$ as much as possible, independently of the strength of the radiation damping, hence the ψ_{+-} state being fixed even for $\omega_1\tau_r >> 1$ even though it was neither stable nor unstable. Because of the non-linearity of Eq. (1), even small changes in τ_r would be expected to change the dynamics *en route* to the fixed points, yet resulting in the same fixed point as defined by Eq. (7). Before analyzing the development of the fixed points themselves, it is useful to determine the interaction between a CW and the radiation damping.

The effect of radiation damping can be recast in spherical coordinates (where $0 \le \theta \le \pi$, and $0 \le \phi \le 2\pi$) as

$$\frac{\partial \theta}{\partial t} = -\frac{1}{\tau_r}\sin(\theta) \tag{8}$$

where the net effect is to nutate the magnetization back towards the $+z$ orientation for $\theta \neq 0, \pi$. The effect of a CW is to excite the magnetization away from the $+z$ position ($\partial\theta/\partial t = \omega_1$) until $\theta(t) = \pi$, to which the CW proceeds to excite that magnetization back towards the $+z$ orientation ($\partial\theta/\partial t = -\omega_1$) where $\theta(t) = 0$. In the absence of radiation damping, it can be seen that both excitations away from and towards the $+z$ orientation require the same amount of time, $\tau = (2\omega_1)^{-1}$. Inspecting the sign of $\partial\theta/\partial t$ for both excitations, it can be seen that the radiation damping destructively interferes with the CW when being excited away from the $+z$ orientation, and constructively interferes with the CW when being excited back towards the $+z$ orientation. As a result, it can be seen that the amount of time required to excite the magnetization down towards the $-z$ orientation is going to be $\tau_\downarrow > (2\omega_1)^{-1}$, whereas the time required to excite the magnetization back towards the $+z$ orientation is $\tau_\uparrow < (2\omega_1)^{-1}$. This leads to an uneven Rabi cycle, as can be seen by analyzing the $m_z = \cos(\theta)$ component of the magnetization, as can be seen in Fig. 2A. The dotted-dashed line shows the effect of the CW in the absence of radiation damping (or for $\omega_1\tau_r >> 1$), as a simple sinusoidal oscillation, with a period of 20 ms (50 Hz). The solid line shows the effect of strong radiation damping ($\omega_1\tau_r \sim 1$), where the excitation towards the $-z$ orientation takes significantly longer ($\sim$ 41 ms) than the excitation back towards the $+z$ orientation ($\sim$ 6 ms).

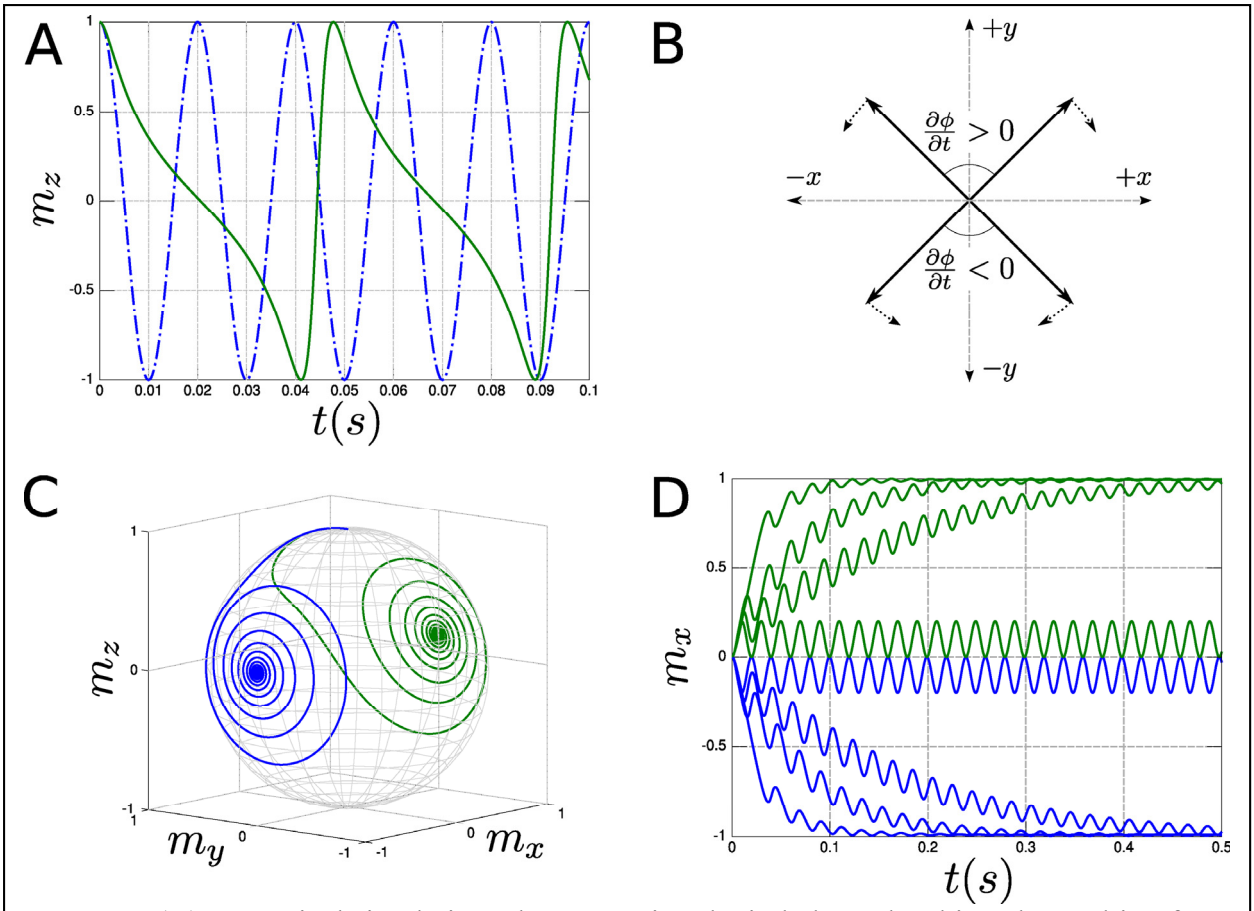

Figure 2. (A) Numerical simulations demonstrating the imbalanced Rabi cycle resulting from the CW interference produced by radiation damping. The dotted-dashed line shows a typical Rabi cycle ($\tau_r \to \infty$) for a CW with $\omega_1 = 50\,\text{Hz}$ for which $\tau_\downarrow = \tau_\uparrow = 10\,\text{ms}$. The solid line shows an imbalanced Rabi cycle with $\tau_r = 3.5\,\text{ms}$ for the same CW for which $\tau_\downarrow \approx 41\,\text{ms}$ and $\tau_\uparrow \approx 6\,\text{ms}$. (B) Diagram showing the acquired phase between two components depending on the hemisphere, where the two components acquire a positive phase, $\partial\phi/\partial t > 0$, in the $+y$ hemisphere and a negative phase, $\partial\phi/\partial t < 0$, in the $-y$ hemisphere. Since $\tau_\downarrow = \tau_\uparrow$ when $\tau_r \to \infty$, the acquired positive phase during the first half of the cycle is perfectly cancelled out by the negative phase acquired during the second half of the cycle. In the presence of radiation damping, $\tau_\downarrow > \tau_\uparrow$, and so the acquired positive phase during the first half of the cycle is not fully cancelled out by the negative phase acquired during the second half of the cycle. (C) 3-dimensional trajectory for a two-component system, where the resonance offset difference between the two components is $\Delta\omega_{ij} = 10\,\text{Hz}$, the CW is placed directly between both components such that $\delta\omega_i = -\delta\omega_j = -5\,\text{Hz}$, $\omega_1 = 50\,\text{Hz}$, and $\tau_r = 3\,\text{ms}$. Both components have the appears of repelling each other towards opposite poles on the Bloch sphere, as predicted by Eq. 7. (D) Comparison of the same system in **C** with different values of τ_r = 3, 6, and 12ms, as well as $\tau_r \to \infty$ to demonstrate the effect of radiation damping strength and the amount of time (as well as imbalanced Rabi cycles) required to arrive at the fixed points.

This uneven Rabi cycle is what allows the two components to reach their eventual fixed points as predicted by Eq. (7). As both components are excited by the CW, $\vec{B}_{cw} = \omega_1 \hat{\mathbf{x}}$, into the $+y$ hemisphere, they will begin to precess away from each other, acquiring a positive phase between them, as can be seen geometrically in Fig. 2B. Once the magnetization passes through the $-z$ orientation into the $-y$ hemisphere, it can be seen that the two components will start to rephase back towards each other, acquiring a negative phase. For negligible radiation damping, since both excitations away from and towards the $+z$ position require the same amount of time, $\tau_{\downarrow} = \tau_{\uparrow} = (2\omega_1)^{-1}$, the acquired phase after one full rotation is going to be zero. For strong radiation damping, it can be seen that since $\tau_{\downarrow} > \tau_{\uparrow}$, there is going to be a net phase accumulation after one full Rabi cycle. Subsequent rotations by the CW allow for further phase accumulation until the components arrive at their respective fixed points on opposite sides of the Bloch sphere, as can be seen three-dimensionally in Fig. 2C. The amount of phase accumulation after one full rotation depends explicitly on imbalance resulting from the interference produced by the radiation damping. Clearly, a larger imbalance (created by stronger radiation damping) produces a greater phase accumulation per cycle, thus requiring fewer rotations in order to reach the fixed points. Consequently, reducing the strength of the radiation damping reduces the imbalance in the Rabi cycle, requiring more rotations before reaching the fixed points, as can be seen in Fig. 2D. As can be seen, in the limit that $\tau_r \to \infty$, the number of rotations required to reach the fixed points is infinite, as both components will never reach the fixed points. The number of rotations required to reach the fixed points is thus proportional to the radiation damping time constant, provided $\omega_1 \tau_r \sim 1$.

It can be seen in Figs. 2C-D that the magnetization evolves until the system arrives at the stable ψ_{+-}, state or fixed point, where all motion stops. In fact, there is no way for the system to ever settle at the unstable ψ_{-+} state unless the system were to start there. It can be seen in Fig. 2, that even for infinitesimally small values of λ in $\psi_{-+} = \psi_{-+}^{(0)} + \lambda\psi$, the system evolves directly towards the $\psi_{+-}^{(0)}$ state [Eq. (7)] and remains there. The ψ_{-+} state is denoted for each component as the dashed vectors, where the ψ_{+-} state is denoted by the solid vectors. In the absence of relaxation, the components are confined to the surface of the Bloch sphere, and so it can clearly be seen that the ψ_{+-} state (or $\psi_{\Delta p}$ state for uneven components) represents a global fixed-point that the system will naturally evolve towards, independent of the starting point. So while the specific trajectory is highly sensitive to the initial conditions, the fixed points can start from anywhere, even infinitesimally near the the unstable fixed points.

5.3.3 Uneven cases and multiple components

While discussing even-component situations is useful to understand how the fixed points develop, it is more practical to consider more realistic situations, where the two components do not have equal contribution, or for *in vivo* considerations where there are more than two components. It turns out that the discussion regarding uneven components can be broadly extended with regards to multiple components. As shown in Eqs. (5) and (6), the location of the fixed points shifts away from the ψ_{+-} state depending on the balance between ω_1, $\delta\omega$, and τ_r and Δp_{ij}.

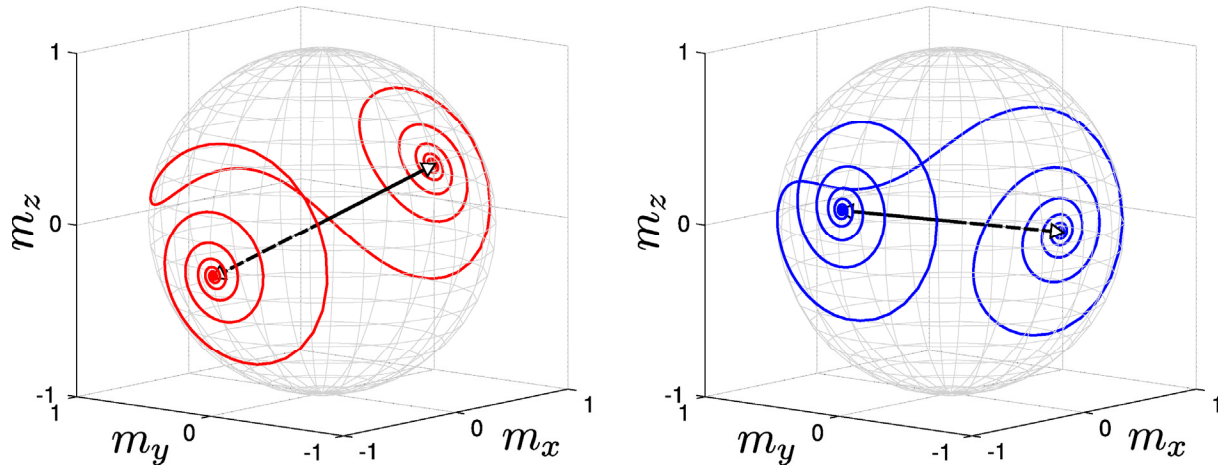

Figure 3. Numerical simulations demonstrating the unstable and repulsive properties of each component (plotted separately) in the ψ_{-+} state as well as the stable and attractive properties of the ψ_{+-} state. The orientation of the ψ_{-+} state is denoted by the dashed vectors in both panels, where the ψ_{+-} state is represented by the solid vector lines. The relevant parameters are $\Delta\omega_{ij} = 20$ Hz, $\omega_1 = 50$ Hz, and $\tau_r = 3$ ms. The perturbation, $\lambda\psi$, was made by adding 1×10^{-4} to each component along the m_y direction such that λ is very small. The presence of a seemingly insignificant perturbation is sufficient to repel the system away from the ψ_{-+} orientation, bringing the system straight towards the ψ_{+-} state because it is stable. Consequently, the system will never be found in the ψ_{-+} state unless the components are allowed to start exactly along that orientation.

Consider a very simple uneven two-component case such that the relative ratio of contribution to Eq. (2) is 4:1, shown in Fig. 3A. The translverse evolution of this particular system with $\omega_1 = 50\,\text{Hz}$ and $\tau_r = 3\,\text{ms}$ is shown in Fig. 3D. For these particular parameters, the fixed points would be expected to shift away from the ψ_0 state by 39.5°, compared to the simulation value of 39.1°, within decent agreement considering Eq. (6) to be only an approximation. While the evolution of both components is completely different from the even component case, a few similarities can be seen to occur within the uneven component case.

Since the contribution of the bulk component to Eq. (2) is much more significant than the minor component, it can be understood that the evolution of the bulk component is going to evolve very similarly to a single component system, with minimal influence from the minor component. As a result, the bulk component would be expected to race towards its own single-component fixed-point, as has been previously described by Warren. The situation is significantly different for the minor component. Since the bulk component arrives at its fixed-point relatively early on, the radiation damping created by this component becomes a static vector that is offset from the CW. As a result, the minor component feels an effective-CW that is the addition of the original CW and the static radiation damping created by the bulk component. Since the minor component has a finite contribution to Eq. (2) it will feel its own [minor] radiation damping field, allowing the component to eventually reach its own fixed point on the opposite pole of the Bloch sphere. The time scale required for the components to stabilize can be understood from the effect of radiation damping on the even-component case. The bulk component feels a much stronger radiation damping field, thus creating a much larger imbalanced Rabi cycle, thus allowing the bulk component to stabilize early on. The minor component feels its own [significantly] reduced radiation damping field, barely enough to create

for an imbalanced Rabi cycle. Since the imbalance is not very severe, the minor component requires a significant number of additional rotations in order to stabilize at its own fixed point compared to the bulk component. Consequently, increasing the strength of the radiation damping can be used (via active feedback) to reduce the amount of time required to arrive at the fixed points. However, it can be seen by Eq. (6), increasing the radiation damping strength tips $\psi_{\Delta p}$ further away from ψ_0. This can be become problematic as the contrast develops along an axis that is not aligned along either m_x or m_y. It can be seen that $\psi_{\Delta p}$ can be tipped back towards the m_x axis by simply increasing the strength of the CW. This, however, has the effect of reducing the imbalance in the Rabi cycle, thus requiring more time to develop the fixed points. As a result, a balance needs to thus be found between reducing the required time to develop the fixed points, and aligning the contrast along the m_x axis. This becomes more of a concern in the presence of relaxation, which can limit the long-term stability of the fixed points.

The dynamics surrounding multiple components can be seen to simply be an extension of the principles surrounding uneven two-component systems. The minor component in the previous uneven two-component case can be split into two such that the bulk component still has the same exact contribution to Eq. (2). The two new minor components are still above the CW resonance as in the previous case, but are now separated by a few Hz, as can be seen in Fig. 3B. It can be seen in Fig. 3E, that for the same parameters used in Fig. 3D, the bulk component behaves almost identically for the multiple component case. The reason for this is that both of the minor components still have a relatively insignificant contribution to Eq. (2), and thus the bulk component still evolves almost independently of the minor components. The behavior of the two minor components can be seen to be similar to the minor component in the two component case. Since each minor component has little contribution to Eq. (2), once again, it can be seen

that these components will evolve under a new effective-CW which is formed by the addition of the CW and the static radiation damping created by the bulk component. Additionally, since the bulk component has the most significant contribution to Eq. (2), the coupling between the two minor components is insignificant, and so the dynamics of each component can be estimated independently.

Of course the exact dynamics are difficult to pin down exactly, as there is always going to be a finite contribution to Eq. 2 from the minor components, and so the bulk component cannot be treated exactly as a singular component. The non-linearity alone makes it very difficult to treat the near-infinite number of possibilities for uneven and multiple component systems. It can be seen, however, from these two simple cases that the dynamics present in even the most ideal situations can be extrapolated to help understand the underlying dynamics of more complicated systems. Multiple component systems can thus be crudely viewed as a simple two-component system, where all components that are under the resonance of the CW will shift to one hemisphere, while all the components that are above the resonance of the CW will shift towards the other hemisphere, as is illustrated in Fig. 3E. As a result, the frequency of the CW serves as an effective filter, causing under-resonance components to move towards one generalized area, and over-resonance components to move towards an opposite area. The type of contrast is thus tunable depending on the frequency of the CW, yet will still develop according to the very basic models presented herein.

To experimentally verify the dynamics, a simple phantom with different capillaries with various concentrations of acetone was constructed. The presence of finite relaxation times will inevitably limit the stability and feasibility of imaging at the fixed points. As can be seen from the simulation results in Figs. 2 and 3, there is significant contrast between the different

components long before the system ever arrives at its fixed point. Supposing the system is heading towards the fixed point, the magnetization can be imaged any time along the way. The presence of the ketone in acetone changes the local magnetic environment for the water proton, being able to shift the resonance by a few Hz. The presence of radiation damping in the spectrometer broadens the frequency spectrum, making it near impossible to resolve the specific peaks. The estimated frequency distribution considering the concentrations and volumes of the respective capillaries for the given phantom is shown in Fig. 3C. The large [pure] water peak is placed under-resonance with respect to the CW, and would thus be expected to move into one particular hemisphere (darker color), where the two smaller peaks (with acetone) are above resonance, moving them into the opposite hemisphere (lighter color). As can be seen in Fig. 3F, the larger component (bulk water surrounding the capillaries) is darker, where the components within the capillaries are lighter, as expected. The developed contrast is thus dependent on the final orientation of each respective magnetization component as opposed to the length of the vector as is the case in conventional imaging techniques.

5.4 Fixed Points with Active Feedback Fields

The explicit dependence of τ_r on the equilibrium magnetization, M_0, limits the use of natural radiation damping to high-field applications, typically on the order of 600 MHz and above. Additionally, the thermodynamic origin of the radiation damping (conservation of energy) restricts the orientation of the field to lag by a factor of $\pi/2$ out of phase with total sample transverse magnetization. With the intent of suppressing radiation damping, Jeener suggested (and later performed by Abergel) the use of an electronic feedback circuit which can retransmit the FID π radians (180°) out of phase with the radiation damping (or $3\pi/2$ behind the

magnetization) in order to destructively interfere with it. The effect thus requires active control over the phase of the transmitted feedback signal, giving rise to the φ parameter in Eq. (2), for which $\varphi = 0$ for natural radiation damping in a perfectly tuned probe. The use of such an active feedback circuit can also be used with $\varphi = 0$ in order to amplify the radiation damping, as has been done by Hwang *et al.* for contrast enhancement purposes. This is useful in low-field or low Q-factor probes, where the natural radiation damping is typically considered to be negligible. As a result, the fixed-point dynamics need not be confined to high-field application, as the effect of the radiation damping can easily be emulated at much lower fields. It can be seen, however, that for any value of $\varphi \neq 0^{\circ}, \pi$, the feedback signal leads to a variety of new and potentially useful dynamics, some useful for imaging purposes. In this section, we highlight the presence and manipulation of the fixed points resulting from a variable radiation damping phase, and how they may be used for contrast enhancement in MRI.

5.4.1 Time-dependent fixed-points

For a two-component system, the angle that $\psi_{\Delta p}$ is tilted away from ψ_0 was approximated [in Eq. (6)] strictly for natural radiation damping where $\varphi = 0$. Relaxing the restriction that the radiation damping lag behind the magnetization by $\pi/2$ to lagging by a factor of $\pi/2 - \varphi$, the tip angle of $\psi_{\Delta p}$ away from ψ_0 is readily shown to be

$$\theta_r = \cos^{-1}\left[\frac{\sqrt{\omega_1^2 - \left(\Delta p_{ij}\omega_r \cos(\varphi)\right)^2}}{\omega_1}\right] \tag{9}$$

where it can be seen that in the limit that $\varphi \to 0$, with the appropriate trig identities, Eq. (9) can be simplified to Eq. (6). For a given ratio, Δp_{ij}, and radiation damping strength, ω_r, it can be

seen that increasing either ω_1 or φ has the net effect of tipping the effective field, and consequently $\psi_{\Delta p}$ back towards ψ_0 as can be seen in Fig. 4A. Clearly in the limit that $\omega_1 \to \infty$, or at least large enough such that $\omega_1^2 >> \left(\Delta p_{ij}\omega_r\right)^2$, $\theta_r \to 0$. Unfortunately, this breaks the previous condition that $\omega_1 \tau_r \sim 1$, meaning the CW completely overrides the radiation damping, preventing the imbalanced Rabi cycle that is necessary for the system to arrive at the fixed points. Trivially, allowing $\omega_r \to 0$ has the same effect as taking $\omega_1 \to \infty$, leading to no stable fixed points. Lastly, setting $\varphi = \pi/2$ lets $\theta_r = 0$. While this brings the fixed points back towards the ψ_0 orientation, the effect of setting $\varphi = \pi/2$ does not produce an imbalanced Rabi cycle, which again, is needed to arrive at the fixed points. As can be seen in Fig. 4B, starting from equilibrium, the two components are never able to stabilize at their respective fixed points, and continue to evolve, never reaching a stable or consistent trajectory. Consequently, there is no way, starting from equilibrium, to take advantage of Eq. (9) in order to bring the components back towards the ψ_0 state, as none of the options provide the necessary imbalanced Rabi cycle.

The problem with the above approach is that manipulating ω_1, ω_r or φ all have the effect of minimizing the imbalanced Rabi cycle, preventing the system from being able to reach any fixed point at all. We thus propose a time-dependent fixed-point scheme, aimed at strategically moving the fixed points to a desired location after the initial fixed point has been achieved. Once the system has settled at a fixed point, $\psi_{\Delta p}$, the values for ω_1 ω_r or φ can be infinitesimally changed such that there exists a new set of fixed points $\psi_{\Delta p}' = \psi_{\Delta p} + \lambda\psi$. Provided λ is small, it can be seen that $\psi_{\Delta p} \to \psi_{\Delta p}'$ without the need of an imbalanced Rabi cycle since the system is already within the vicinity of the new fixed point. Immediately

following, new values can be chosen such that $\psi_{\Delta p}' \rightarrow \psi_{\Delta p}''$ and so on. Since $\psi_{\Delta p}$ is defined as a simple rotation of the ψ_0 state by an angle of θ_r (Eq. 5), ω_1, ω_r or φ can be theoretically manipulated such that $\psi_{\Delta p} \rightarrow \psi_0$. Figure 4C shows a two-step process for which the first step involves bringing the magnetization to the initial fixed points, $\psi_{\Delta p}$, similar to Fig. 3D. Immediately following, φ is gradually increased to $\varphi = \pi/2$ as well as gradually increasing ω_1, which can be seen from Eq. (9) (or Fig. 4A) to decrease the value for θ_r. The dashed line shows the trajectory of $\psi_{\Delta p}'$ as it is rotated back towards the ψ_0, denoted by the dashed vectors aligned along the x-axis. The system cannot be brought exactly to the ψ_0 orientation, as this particular state was strictly defined for the even component case. It is still remarkable, howver, that the tip angle can be strategically manipulated in order to bring the magnetization to a location of choice. It can thus be seen that using the attractive nature of the fixed-points, the system can be made to follow a specific trajectory once the system reaches an initial fixed point, $\psi_{\Delta p}$.

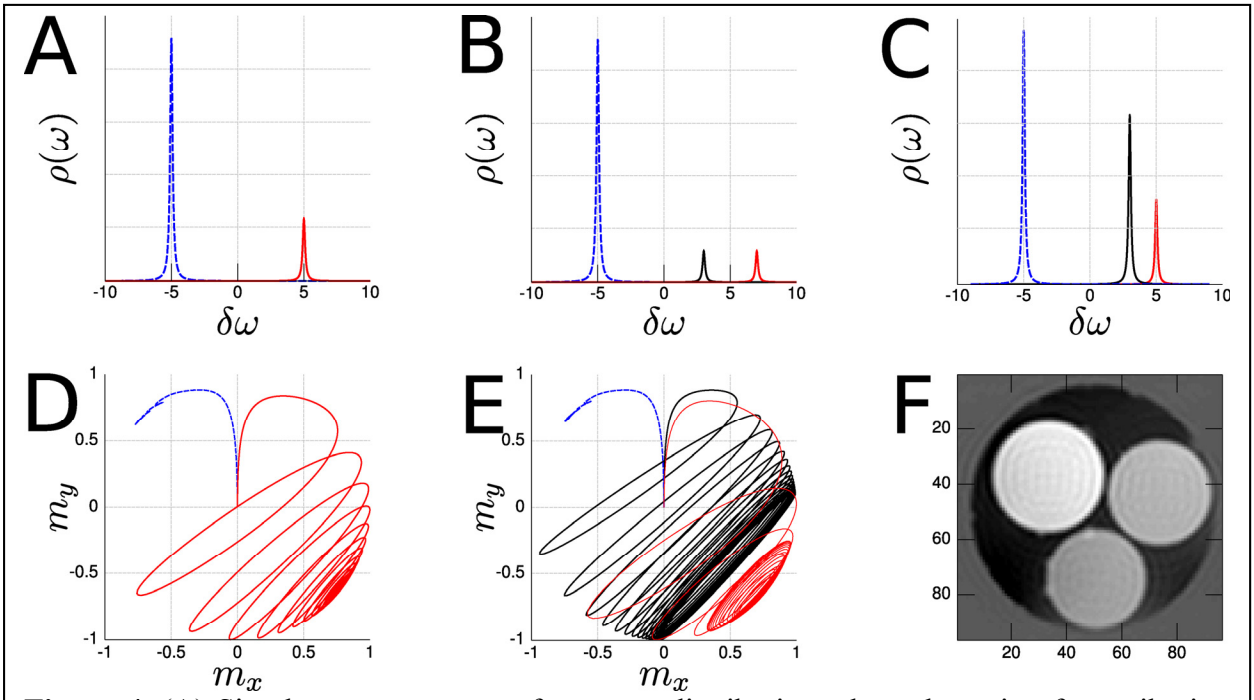

Figure 4. (A) Simple two-component frequency distribution where the ratio of contribution to Eq. 2 is 4:1, and $\Delta\omega_{ij} = 10\,\text{Hz}$. (B) Simple three-component frequency distribution where the ratio of contribution to Eq. 2 is 8:1:1. The minor component in part A was split in two such that the average of the two components is still the same as the minor component in part A. The difference between the bulk component and the average of the two minor components is thus 10 Hz as in part A. (C) Estimated frequency distribution of for a simple phantom containing pure water outside of the capillaries containing two different concentrations of acetone, which can shift the water resonance by a few Hz, depending on the concentration. (D) Transverse projection of the 3-dimensional trajectory for the system defined in part A. The dashed line corresponds to the bulk (dashed) peak, whereas the minor component corresponds to the minor (solid) peak. The relevant parameters are $\omega_1 = 50\,\text{Hz}$ and $\tau_r = 3\,\text{ms}$. (E) Transverse projection of the 3-dimensional trajectory for the system defined in part B. The dashed line corresponds to the bulk (dashed) peak, whereas the darker/black trajectory corresponds to the darker/black peak, and the lighter/red trajectory corresponds to the lighter/red peak. The relevant parameters are $\omega_1 = 50\,\text{Hz}$ and $\tau_r = 3\,\text{ms}$. (F) Experimental image of the simple phantom described in part C. The strength of the CW was estimated to be $\omega_1 \approx 45\,\text{Hz}$, and the strength of the radiation damping time constant was estimated to be $\tau_r \approx 3-4\,\text{ms}$.

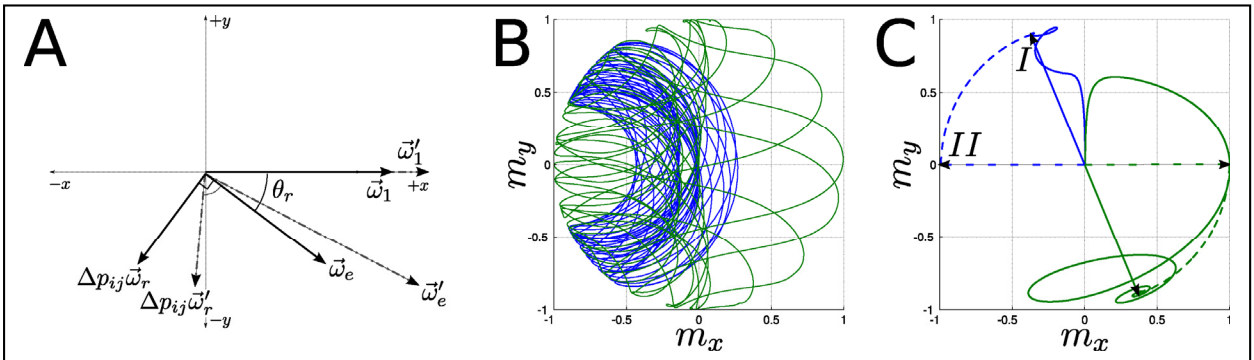

Figure 5. (A) 2-dimensional plot showing how θ_r changes upon relaxing the condition that $\varphi = 0$ as well as increasing ω_1, consistent with Eq. 9. It can be seen that in the limit that $\varphi \to \pi/2$ or $\omega_1 \to \infty$, then $\theta_r \to 0$. (B) Transverse projection of the 3-dimensional evolution for an uneven two-component system with $\varphi = \pi/2$, starting from equilibrium, with $\omega_1 = 50$ Hz, and $\tau_r = 2$ ms. Equation 9 predicts a shift of the $\psi_{\Delta p}$ state back towards the ψ_0 state. However, setting $\varphi = \pi/2$ disables the uneven Rabi cycle, removing the systems ability to stabilize at the fixed points, even though the fixed points are theorized to exist. (C) Transverse projection of the two-step 3-dimensional evolution for the same system in part B. The first step (I) is a simple application of a CW in the presence of radiation damping, bringing the system down to $\psi_{\Delta p}$. The second step (II) involves a gradual increase of ω_1 as well as slowly bringing $\varphi \to \pi/2$ such that the $\psi_{\Delta p}$ state can be rotated back towards the ψ_0 state, which demonstrates the theoretical ability to dynamically control the location of the fixed points in real time.

5.4.2 Self nutation

Up to this point, all of the fixed-points were located primarily in the transverse plane since the application of a CW prevents the system from stabilizing along the z-axis. Without a CW, following an arbitrary non-selective pulse, the natural radiation damping will always bring the two components back towards the equilibrium position in order to bring $\int \vec{m}_+(\vec{r})d^3\vec{r}$ to a minimum. Since the natural radiation damping is automatically activated for any $\int \vec{m}_+(\vec{r})d^3\vec{r} \neq 0$, it will immediately respond to influence the evolution of the magnetization, thus always bringing both components back to the $+z$ position. Replacing the natural radiation damping with the active feedback device, the feedback signal can be selectively turned on or off during any point in the evolution. Previously, the tendency of the natural radiation damping to bring the magnetization back towards the $+z$ position could be understood from a conservation of energy stand point. The use of an electronic feedback circuit, which does not require energy from the system in order to operate, bypasses this necessity, and so by altering the phase, the magnetization can be made to rotate any desired direction. By strategically controlling when the feedback is turned on, along with the phase of the applied feedback signal, the system can be made to shift towards fixed points along the $\pm z$ axes in an effect that this group refers to as self-nutation.

Consider the two-step pulse sequence as shown in Fig. 6A, where, following a preparatory 90° pulse, the magnetization is allowed to freely evolve for a time time of τ_1, to which the feedback is then switched via active feedback with a variable feedback phase, φ, and allowed to evolve for some time τ_2. The evolution of a two-component system (with $\Delta\omega_{ij} = 10$ Hz) can be broken down for each step, as shown schematically in Fig. 6B. Immediately

following the 90° pulse, the two components are allowed to precess away from each other, acquiring a phase in between them. The feedback signal can then be strategically placed directly in between both components, such that the trajectory for one component heads upwards towards the $+z$ direction, while the other component is forced downwards towards the $-z$ orientation. This step differs from typical natural radiation damping experiments where the radiation damping is either on the whole time, or not on at all. Using the active feedback device enables the specific control of when and where the feedback signal should be applied. As a result, both components are kicked off the transverse plane in opposite directions while rotating until they stabilize on opposite poles along the z-axis, seen in the last panel of Fig. 6B. The specific trajectories will vary depending on both τ_1 and φ, but as can be seen in Figs. 6C and 6D, the efficiency of reaching the fixed points is sensitive to the specific phase angle of the applied feedback signal. Nevertheless, it can be seen that strategically placing the feedback signal between the two components allows for the stabilization of both components along the $\pm z$ axis, contrary to the location of the previously discussed fixed points which were in the transverse plane, which were not allowed to return to the $\pm z$ axis because of the constant excitation of the CW. The active mechanism is very similar to the trivial behavior of a single component in the presence of radiation damping. In this case, the absence of the CW allows for the components to stabilize at the $\pm z$ positions where $\int \vec{m}_+(\vec{r}) d^3\vec{r}$ is minimized. The difference being in that having dynamic control over the timing, τ_1, as well as the phase, φ of the feedback can allow the system to bring the bulk back towards the equilibrium $+z$ position as usual, but bringing the minor component to the complete opposite pole along the $-z$ axis.

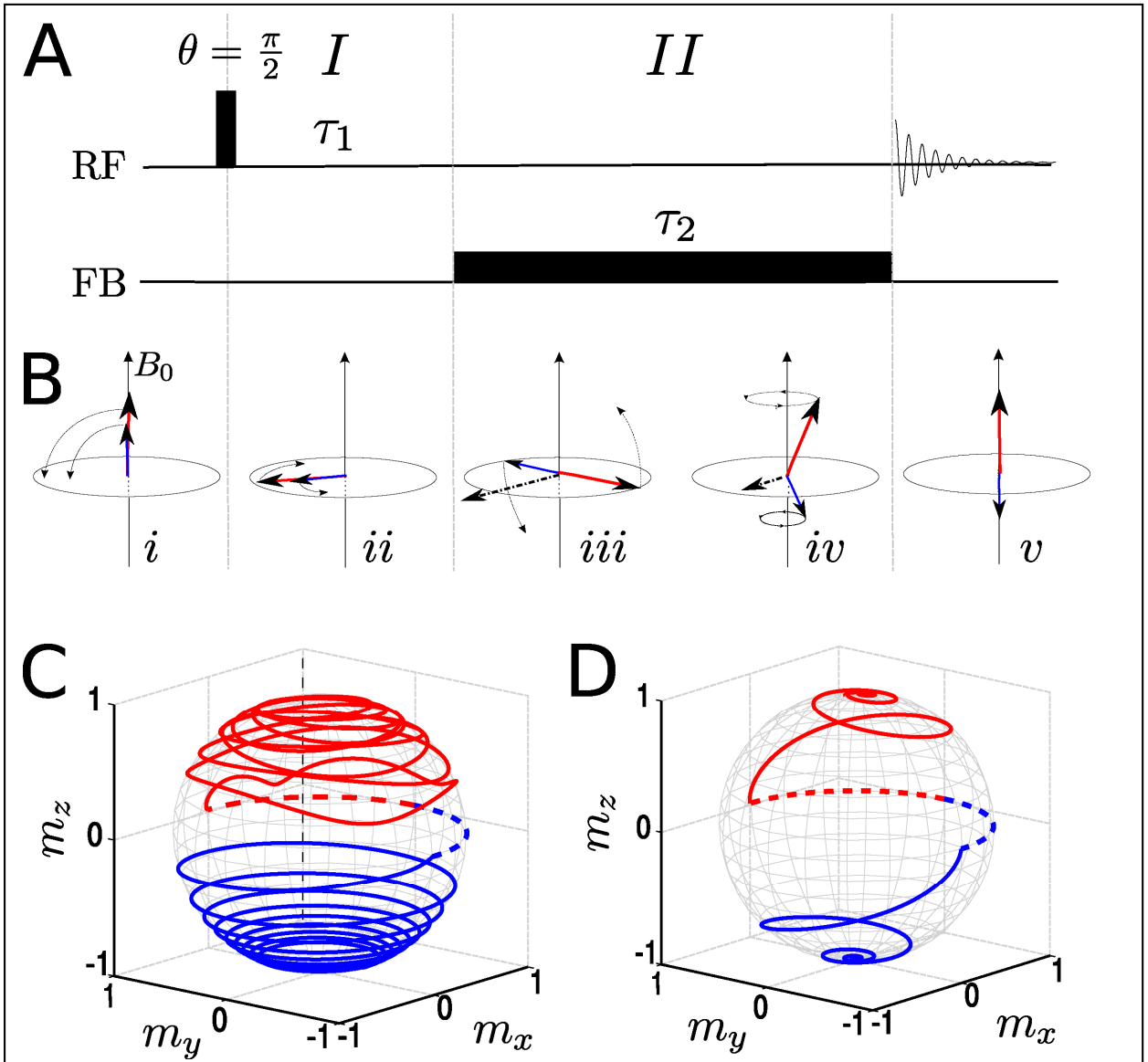

Figure 6. (A) The pulse sequence for a self-nutation experiment. The first step (I) involves a hard 90° pulse followed by a free evolution time of τ_1. The second step (II) involves evolution under the active feedback signal for a time of τ_2, with a feedback phase of φ (Eq. 2). (B) A general schematic demonstrating the dynamics of the pulse sequence shown in part A, for a simple two-spin system. Immediately after the 90° pulse (i), the two spins, with different resonance offset are allowed to precess away from each other during τ_1 (ii). The feedback signal is then turned on (dotted-dashed line) with a specific φ such that the feedback is applied directly between both components (iii), causing the spins to nutate in opposite directions towards opposite poles (iv) until they reach their fixed points along the $\pm z$ axis (v). Numerical simulations for a two component system with $\Delta\omega_{ij} = 10Hz$ demonstrating the dynamics in parts A and B, where (C) $\varphi = 91^\circ$, and (D) $\varphi = 100^\circ$. The dashed lines represent the free evolution (I) and the solid lines represent the evolution under the feedback signal (II).

5.5 Conclusion

The responsive nature of the radiation damping and feedback fields to the total transverse magnetization will force the system to evolve in order to minimize the total transverse magnetization $\int \vec{m}_+(\vec{r})d^3\vec{r}$. This is traditionally done by bringing the magnetization back towards the equilibrium $+z$ position, where $\int \vec{m}_+(\vec{r})d^3\vec{r} = 0$, making it a trivial fixed point. We have shown that the application of a CW prevents the magnetization from returning to the equilibrium $+z$ position, forcing the system to seek out an alternative orientation in which to minimize $\int \vec{m}_+(\vec{r})d^3\vec{r}$. For two-component cases, the most stable configuration is to place both components on opposite poles of the Bloch sphere such that the components can cancel each other out.

The presence of these fixed points on opposite sides of the Bloch sphere can be useful for imaging contrast, where the resonance offset difference between two regions is very small. While these types of fixed points are unlikely to be observed directly in experiment, it can be known that the magnetization is heading towards them, as they cannot stabilize along the equilibrium $+z$ orientation. As a result, the magnetization can thus be imaged *en route* to the fixed points without having to actually reach them in order to generate imaging contrast. With the aid of an active feedback circuit (in order to amplify the radiation damping signal), the use of a CW has been shown to be sensitive to the small differences between healthy and tumor tissues in mouse specimens, much more efficiently than current conventional imaging techniques. The specific fixed points presented in this paper do not represent an exhaustive list of the possible types of attainable fixed points. The goal of this paper is to illustrate that the tendency of the radiation damping to respond to the magnetization is key into the development of stable fixed points for multiple component system, often times on opposite sides of the Bloch sphere. The

determination and consequent characterization of additional types of fixed-points thus warrants additional investigation.

5.6 References

[1] D. Abergel, *Phys. Lett. A.* **302**, 17 (2002).

[2] F. Bloch, *Phys. Rev.* **70**, 460 (1946).

[3] N. Bloembergen, R. V. Pound, *Phys. Rev.* **95**, 8 (1954).

[4] P. Broekaert, J. Jeener, *J. Magn. Reson. A.* **113**, 60 (1995).

[5] S. Datta, S. Y. Huang, Y.-Y. Lin, *J. Phys. Chem. B.* **110**, 22071 (2006).

[6] J. K. Furuyama, *et al.*, *49th Experimental Nuclear Magnetic Resonance Conference* (2008).

[7] J. K. Furuyama, *et al.*, *Dynamic Fixed-Point Generation Using Non-Linear Feedback Fields - with Applications in MR Contrast Enhancement* (WILEY-VCH, 2008), chap. 5, pp. 65–79.

[8] D. I. Hoult, B. Bhakar, *Concepts Magn. Reson.* **9**, 277 (1997).

[9] S. Y. Huang, C. Anklin, J. D. Walls, Y.-Y. Lin, *J. Am. Chem. Soc.* **126**, 15936 (2004).

[10] S. Y. Huang, *et al.*, *Magn. Reson. Med.* **56**, 776 (2006).

[11] S. Y. Huang, J. K. Furuyama, Y.-Y. Lin, *Magn. Reson. Mater. Phy.* **19**, 333 (2006).

[12] J. Jeener, *J. Chem. Phys.* **116**, 8439 (2002).

[13] Y.-Y. Lin, N. Lisitza, S. Ahn, W. S. Warren, *Science* **290**, 118 (2000).

[14] A. Louis-Joseph, D. Abergel, J.-Y. Lallemand, *J. Biomol. NMR.* **5**, 212 (1995).

[15] X. an Mao, C.-H. Ye, *Concepts Magn. Reson.* **9**, 173 (1997).

[16] R. Tycko, A. Pines, J. Guckenheimer, *J. Chem. Phys* **83**, 2775 (1985).

[17] A. Vlassenbroek, J. Jeener, P. Broekaert, *J. Chem. Phys.* **103**, 5886 (1995).

[18] W. S. Warren, S. L. Hammes, J. L. Bates, *J. Chem. Phys.* **91**, 5895 (1989).

Chapter 6

Spin Control to Enhance NMR Sensitivity

6.0 Abstract

We demonstrate the first experimental control of transient spin chaos in high-field solution magnetic resonance. We characterize the high-dimensional spin turbulence arising from the joint action of radiation damping and the distant dipolar field by linear stability analysis and the leading Lyapunov exponents. Based on our analysis, a general approach is presented for suppressing and enhancing the dynamics at will by radiofrequency perturbations. We demonstrate applications of such control schemes to suppressing signal fluctuations and amplifying sensitivity by up to 30 times through indirect detection and spin amplification.

6.1 Introduction

The prevalence of complex, high-dimensional nonlinear dynamics in nature has generated great interest in their characterization and control [1, 2]. While examples of controlling low-dimensional nonlinear dynamics abound [3], experimental control over orbits with more than one unstable direction, including spatiotemporal chaos, proves more challenging [1]. A new type of high-dimensional nonlinear dynamics known as spin turbulence has recently emerged at high magnetic fields from the joint action of two reaction fields, radiation damping and the distant dipolar field (DDF) [4, 5, 6, 7, 11, 8, 9, 10, 14, 15, 16, 17]. The resulting nonlinear dynamics exhibit the essential features of transient chaos and may interfere in routine magnetic resonance (MR) experiments by generating signal distortions and irreproducible measurements

[6, 7, 11]. The ease of manipulating spin states by radiofrequency (RF) pulses provides an accessible and effective means of controlling the underlying spin chaos. This advantage, combined with the ability to separate spins from other degrees of freedom, makes MR experiments an ideal setting for experimentally testing various approaches in controlling high-dimensional unstable orbits. The ultimate goal is to suppress and enhance the inherent turbulent spin dynamics at will for experimental applications targeting the fundamental challenge of sensitivity enhancement in solution MR.

In this chapter, we characterize the discovered spin turbulence in the context of linear stability and the leading Lyapunov exponents. We present a general approach to control the dynamics by directing and maintaining trajectories toward more or less stable regions of state space. The difficulty of monitoring and controlling the full system state vector in high dimensions has been addressed by several groups through multiple perturbations of select control parameters [1, 2]. Here, we aim to control the high-dimensional turbulent spin system through RF perturbations to a single state variable, the average magnetization vector ε. Numerical simulations and experiments show that these control schemes can alternately suppress and enhance spin turbulence, marking the first experimental demonstration of controlling transient chaos due to the joint reaction fields in MR. In practice, our ability to manipulate the dynamics at will can be applied to suppress signal distortions and irreproducible measurements arising under the turbulent spin dynamics. The flexibility of our approach can also amplify sensitivity in MR spectroscopy by up to 30 times through indirect detection and spin amplification, as demonstrated here in simulations and experiments.

6.2 Theory and Method

Determining the stability of different spin configurations in state space requires an understanding of how dynamical instabilities due to radiation damping and the DDF arise in solutions with abundant high-gyromagnetic ratio (γ) spins. The nonlinear Bloch equations for the evolution of the magnetization $m(r,t)$ (normalized with respect to the equilibrium magnetization M_0) are

$$\frac{\partial m(r,t)}{\partial t} = \gamma m(r,t) \times \left[B_r(t) + B_d(r,t) \right]. \tag{1}$$

The radiation damping field $B_r(t)$ and distant dipolar field $B_d(r,t)$ can be described by [18, 19]

$$\gamma B_r(t) = \omega_r \int \mathrm{d}r \left[-m_y(r,t)\, x + m_x(r,t)\, y \right] \tag{2}$$

$$\gamma B_d(r,t) = \frac{\omega_d}{4\pi} \int \mathrm{d}r' \frac{3\cos^2 \theta_{rr'} - 1}{2\,|r - r'|^3} \times \left[3m_z(r',t)\, z - m(r',t) \right] \tag{3}$$

where $\omega_r = \gamma \mu_0 \eta M_0 Q/2$, $\omega_d = \gamma \mu_0 M_0$, η is the coil filling factor, Q is the probe quality factor, and μ_0 is the magnetic permeability of a vacuum. $B_r(t)$ acts back on the spins through the induced current in the receiver coil and causes the magnetization to nutate toward the asymptotically stable $+z$-axis at a rate proportional to the magnitude of the transverse magnetization [18]. $B_d(r,t)$ results from long-range dipolar couplings that survive spatial and temporal averaging in solution and is enhanced by application of gradients [19, 20, 21, 22]. $B_d(r,t)$ can produce dynamical instabilities in highly polarized samples [22, 23]; however, in typical solution MR experiments, dipolar instabilities can be largely neglected as they do not grow quickly enough to overcome T_2 relaxation [23].

Through radiation damping, however, bulk sample magnetization indirectly induces an additional RF irradiation field that hastens the onset of spin turbulence mediated by the DDF [4, 5]. A common component of many modern MR pulse sequences, the pulse-gradient combination $[\pi/2-(GT)_z]$ modulates the magnetization to establish a helix configuration whose net magnetization should average to zero. In practice, a small net magnetization ε survives the dephasing gradient and builds up over time [4] to contribute significantly to the instability by coupling directly to radiation damping and indirectly to the DDF [7, 11]. Linear stability analysis indicates that dynamics are unstable near the fixed point represented by helical distribution of magnetization under joint reaction fields [5].

In fact, the presence of net residual magnetization causes radiation damping to dominate initially, as the typical time scale for radiation damping τ_r is typically ~ 10 ms, while that for the DDF is much longer (~ 70 ms). The initial instability is thus governed by the instability of the net magnetization under radiation damping. Inverted magnetization represents an unstable equilibrium under radiation damping, which is reflected in the equation of motion under radiation damping, parameterized by r and θ. Net magnetization oriented in the lower half of the Bloch sphere is less stable than net magnetization oriented in the upper hemisphere for short times. When the net magnetization points along the $+z$-axis, the DDF also contributes to the instability but to a lesser extent. The stability of spin configurations evolving after $[(\pi/2)_x-(GT)_z]$ for short times can thus be roughly considered in the context of the stability of ε along the Bloch sphere. Results from extensive numerical simulations and analytical theory also support this conclusion.

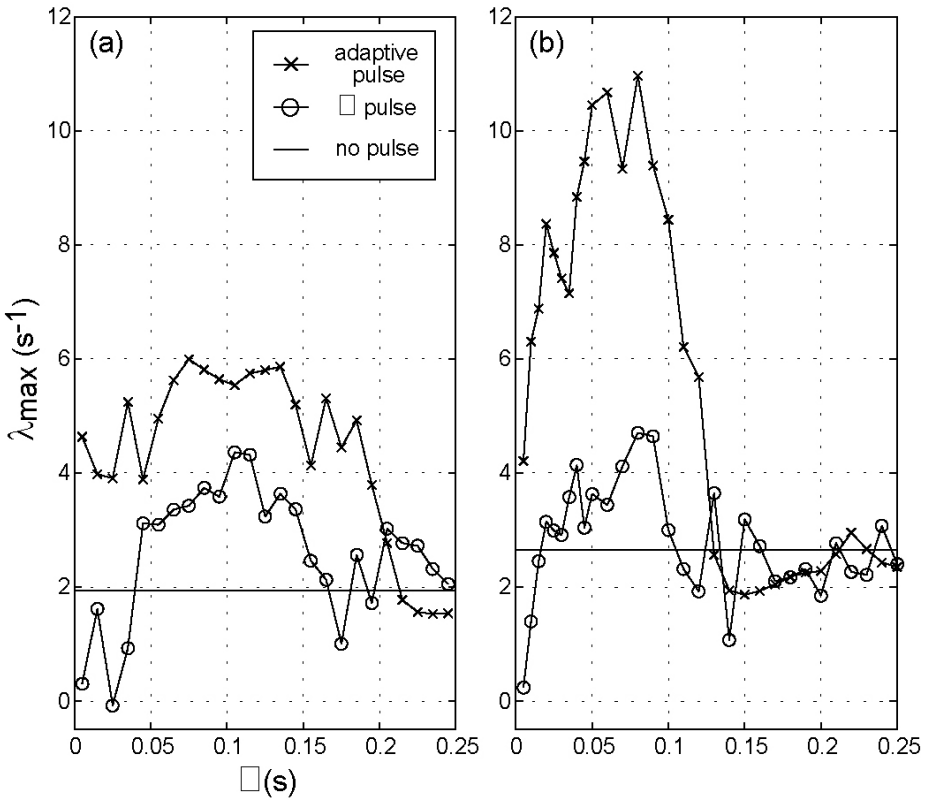

Figure 1. Largest Lyapunov exponent λ_{max} averaged over 2 s for the sequence $[(\pi/2)_x - (GT)_z - (\tau - RF - \tau)_n]$, where RF is either an adaptive pulse that brings the net magnetization to $-z$ (×) or a π_y pulse (○). For comparison, the solid lines show λ_{max} for free evolution following $[(\pi/2)_x - (GT)_z]$. (a) λ_{max} at ^{1}H resonance frequency 600 MHz (14.1 T), with $\omega_r = 125$ s^{-1} and $\omega_d = 14$ s^{-1}. (b) λ_{max} at 900 MHz (21.1 T), with $\omega_r = 189$ s^{-1} and $\omega_d = 22$ s^{-1}. Calculations were carried out on a rectangular lattice of sides $0.117 \times 0.117 \times 3.76$ mm^3, sampled by $8 \times 8 \times 256$ magnetization voxels along the x-, y-, and z-directions. Dynamics were found by numerically integrating the nonlinear Bloch equations based on the Runge-Kutta (4,5) algorithm and finite element method. Parameters used in the calculations were: $T_1 = 3.05$ s, $T_2 = 2.10$ s, $GT = 5$ gauss · ms/cm, and $\varepsilon_x = 5 \times 10^{-3}$.

6.3 Result and Discussion

The physical picture drawn above suggests that the dynamics under radiation damping and the DDF may be stabilized or destabilized by rotating and maintaining the net magnetization near the stable $+z$ or unstable $-z$ directions. The response of the spin system under such tailored manipulation can be assessed through the Lyapunov exponents, which measure the stability averaged over an entire trajectory. In particular, the largest Lyapunov exponent λ_{max} traces the growth of small perturbations along the direction of maximum expansion in phase space. Figure 1 shows λ_{max} estimated over an experimentally meaningful time scale of 2 s for RF control schemes designed to suppress and enhance the development of spin turbulence following the sequence $[(\pi/2)_x - (GT)_z]$.

The instabilities that arise under the nonlinear Bloch equations can be enhanced by applying feedback-based, adaptive RF pulses, whose flip angles and phases are adjusted to rotate ε toward the unstable $-z$ direction at fixed intervals τ (Fig. 1, crosses). As ε evolves back to the $+z$-axis under the joint reaction fields, adaptive RF pulses are required to maintain the magnetization in the inverted state. λ_{max} peaks for values of τ that allow the system to find the new direction of maximum expansion in phase space after each RF perturbation and optimize the magnitude of the longitudinal magnetization and the amount of time the net magnetization remains in the lower half of the Bloch sphere. However, if the delay between pulses 2τ is prolonged to allow ε to return to the $+z$-axis, λ_{max} averages to a smaller positive value as ε samples more configurations near the stable $+z$-axis. Furthermore, λ_{max} takes on larger values at 900 MHz due to stronger radiation damping and DDF effects at higher fields.

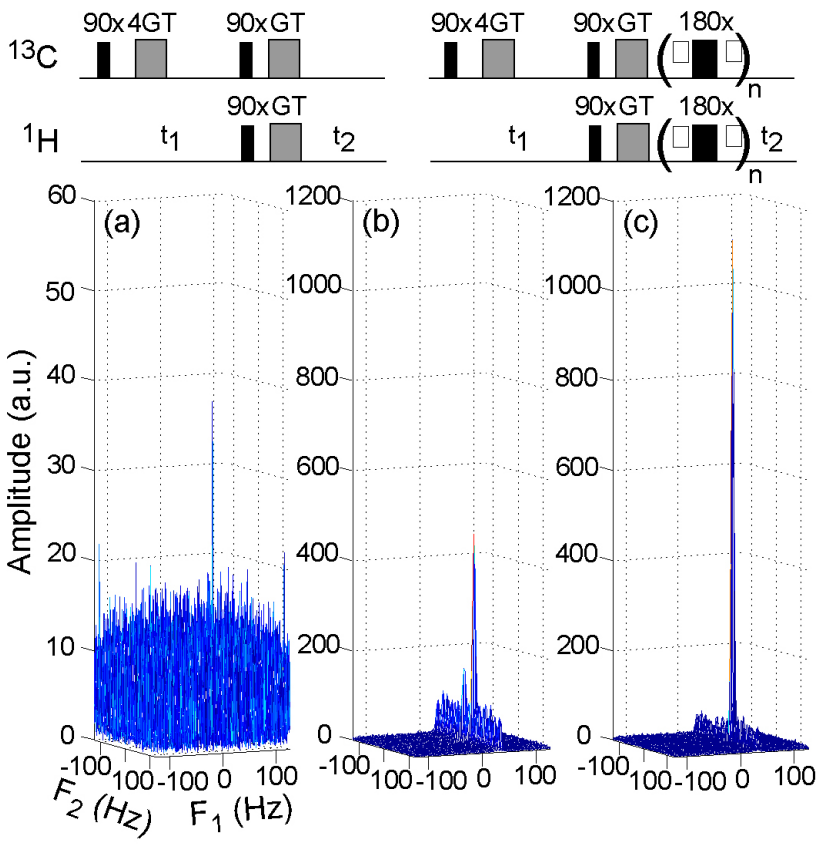

Figure 2. Simulated two-dimensional frequency spectra according to the indirect detection sequences shown above, with (right, (c)) and without (left, (a) and (b)) control of spin turbulence, for an aqueous solution of 1 M ^{13}C. The carbon magnetization (resonance offset +30 Hz) is about 10^{-5} of the water magnetization (resonance offset -20 Hz). The sample was modeled by 256 magnetization voxels in the z direction while assuming uniform transverse magnetization. Thermal noise in the electronics was simulated by adding Gaussian noise with standard deviation 0.0275 to each point in the two-dimensional data set prior to Fourier transform. Parameters used in the calculations were: $t_1 = 1.024$ s, ω_d (^{1}H)=14 s^{-1}, ω_d (^{13}C) $= 2.1\times10^{-3}$ s^{-1}, ω_r (^{1}H)=125 s^{-1}, T_2 (^{1}H)=2.10 s, T_2 (^{13}C)=5 s, GT =5 gauss $\cdot$ ms/cm, $\sigma = 1.5\times10^{-4}$, and $\sigma_\varepsilon = 1.5\times10^{-4}$. (a) DDF only, with $t_2 = 800$ ms. (b) DDF and radiation damping, with $t_2 = 468$ ms. (c) DDF, radiation damping, and control, with $\tau = 5$ ms, $n = 20$, and $t_2 = 532$ ms.

Adaptive feedback-controlled perturbations require precise knowledge of the state of the magnetization as it evolves. Modern electronic and computational techniques should be able to acquire information about the precessing magnetization and evaluate appropriate RF correction fields quickly enough to implement effective feedback pulses. Still, present spectrometer hardware and software do not allow direct access to the real-time magnetization trajectory, which thus raises the need for alternative control approaches. Replacing the adaptive control scheme simulated in Fig. 1 (crosses) with periodic π pulses (Fig. 1, circles) results in similar trends for λ_{max}. λ_{max} for periodic control is smaller, however, as the ability to force ε into the lower half of the Bloch sphere is more limited in the periodic scheme than for feedback control. For sufficiently large τ, λ_{max} for both control schemes converge to the same value since the adaptive pulses essentially become π pulses if the net magnetization is allowed to evolve back to the $+z$ -axis.

In the short τ regime, the rapid pulsing prevents the system from fully recovering its new maximum expansion direction, and the dynamics subjected to periodic control may be better understood through an approach inspired by average Hamiltonian theory [24]. In the interaction frame of the periodic π pulse sequence $[\tau-\pi-2\tau-\pi-\tau]$, the nonlinear Bloch equations are $\partial\tilde{m}/\partial t=\gamma[\tilde{m}\times\tilde{B}_d+g(t)\tilde{m}\times\tilde{B}_r]$, where $g(t)=1$ when $0<t<\tau, 3\tau<t<4\tau$ and -1 when $\tau<t<3\tau$ and $\tilde{m}$, $\tilde{B}_d$, and $\tilde{B}_r$ are written in the interaction frame. When repeated in rapid succession, this sequence averages out in time the dominant reaction field ($\langle g(t)\tilde{m}\times\tilde{B}_r\rangle\approx 0$) while leaving the DDF intact. The instability then reduces to that of the DDF alone, which is negligible in solution [5]. Further pulse sequence optimization can be achieved by expressing

$\widetilde{B}_d$ and $\widetilde{B}_r$ in terms of $\widetilde{m}$, then carrying out a perturbation analysis similar to that used in average Hamiltonian theory.

Periodic π pulses can be directly applied to suppress spin turbulence in such experiments as correlation spectroscopy, diffusion measurements, and imaging, for which the underlying Hamiltonians, e.g., scalar couplings and interactions depending only on spatial variables, are invariant under RF rotations. The periodic control of spin turbulence may also be exploited to tackle the age-old problem of low sensitivity in MR, with potent applications in biomolecular NMR where insensitive and/or dilute spins are detected. For example, indirect detection of low-γ nuclei such as ^{13}C with the large ^{1}H magnetization can potentially improve the signal-to-noise ratio (SNR) of rare, insensitive spins [26, 27]. This method does not require the two spin species to be chemically coupled or located on the same molecule; instead, they interact through the nonlinear DDF. The indirect detection sequence is shown in Fig. 2 (top right). This sequence allows the ^{1}H spins to precess during t_2 under the influence of the DDF produced by ^{13}C spins in t_1. The resulting echo carries information about the state of the ^{13}C magnetization and therefore furnishes a means of indirectly detecting the rare species. In certain cases, indirect detection by the DDF can yield a higher SNR than that obtained by direct detection [26]. In practice, however, achieving signal gains by indirect detection is difficult as growth of the indirect echo signal under the DDF is constrained by relaxation [26, 27]; consequently, the indirectly detected signal is usually overshadowed by thermal noise in the electronics (Fig. 2(a)).

The small ^{1}H signals arising from indirect detection can, however, be amplified by triggering the self-refocusing of the water magnetization helix under the joint action of radiation damping and the DDF [4]. A significant drawback of the signal amplification process is that, if left unchecked, the chaotic spin dynamics indiscriminately amplify both the desired signal as

well as small variations affecting the inherent spin dynamics, e.g., spin noise and spectrometer instability [7], which subtracts from the expected improvement in SNR (Fig. 2(b)). To offset the unwanted amplification of intrinsic noise due to such variations, rapid modulation of the magnetization by π pulses during the initial growth of the ^{1}H indirect echo is applied to delay the amplification process while leaving the DDF intact. While the periodic RF control sequence is applied (Fig. 2, top left), heteronuclear polarization transfer takes place solely under the DDF, without the interference of radiation damping and the accompanying spin chaos. Once the indirectly detected signal has grown to a sufficient height to overcome the intrinsic noise level, the desired indirectly detected ^{1}H signal is then amplified through evolution under the joint reaction fields. Minimizing the interference of intrinsic noise on the spin dynamics results in an increase in SNR by up to 30 times (Fig. 2(c)) over detection by the DDF alone (Fig. 2(a)). This example suggests potential applications of such control schemes to sensitivity and contrast enhancement. A detailed discussion of this method and experimental results will be reported elsewhere.

6.4 Conclusion

In conclusion, knowledge of stable and unstable spin configurations under radiation damping and the DDF has been used to guide the design of adaptive or periodic control sequences that selectively suppress or enhance the feedback leading to spin turbulence. We apply such control schemes to suppress MR signal fluctuations and construct a powerful, controlled signal amplification scheme for NMR sensitivity enhancement by indirect detection and spin amplification. Our approach marks the first experimental demonstration of controlling transient spin chaos due to the joint reaction fields in high-field MR. The transient chaos that develops in

spin systems also provides a context in which theories on chaos control in high-dimensional dynamical systems may be further investigated. Higher fields and more sensitive probes will intensify the underlying reaction fields, making the characterization and control of the turbulent spin dynamics all the more important for understanding and designing experiments at high fields.

6.5 Reference

[1] D. Auerbach *et al.*, Phys. Rev. Lett. **69**, 3479 (1992).

[2] P. So and E. Ott, Phys. Rev. E **51**, 2955 (1995); V. Petrov *et al.*, Phys. Rev. E **51**, 3988 (1995); M. Löcher and E. R. Hunt, Phys. Rev. Lett. **79**, 63 (1997).

[3] E. Ott and M. L. Spano, Phys. Today **48**, No. 5, 34 (1995).

[4] Y.-Y. Lin *et al.*, Science **290**, 118 (2000).

[5] J. Jeener, J. Chem. Phys. **116**, 8439 (2002).

[6] S. Y. Huang, Y.-Y. Lin, N. Lisitza, and W. S. Warren, J. Chem. Phys. **116**, 10325 (2002).

[7] S. Y. Huang, J. D. Walls, Y. Wang, W. S. Warren, and Y.-Y. Lin, J. Chem. Phys. **121**, 6105 (2004).

[8] S. Datta, S. Y. Huang, Y.-Y. Lin, J. Chem. Phys. **124**, 154501 (2006).

[9] S. Datta, S. Y. Huang, Y.-Y. Lin, Concepts Magn. Reson. A **28**, 410 (2006).

[10] S. Datta, S. Y. Huang, Y.-Y. Lin, J. Phys. Chem. B **110**, 22071 (2006).

[11] S. Y. Huang, C. Anklin, J. D. Walls, Y.-Y. Lin, J. Am. Chem. Soc. **126**, 15936 (2004).

[12] J. D. Walls, S. Y. Huang, Y.-Y. Lin, J. Phys. Chem. B **110**, 19985 (2006).

[13] J. D. Walls, S. Y. Huang, Y.-Y. Lin, J. Chem. Phys. **127**, 054507 (2007).

[14] S. Y. Huang, S. M. Wolahan, G. W. Mathern, D. J. Chute, M. Akhtari, S. T. Nguyen, M. N. Huynh, N. Salamon, Y.-Y. Lin, Magn. Reson. Med. **56**, 776 (2006).

[15] S. Y. Huang, J. K. Furuyama, Y.-Y. Lin, MAGMA (Magnetic Resonance Materials in Physics, Medicine, and Biology) 24, 135 (2006).

[16] S. Y. Huang, A. P. Chung, Y.-Y. Lin, Concepts Magn. Reson. A **30**, 378 (2008).

[17] S. Y. Huang, S. S. Yang, Y.-Y. Lin, Magn. Reson. Med. **61**, 925 (2009).

[18] M. P. Augustine, Prog. NMR Spectrosc. **40**, 111 (2002).

[19] G. Deville, M. Bernier, and J. M. Delrieux, Phys. Rev. B **19**, 5666 (1979).

[20] R. Bowtell, R. M. Bowley, and P. Glover, J. Magn. Reson. **88**, 643 (1990).

[21] W. S. Warren *et al.*, Science **262**, 2005 (1993).

[22] M. V. Romalis and M. P. Ledbetter, Phys. Rev. Lett. **87**, 067601 (2001); M. P. Ledbetter and M. V. Romalis, Phys. Rev. Lett. **89**, 287601 (2002).

[23] J. Jeener, Phys. Rev. Lett. **82**, 1772 (1999).

[24] U. Haeberlen and J. S. Waugh, Phys. Rev. **175**, 453 (1968).

[25] Y.-Y. Lin *et al.*, Phys. Rev. Lett. **85**, 3732 (2000).

[26] R. Bowtell, J. Magn. Reson. **100**, 1 (1992);

[27] W. S. Warren and S. Ahn, J. Chem. Phys. **108**, 1313 (1998).

Chapter 7

Spin Control to Alleviate Strong, Irregular Self-Induced Dynamic Frequency Shifts

7.0 Abstract

Accurate temperature measurement is a requisite for obtaining reliable thermodynamic and kinetic information in all NMR experiments. A widely used method to calibrate sample temperature depends on a secondary standard with temperature-dependent chemical shifts to report the true sample temperature, such as the hydroxyl proton in neat methanol or neat ethylene glycol. The temperature-dependent chemical shift of the hydroxyl protons arises from the sensitivity of the hydrogen-bond network to small changes in temperature. The frequency separation between the alkyl and the hydroxyl protons are then converted to sample temperature. Temperature measurements by this method, however, have been reported to be inconsistent and incorrect in modern NMR, particularly for spectrometers equipped with cryogenically-cooled probes. Such errors make it difficult or even impossible to study chemical exchange and molecular dynamics or to compare data acquired on different instruments, as is frequently done in biomolecular NMR. In this work, we identify the physical origins for such errors to be unequal amount of dynamical frequency shifts on the alkyl and the hydroxyl protons induced by strong radiation damping (RD) feedback fields. Common methods used to circumvent RD may not suppress such errors. A simple, easy-to-implement solution was demonstrated that neutralizes the RD effect on the frequency separation by a "selective crushing recovery" pulse sequence to

equalize the transverse magnetization of both spin species. Experiments using cryoprobes at 500 MHz and 800 MHz demonstrated that this approach can effectively reduce the errors in temperature measurements from about ±4.0 K to within ±0.4 K in general.

7.1 Introduction

High-resolution, high-field solution NMR is a valuable analytical tool for studying molecular structure and dynamics with great accuracy and reliability. In NMR studies, reliable, accurate, and consistent temperature measurements are crucial, especially when studying protein structure and dynamics. Researchers wishing to perform temperature dependent experiments have reported errors and inconsistency when calibrating the temperature in probes with a high quality factor (Q) operating at high fields [1]. Such errors become even more pronounced for spectrometers equipped with cryogenically-cooled probes – a popular trend for hardware development in modern NMR.

In this work, we first reveal the underlying spin dynamics that leads to significant temperature calibration errors, i.e. nonlinearity and its resulting dynamical frequency shifts triggered by the radiation damping feedback fields. Then, a new approach that effectively alleviates such errors by controlling the inherent interaction between the sample and the receiver coil to report the true sample temperature in high Q probes is demonstrated.

Accurate temperature measurement is an important requisite for obtaining reliable thermodynamic and kinetic information of the spin systems in all NMR experiments [2-5]. This is especially true for biomolecular NMR where researchers use high-field NMR spectrometers and sensitive probes to obtain high resolution spectra and need accurate temperature measurements to study chemical exchange and molecular dynamics. For example, the exchange

process between the dominant NMR observable state of a protein and an NMR invisible low-populated excited state has been recognized as critical in the function of the protein and is commonly studied by relaxation dispersion NMR spectroscopy [6], which relies on comparing spectra acquired at several field strengths. The temperature must be the same on all NMR spectrometers to obtain comparable data and, by studying relaxation dispersion at different temperatures, the thermodynamic properties of the system are elucidated [7]. As another example, in a structure determination procedure, 20-30 multi-dimensional spectra are generally acquired where chemical shifts are compared to make assignments. Referencing is done to the water peak at the center of the spectrum. It is set a specific temperature dependent chemical shift. A few degree of temperature difference between instruments due to the temperature calibration errors would result in ~0.04-0.06 ppm offset between the data sets, which is unacceptable for accurate structure determination.

7.2 Theory and Method

The spectrometer controls sample temperature by blowing air past the NMR tube and coil and reports the air temperature in this area. The air-to-sample temperature relationship is calibrated by determining the true sample temperature at a range of spectrometer-controlled air temperatures. The most generally used method to measure the true temperature of the solution depends on a secondary standard with a temperature-dependent chemical shift covering a wide temperature range [2-5]. These criteria are met by the hydroxyl proton in methanol for temperatures between 180 and 330K, and in ethylene glycol for higher temperatures between 270 and 440K. The temperature-dependent chemical shift of hydroxyl protons arises from the sensitivity of the hydrogen-bond network to small changes in temperature. One then measures

the temperature-dependent frequency separation, Δυ, between the two peaks of methanol or ethylene glycol. Conversion formula are then used to convert Δυ to the true sample temperature [2-5].

Radiation damping (RD) causes spectra to have broad peaks shifted from their true frequency in sensitive probes [8-28]. RD is a macroscopic feedback field, which is fed back to the spins through the induced free-induction-decay (FID) current in the receiver coil. Define the dimensionless normalized Bloch vector as $\boldsymbol{m} \equiv \boldsymbol{M}/M_0$, where $\boldsymbol{M}$ is the sample's magnetization density vector and M_0 is the sample's equilibrium magnetization under the external Zeeman field of flux density B_0 along the z axis. As dictated by Lenz's law, the RD field exerts a torque to nutate $\boldsymbol{m}$ on the surface of the Bloch sphere and can be described by [8-28]

$$\mathbf{B_r}(t) = \frac{1}{\gamma\tau_r} i < m_+(t) > e^{-i\psi} \tag{1}$$

where τ_r is the RD time constant, ψ is the RD phase, and $m_+ = m_x + i\, m_y$ is the transverse magnetization $m_+ = m_x + i\, m_y$. The RD time constant is defined as $\tau_r = 2/(\mu_0 \eta M_0 Q \gamma)$, where η is the sample filling factor, γ is the gyromagnetic ratio, and μ_0 is the vacuum permeability. The RD field, $\mathbf{B_r}$, lags 90° behind the average transverse magnetization, $<m_+>$, when the RD phase $\psi = 0°$, but may vary depending on the probe conditions. For example, the tuning and matching conditions of the radio-frequency (RF) circuits, as well as the properties of the transmission lines connecting these to the preamplifier, have direct consequences for NMR probe sensitivity and for the optimum delivery of RF power to the sample, thereby influencing the strength, $1/\tau_r$, and phase, ψ, of the RD feedback fields [18]. Despite the considerable efforts invested in suppressing RD and its unwanted effects, most of the existing techniques require hardware modifications, or complicated pulse and data processing methods [8-28]. Most recently, novel spin-engineering approaches have been proposed and demonstrated to reduce RD, for example, by using pulse

sequences that create a small transverse magnetization and simultaneously eliminate z-magnetization [19].

The RD field leads to a dynamical frequency shift, ω(t), for each spin species in the sample [9,10,19]. Such frequency shifts, ω(t), are "dynamical" in the sense that they depend on the instantaneous, time-dependent field conditions. For a one-spin species system such as pure water, the dynamical frequency shift can be derived as [10]

$$\omega(t) = m_z(t)\frac{\sin\psi}{\tau_r} \quad . \tag{2}$$

In a multi-spin species system (i=1,2,…,n), each spin species experiences a different dynamical frequency shift, $\omega_i(t)$, that depends on its z-magnetization ($m_{z,i}$); the relative contribution to the sample's total averaged transverse magnetization, $\langle m_+ \rangle = \langle m_{+,1} \rangle + \ldots + \langle m_{+,n} \rangle$; the RD time constant, τ_r; and the resonance offset from the RD field frequency. Consequently, RD can change the frequency separation of the two ^{1}H peaks, Δυ, in pure methanol or pure ethylene glycol to generate erroneous temperature readings. This is demonstrated in Fig. 1 by Matlab computer simulation to numerically integrate the nonlinear, generalized Bloch equations for various initial RF flip angles and RD time constant τ_r. After stimulating the spin system with a RF pulse of 5°, 45°, or 90° to obtain the resulting FIDs, the chemical shifts were determined with the ITMPM method, a combined detection-estimation scheme, which determines frequencies with much greater accuracy than the Fourier transform by fitting the acquired FIDs with a set of damped complex exponentials by the matrix-pencil method [29]. All chemical shifts reported in this work were determined with the ITMPM method.

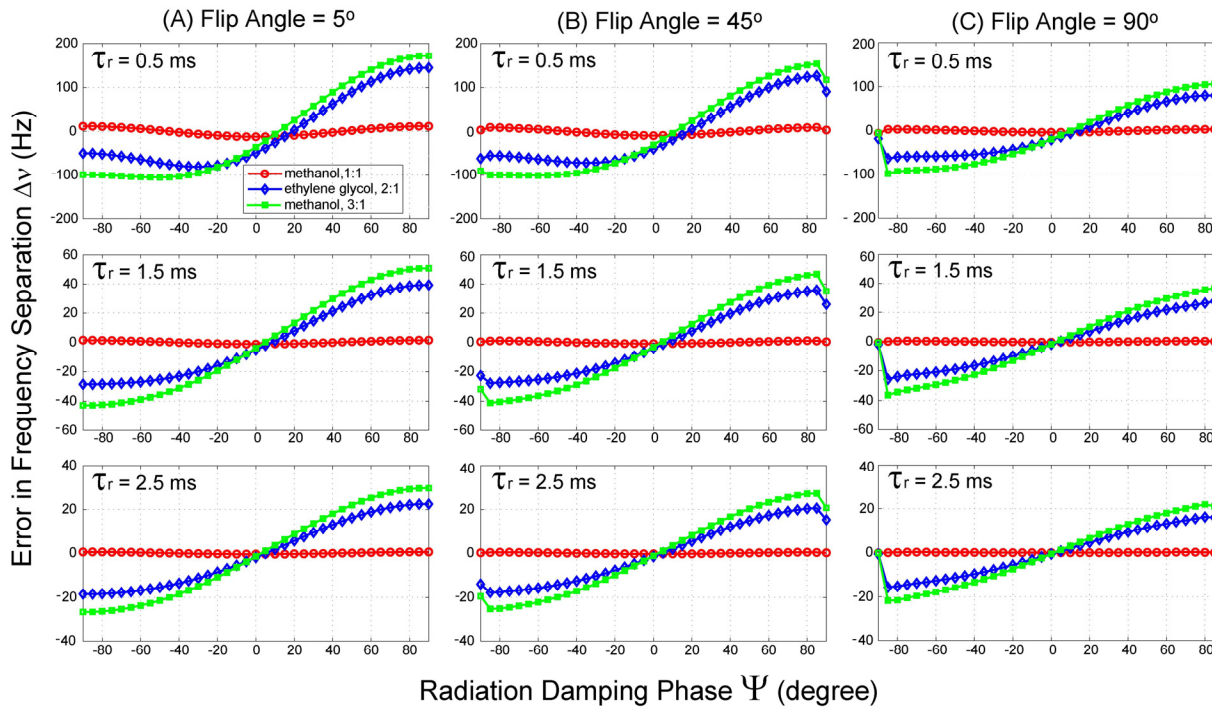

Figure 1. Simulation results of RD-induced errors in frequency separation, Δυ, as a function of the RD phase ψ. With the conventional pulse-acquire sequence and for the initial flip angle (a) 5˚, (b) 45˚, and (c) 90˚, three RD time constants are shown for two spin species in a 3:1 ratio in pure methanol (green square), in a 2:1 ratio in pure ethylene glycol (blue diamond), and in a 1:1 ratio in pure methanol with the "selective crushing recovery" pulse sequence illustrated in the inset of Fig. 2b (red circle). At 500 MHz and 287.4 K, the correct Δυ is 833.5 Hz for methanol and 878 Hz for ethylene glycol.

7.3 Result and Discussion

Simulations in Fig. 1 reveal that RD changes $\Delta\upsilon$ and, therefore, induces errors in temperature measurement in pure methanol (green squares) by as much as -25 ~ +30 Hz for typical high Q probes (τ_r = 2.5 ms) and by as much as -100 ~ +180 Hz for cryoprobes (τ_r = 0.5 ms) with small initial flip angles and large absolute RD phases $|\psi| \rightarrow 90°$. Moreover, common methods used to circumvent RD may not suppress such errors. For examples, detuning the probe deteriorates the signal-to-noise ratio and shifts the RD phase towards $|\psi| \rightarrow 90^{\circ}$. Small flip angles minimize the transverse magnetization and therefore $\mathbf{B_r}$ [Eq. (1)], but maximize the instantaneous RD-induced dynamical frequency shifts and the error in $\Delta\upsilon$ [Eq. (2) and Fig. 1]. Diluted or deuterated samples alleviate the RD effect, but, because the hydrogen bond network is weaker now, $\Delta\upsilon$ becomes less sensitive to temperature changes. The simulations of methanol and ethylene glycol in Fig. 1 (green squares and blue diamonds) and experimental results for methanol $\Delta\upsilon$ in Fig. 3 (blue asterisk) help explain why temperature errors are so prevalent in NMR experiments using cryoprobes where strong RD is present.

Simulations in Fig. 1 also reveal that accurate $\Delta\upsilon$ and, therefore, temperature measurements can actually be restored when the transverse magnetization of the two spin species are in a 1:1 ratio, rather than a 3:1 ratio as in methanol or a 2:1 ratio as in ethylene glycol. Under such experimental conditions, both spin species experience the same degree of dynamical frequency shifts, $\omega(t)$, which cancel out each other and leave $\Delta\upsilon$ intact. In order to equalize the transverse magnetization of the two spin species, a "selective crushing recovery" scheme was proposed, as shown in the inset of Fig. 2b. The selective 90° pulse on the larger of the two peaks, the alkyl proton, and the following z-gradient together crush the alkyl proton magnetization. Since the molar ratio of the alkyl proton to the hydroxyl proton in methanol is 3:1, the crushed

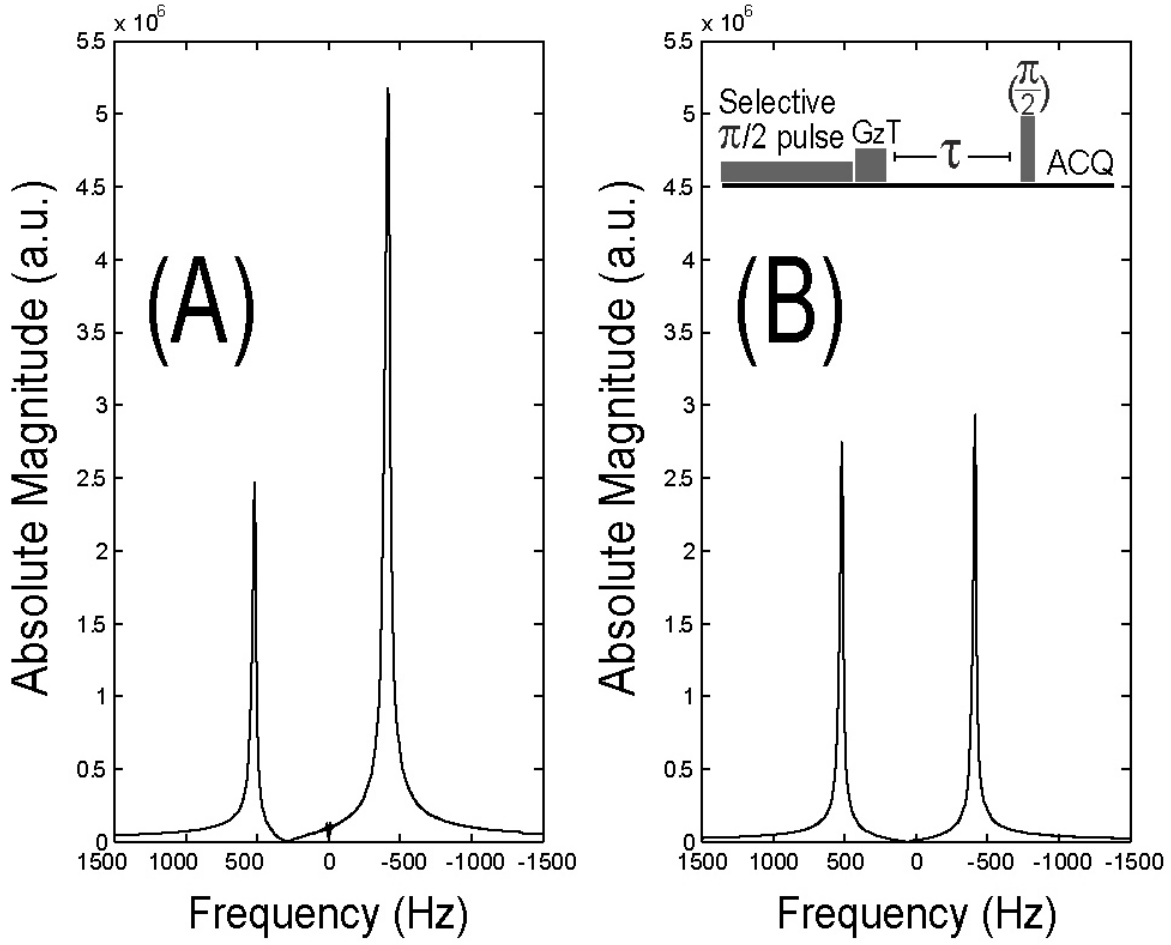

Figure 2. Fourier transform of the FID of a standard neat methanol sample acquired on a 600 MHz Bruker AVANCE spectrometer. (a) Data acquired after a hard 90° pulse. (b) Data acquired after the "selective crushing recovery" pulse sequence (insert) with the selective pulse centered on the CH_3 peak and $\tau = 3.5$ s.

magnetization of the alkyl proton can grow to the equilibrium magnetization of the intact hydroxyl proton when the delay period, τ, is chosen to be $0.405*T_{1,alkyl}$ of the alkyl proton of methanol in an inversion recovery process (Fig. 2b). Similarly, when τ is chosen to be $0.693*T_{1,alkyl}$ of the alkyl proton of ethylene glycol, the two spin species in ethylene glycol will have equal magnetizations. In practice, acquiring spectra for a range of τ until the integrated area of the two peaks are equal works best and knowing the exact T_1 value at a given temperature is

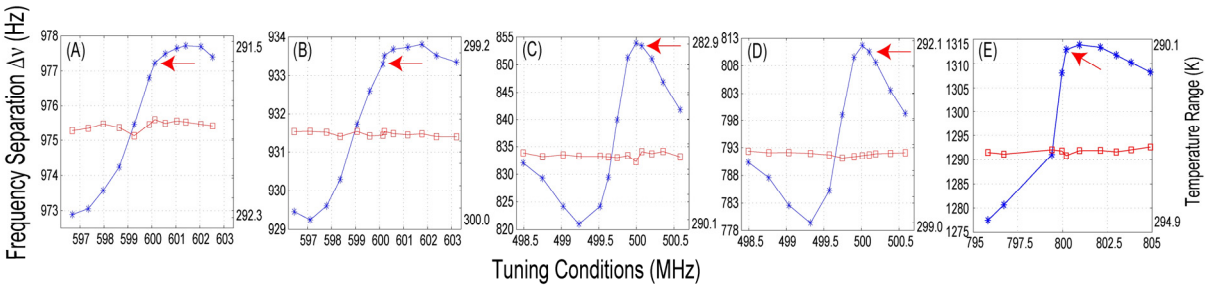

Figure 3. Chemical shift (left axis) and corresponding range of temperature reading (right axis) of methanol as a function of probe tuning. Arrow denotes the "best" tuning condition, achieved by the practice of minimizing the RF reflected power. Asterisks correspond to chemical shifts measured from spectra acquired after a hard 90° pulse and squares to chemical shifts measured from the selective crushing recovery pulse sequence (Fig. 2b inset). Data acquired on a 600 MHz Bruker AVANCE spectrometer with a microimaging probe (τ_r = 5 ms) at a spectrometer-determined temperature of (a) 290 K and (b) 300 K; on a 500 MHz Bruker spectrometer with a cryoprobe (τ_r = 1.5 ms) at a spectrometer-determined temperature of (c) 290 K and (d) 300 K; and on a 800 MHz Bruker AVIII spectrometer with a cryoprobe (τ_r = 1.3 ms) at a spectrometer-determined temperature of (e) 293 K.

unnecessary. Experimentally determined $\Delta\upsilon$ from spectra acquired with the "selective crushing recovery" pulse sequence at a range of tuning conditions are shown in Fig. 3 on a microimaging probe (τ_r = 5 ms) at 600 MHz (3a and 3b), a cryoprobe (τ_r = 1.5 ms) at 500 MHz (3c and 3d), and a cryoprobe (τ_r = 1.3 ms) at 800 MHz (3e). Under all experimental conditions, this approach reduces the errors in $\Delta\upsilon$ (and in temperature) from approximately ±2.5 Hz (±0.4 K) to ±0.2 Hz (±0.04 K) in the microimaging probe at 600 MHz, from ±20 Hz (±3.5 K) to ±2.1 Hz (±0.35 K) in the cryoprobe at 500 MHz, and from ±22 Hz (±3.9 K) to ±2.3 Hz (±0.39 K) in the cryoprobe at 800 MHz, providing satisfactory, consistent, and accurate measurements in $\Delta\upsilon$ and, therefore, sample's true temperature.

7.4 Conclusion

In summary, we have revealed the physical origins for the pronounced errors in measuring sample temperature using high-Q probes in solution NMR to be unequal amount of RD-induced dynamical frequency shifts, $\omega_i(t)$, to each spin species. A simple solution was proposed that neutralizes this RD effect on $\Delta\upsilon$ by the "selective crushing recovery" method to equalize the contribution of each spin species to the average transverse magnetization. Experiments using cryoprobes at 500 MHz and 800 MHz demonstrated that this approach can effectively reduce the errors in temperature measurements from ±3.9 K to within ±0.4 K in general. It should be pointed out that, in principle, RD-induced errors in $\Delta\upsilon$ and temperature measurements vanish when RD phase $\psi = 0^\circ$, as shown in Fig. 1. In practice, however, such experimental condition $\psi = 0^\circ$ is hard to achieve.[10,16,19] Ironically, the common practice of finding the perfect tuning condition to reach $\psi = 0^\circ$ by minimizing the reflected power almost guarantees the largest temperature measurement errors, about -3.9 K for cryoprobes (arrow in Fig. 3). With the trend of designing even more sensitive cryoprobes and ultra-high-field magnets, the errors in temperature measurements are expected to become more pronounced and the proposed solution more useful.

7.5 References

[1] G. Gemmecker, Technische Universität München, Department Chemie, Garching, Germany. Personal communication.

[2] C. Ammann, P. Meier, A.E. Merbach, A simple multi-nuclear NMR thermometer, J. Magn. Reson. 46 (1982) 319-321.

[3] M.L. Kaplan, F.A. Bovey, H.N. Cheng, Simplified method of calibrating thermometric nuclear magnetic-resonance standards, Anal. Chem. 47 (1975) 1703-1705.

[4] J.J. Led, S.B. Petersen, Heating effects in C-13 NMR-spectroscopy on aqueous-solutions caused by proton noise decoupling at high-frequencies, J. Magn. Reson. 32 (1978) 1-17.

[5] W.H. Sikorski, A.W. Sanders, H.J. Reich, Tris(trimethylsilyl)methane as an internal C-13 NMR chemical shift thermometer, J. Magn. Reson. Chem. 36 (1998) S118-S124.

[6] D.F. Hansen, P. Vallurupalli, L.E. Kay, Using relaxation dispersion NMR spectroscopy to determine structures of excited, invisible protein states, J. Biomol. NMR 41 (2008) 113-120.

[7] F.A.A. Mulder, A. Mittermaier, B. Hon, F.W. Dahlquist, L.E. Kay, Studying excited states of proteins by NMR spectroscopy, Nat. Struct. Bio. 8 (2001) 932-935.

[8] H. Barjat, G.P. Chadwick, G.A. Morris, A.G. Swanson, The behavior of multiplet signals under radiation damping conditions .1. classical effects, J. Magn. Reson. A 117 (1995) 109-112.

(9) A. Vlassenbroek, J. Jeener, P. Broekaert, Radiation damping in high-resolution liquid NMR – a simulation study, J. Chem. Phys. 103 (1995) 5886-5897.

(10) S.Y. Huang, C. Anklin, J.D. Walls, Y.-Y. Lin, Sizable concentration-dependent frequency shifts in solution NMR using sensitive probes, J. Am. Chem. Soc. 126 (2004) 15936-15937.

(11) J.D. Walls, S.Y. Huang, Y.-Y. Lin, Excitation of magnetization using a modulated radiation damping field, J. Phys. Chem. B 110 (2006) 19985-19989.

(12) J.D. Walls, S.Y. Huang, Y.-Y. Lin, Spin amplification in solution magnetic resonance using radiation damping, J. Chem. Phys. 127 (2007) 054507.

(13) V.V. Krishnan, N. Murali, Radiation damping in modern NMR experiments: Progress and challenges, Prog. Nucl. Magn. Reson. Spectrosc. 68 (2013) 41-57.

(14) G. Zheng, W.S. Price, Solvent signal suppression in NMR, Prog. Nucl. Magn. Reson. Spectrosc. 56 (2010) 267-288.

(15) M.P. Augustine, Transient properties of radiation damping, Prog. Nucl. Magn. Reson. Spectrosc. 40 (2002) 111-150.

(16) D.J.-Y. Marion, H. Desvaux, An alternative tuning approach to enhance NMR signals, J. Magn. Reson. 193 (2008) 153-157.

(17) J.-H. Chen, A. Jerschow, G. Bodenhausen, Compensation of radiation damping during selective pulses in NMR spectroscopy, Chem. Phys. Lett. 308 (1999) 397-402.

(18) A.K. Khitrin, A. Jerschow, Simple suppression of radiation damping, J. Magn. Reson. 225 (2012) 14-16.

(19) E. Bendet-Taicher, N. Müller, A. Jerschow, Dependence of NMR noise line shapes on tuning, matching, and transmission line properties, Concepts Magn. Reson. 44 (2014) 1-11.

(20) J.-H. Chen, X.-A. Mao, Measurement of chemical exchange rate constants with solvent protons using radiation damping, J. Magn. Reson. 131 (1998) 358-361.

(21) J.-H. Chen, X.-A. Mao, Radiation damping transfer in nuclear magnetic resonance experiments via chemical exchange, J. Chem. Phys. 107 (1997) 7120-7126.

(22) J.-H. Chen, X.-A. Mao, C.-H. Ye, Intensity jumping and beating in inversion-recovery experiments of water due to radiation damping, J. Magn. Reson. 124 (1997) 490-494.

(23) J.-X. Guo, X.-A. Mao, Radiation damping induced half-frequency-spaced harmonic peaks in two-dimensional J-resolved NMR spectrum on liquid water, J. Phys. II 6 (1996) 1183-1193.

(24) S.Y. Huang, J.D. Walls, Y. Wang, W.S. Warren, Y.-Y. Lin, Signal irreproducibility in high-field solution magnetic resonance experiments caused by spin turbulence, J. Chem. Phys. 121 (2004) 6105-6109.

(25) S.Y. Huang, Y.-Y. Lin, N. Lisitza, W.S. Warren, Signal interferences from turbulent spin dynamics in solution nuclear magnetic resonance spectroscopy, J. Chem. Phys. 116 (2002) 10325-10337.

(26) Y.-Y. Lin, N. Lisitza, S. Ahn, W.S. Warren, Resurrection of crushed magnetization and chaotic dynamics in solution NMR spectroscopy, Science, 290 (2000) 118-121.

(27) S. Ahn, S. Lee, W.S. Warren, The competition between intramolecular J couplings, radiation damping, and intermolecular dipolar couplings in two-dimensional solution nuclear magnetic resonance, Mol. Phys. 95 (1998) 769-785.

(28) W.S. Warren, S.L. Hammes, J.L. Bates, Dynamics of radiation damping in nuclear magnetic resonance, J. Chem. Phys. 91 (1989) 5895-5904.

(29) Y.-Y. Lin, P. Hodgkinson, M. Ernst, A. Pines, A novel detection-estimation scheme for noisy NMR signals: Applications to delayed acquisition data, J. Magn. Reson. 128 (1997) 30-41.

Chapter 8

Core-Shell Nano-Platform for MR Theranostics

8.1 Introduction

A core-shell nano-platform can be composed of by a variety of materials. Though the core is surrounded by a hydrophilic shell, the overall structure is stabilized by covalent or ionic bonds between the core and shell. The physiological stability, surface modification simplicity, drug releasing ability [1, 2], and core and shell component flexibility [3, 4] of core-shell nano-plateforms show great promise for theranostic purposes. In this chapter, we aim to present the most recent developments of core-shell nano-platforms formed by co-polymers that consists of both hydrophobic and hydrophilic blocks. In the next chapter, we developed a theranostic core-shell nano-platform (UCS-Gd-DOX) that achieved a selective drug release (75% difference between pH 7.4 and 5.5) and MR imaging (r1 = 0.9 and 14.5 $mM^{-1}s^{-1}$ at pH 7.4 and 5.5, respectively). The anti-cancer effect of UCS-Gd-Dox is significantly better than free Dox in tumor-bearing mouse models, presumably due to enhanced permeability and retention effect and pH-triggered release. To the best of our knowledge, this is the simplest approach to obtain the theranostic NPs with Gd-conjugation and Dox doping.

The hydrophilic block of the copolymer (e.g. polyethylene glycol, PEG) often serves as the outer shell to provide good water solubility and biocompatibility, ultimately reducing premature clearance of core-shell nanoparticles, therefore prolonging the circulation time in the blood. Alternatively, the hydrophobic block of the copolymer provides sufficient interactions

with the typically hydrophobic anticancer drugs to increase the drug/contrast agent loading efficiency.

8.2 Core-Shell Nano-Platform as T2 Theranostic Agent

Certain sizes of nanoparticles and macromolecular drugs tend to accumulate in tumor tissue much more than they do in normal tissues [5-7], and is referred to as the enhanced permeability and retention (EPR) effect. Such phenomenon can be explained by the stimulated production of blood vessels from proximal fast-growing tumor cells. These newly formed vessels at the tumor site are usually abnormal in form and architecture, which leads to abnormal molecular and fluid transport dynamics. The EPR effect helps to deliver and distribute the nanoparticles inside the cancer tissue and therefore resulting in negative targeting (i.e. targeting without active targeting moieties). Filippousi*et. al.* [8] synthesized amphiphilic triblock copolymers of hydrophobic poly(propylene succinate) (PPSu) and hydrophilic poly(ethylene glycol) (PEG). The core-shell magnetic nanoparticles was formed by encapsulating magnetite (Fe3O4) and anticancer drug paclitaxel (Taxol) into the hydrophobic core. Furthermore, they prepared three copolymer samples with similar lengths of PEG blocks but with different lengths of PPSublocks, allowing for further investigation in the effect from the hydrophobic (PPSu) over hydrophilic (PEG) ratio of the polymeric matrix. All three samples exhibited satisfactory nanoparticle yield (ranging from 70.57% to 78.21%) and drug entrapment efficiency (ranging from 53% to 65%). However, the differences in the hydrophobic block among the three samples produced varying drug-releasing profile pattern in an *in vitro* environment. The copolymer sample of 5800 g/mol PPSu released approached 100% amount of Taxol loaded at about 25

hours; while the sample formed with 18900 g/mol PPSu did not release until 240 hours with a maximum release of 80%.

Schleich et al. [9] synthesized Taxol/SPIO-loaded PLGA-based nanoparticles by mixing poly(lactide-co-glycolide) (PLGA), poly(ε-caprolactone-b-ethylene glycol) (PCL-b-PEG),(PLGA-PEG), oleic acid-coated SPIO, and Taxol through emulsion-diffusion-evaporation. The resulting nanoparticles are composed of a hydrophobic core containing the SPIO and Taxol, and a PEG block hydrophilic shell. Such Taxol/SPIO-loaded nanoparticles possess a high r_2/r_1 ratio of 33.4 at 20 MHz, higher than the conventional available magnetic nanoparticle Resovist, presenting promising applications as T_2 contrast agent. Both *in vitro* cytotoxicity studies of CT26 colon carcinoma cells and *in vivo* anti-tumor studies of CT26-tumor-bearing mice had shown Taxol/SPIO-loaded nanoparticles inhibited the growth of CT26 cells. Based on the Kaplan-Meier survival rate analysis, the Taxol-load and Taxol/SPIO-loaded nanoparticles exhibited superior survival rates, with median survival rates of 13 and 15 days respectively, as opposed to the PBS administered control group with median survival rate of 9 days.

Even with the same copolymer composition, a different conjugated structure will affect the drug releasing characteristic. Wang *et. al.* [10] had synthesized two similar core-shell nanoparticles using Fe_3O_4-SiO_2, poly(benzyl L-aspartate) (PBLA), and methoxy poly(ethylene glycol) (mPEG). The first core-shell nanoparticle, FeSi@PBLA@mPEG, was synthesized by first conjugating PBLA with Fe_3O_4-SiO_2, then conjugating the methoxypoly(ethylene glycol) benzaldehyde(mPEG-CHO) onto the resulting nanoparticle through benzoic-imine bonds. The second core-shell nanoparticle FeSi@PBLA-mPEG was produced in a one-step conjugation of Fe_3O_4-SiO_2 to the diblock copolymer of mPEG-PBLA, where mPEG and PBLA were copolymerized through peptide bonds. Both core-shell nanoparticles were loaded with the

anticancer drug doxorubicin (DOX) to form the complexes FeSi@PBLA@mPEG@DOX and FeSi@PBLA-mPEG@DOX, respectively. *In vitro* drug release studies showed that in PBS buffer solution of pH 7.4, the drug release profile pattern of the two DOX-loaded core-shell nanoparticles are very similar, both being less than 25% after 50h. When the buffer was adjusted to an acidic environment with pH = 5.8, the release of DOX for FeSi@PBLA@mPEG@DOX was accelerated, and reached 45% after 50h. In contrast, FeSi@PBLA-mPEG@DOX did not show much difference between the acidic and neutral conditions. This difference in drug releasing behavior between the two core-shell nanoparticles is mainly attributed to the pH-sensitive benzoic-imine bonds between mPEG and PBLA in FeSi@PBLA@mPEG@DOX.

Alternatively, folic acid (FA) can serve as a targeting moiety, as it is able to enhance the targeting of the nano-platform to cancer cells through a folate receptor-mediated endocytosis. Patra*et. al.* [11] manufactured core-shell nanoparticles of SPION@PS-b-PAA-DOX/FA with an SPIO core containing a contrast agent, encompassed by a poly(styrene)-b-poly(acrylic acid) (PS-b-PAA) shell not only containing DOX for therapy, but also containing FA peripherally conjugated to the outer shell for recognition of the cancer site. Both the drug release profile and magnetization of such core-shell nanoparticles improved dramatically by altering the neutral physiological pH of 7.4 to an acid pH of 5.3. At pH = 5.3, the nanoparticle revealed an initial burst of drug release from 0% to 37%, reaching a final 92% after 160h. At pH = 7.4, however, only had an initial release from 0% to 12%, reaching a final release of 32%.

Additionally, the r_2 relaxivity of the nanoparticle at pH = 5.3 was found to be more than 5 times of that at pH = 7.4. This result was expected, as DOX is conjugated to the core-shell nanoparticle through a pH-sensitive hydrazine linkage. Further *in vitro* cell viability assays on human breast cancer SkBr3 cells and colon cancer HCT116 cells demonstrated that SPION@PS-

b-PAA-DOX/FA had a higher efficacy in killing cancer cells compared to free DOX, mainly because the conjugated drug had a faster internalization rate, as well as and longer retention time in the intracellular environment.

A recent study published by Ji *et. al.* [12] had depicted the synthesis of a hollow porous Fe_3O_4 ($HPFe_3O_4$) nanoparticle, loaded with DOX into the cavity, then self-assembled with the polymer of [7-(didodecylamino)coumarin-4-yl] methyl methacrylate (DDACMM) and poly(ethyleneglycol) (PEG). The complex was then conjugated with FA for selective cancer targeting, and was near-IR light responsive. The resulting $HPFe_3O_4$@DDACMM-PEG-FA nanoparticles showed continuous drug release under femtosecond pulse NIR laser exposure, with a final 24h release amount of 70% at pH = 5.0, and 50% at pH = 7.4. When placed in dark, however, less than 10% DOX was released during the 24h period, irregardless of the pH environment. *In vitro* MTT assay on folate receptor protein positive human KB FR(+) cells further verified this selective releasing under the presence of NIR exposure. The $HPFe_3O_4$@DDACMM-PEG-FA nanoparticles also possessed a high r_2 relaxation rate of 139.1 Fe mM^{-1} s^{-1}.

Cancer cell antigens are specific structural substances on the surface of cancer cells that can serve as a target for adaptive immuno-targeting. These antigens can be recognized and specifically bound by the corresponding antibody. Through the high selectivity and binding affinity between antibody and antigen, the nano-platform conjugated with antibody on the surface can be used to target corresponding cancer cells with high efficiency and specificity. This has been verified by *in vitro* and *in vivo* studies of drug-loaded magnetic core-shell nanoparticles conducted by Gao *et. al.* [13].

In their study, a core composed of poly(D,L-lactic-co-glycolic acid) (PLGA), anti-cancer drug docetaxel, and hydrophobic SPIONs, was first created using a single emulsion evaporation method, then subsequently conjugated with poly(allylamine hydrochloride) (PAH) and two different sized poly(ethylene glycol) (PEG) molecules through a layer-by-layer strategy. The outer shell PEG molecules had been conjugated with prostate stem cell antigen antibody (scAb), for a more specific targeting capability to prostate stem cell antigen-positive PC3M cells. This specific binding was confirmed by an *in vitro* cytotoxicity study of scAb-PLGA-SPIO/docetaxel (nano-platform conjugated with scAb) and PLGA-SPIO/docetaxel (without scAb) on PC3M cells and HT29 cells.

For PC3M cells, the half maximal inhibitory concentration (IC_{50}) of scAb-PLGA-SPIO/docetaxel was found to be significantly lower than that of PLGA-SPIO/docetaxel. In contrast, the prostate stem cell antigen-negative HT29 cells, revealed IC_{50} values with or without scAb to be very close. *In vivo* MRI and antitumor efficacy studies also confirmed the effective targeting of scAb-PLGA-SPIO/docetaxel to the tumor site. *In vivo* MRI showed a significant contrast between the tumor and muscle after the injection of either scAb-PLGA-SPIO/docetaxel or PLGA-SPIO/docetaxel, due to SPIO accumulation at the tumor site via EPR effect. However, scAb-PLGA-SPIO/docetaxel showed further contrast enhancement due to the additional antigen-antibody interaction. Furthermore, scAb-PLGA-SPIO/docetaxel induced a long-term tumor inhibition on PC3M tumor bearing mice and possessed the smallest mean tumor volume of $156.4\pm12.6mm^3$ (at 75 days) in comparison to other conditions. Specifically, without the antibody scAb, PLGA-SPIO/docetaxel, the tumor volume was found to be $269.9\pm225.4mm^3$ (at 72 days), free docetaxel tumor volume of about $500mm^3$ (at 57 days), and PBS tumor volume of about $750mm^3$ (at 33 days). As described, the copolymer sections in the core-shell nanoparticles

provide a variety of functional groups that can bind with different targeting moieties, which can be extended to other cancer types using such specific contrast-enhancement and targeting therapy through antigen-antibody interactions.

8.3 Core-Shell Nano-Platform as T1 Theranostic Agent

Polyelectrolyte multilayers are promising candidates as a material for the shell of core-shell nanoparticles for their pH-responsive encapsulation and release of drug. Huang *et. al.* [14] first synthesized Gd_2O_3:Yb^{3+}:Er^{3+}, a functionalized mesoporous silica nanoparticle (MSNs) core, which was then coated by multiple layers of the polyelectrolyte poly(allyamine hydrochloride) (PAH) and poly(sodium 4-styrenesulfonate) (PSS) using a layer-by-layer (LbL) technique. DOX was then loaded onto the polyelectrolyte shell in a strong acidic condition (pH = 2.0). The resulting DOX-loaded core-shell nanoparticles had a r_1 rate of 7.35 s^{-1} mM^{-1}. While less than 10% DOX was released over a 72h period in a PBS buffer at pH = 7.4, more than 60% DOX was released within 72h at pH = 5.2. *In vitro* cytotoxicity studies on MCF-7 breast cancer cells showed that both DOX-loaded nanoparticles and free DOX exhibited a high cytotoxicity, where the former exhibited a higher cytotoxicity than the latter. However, this higher cytotoxicity in the DOX-loaded nanoparticles should not be attributed to the platform itself, as the core-shell nanoparticles without DOX had negligible cytotoxic effects on MCF-7 cells. The authors attributed this enhanced performance to the acidic microenvironment of endosomes and lysosomes, as well as the weakly acidic extracellular environment at the tumor site, which in turn, likely benefited a more effective releasing of DOX inside tumor cells.

Our group and collaborators [15] have synthesized a unibody core-shell (UCS) nanoparticle using a polymer platform formed by resorcinol and 1,3-phenylenediamine

monomers. In the two-step synthesis process, Gd^{3+} was first conjugated to the polymer backbone to form the Gd-core, then DOX was encapsulated within the shell surrounding the Gd-core. Resorcinol was chosen as one of the components in the core for its stabilizing hydroxyl groups at the physiological pH ranges of interest. 1,3-phenylenediamine was chosen as the shell unit for its capability to perform a pH controllable release function using its amino groups, as demonstrated in Fig. 1. In addition, hydrophobic patches in 1,3-phenylenediamine provide tight packing of DOX molecules, resulting in a superior drug loading efficiency of 97.5%. The design of such UCS-Gd-DOX takes advantage of the acidic pH values of some malignant tumor tissues, ranging around 6.5 [16, 17].

In vitro and *in vivo* studies of UCS-Gd-DOX as an innovative theranostic nanoparticle showed that: (1) the presence of DOX in the shell is able to be effectively and selectively released under an acidic environment (pH = 5.5) compare to a weakly basic(pH = 7.4) physiological environment as in the blood; (2) the signal-to-noise ratio (SNR) of the "region of interest" (ROI) after injection has been improved by 10-30% (n = 3 mice). *In vitro* drug release studies showed that at pH = 8.0, 7.0, 6.0, 5.0, and 4.0, the release of DOX after 2h was found to be <5%, 10%, 55%, 75%, and 80% respectively. The increase in release of DOX in an acidic environment should be attributed to the protonation of polymer backbone. The notable increase in drug release from pH = 7.0 to pH = 6.0 verified the potential of UCS-Gd-DOX for targeted therapy towards malignant tumor tissues. In addition, based on data acquired from *in vitro* T_1-weighted MR images, T1 relaxivity of UCS-Gd-DOX at pH = 5.5 was found to be 14.5 mM^{-1} s^{-1}, which was significantly higher than that of UCS-Gd-DOX at pH = 7.4 (0.9mM^{-1} s^{-1}), and overall reflecting the pH-switchable MR contrast capability of UCS-Gd-DOX. We hypothesize this pH-

switchability is a result of replacing water molecules with DOX in the shell under an acidic condition.

In vivo multiple-slice MR data on 3 mice are shown in Fig. 2, where T_1-weighted images of NOD/SCID mice with heterotopic, subcutaneous human cervical cancers were acquired and processed with "maximum intensity projection (MIP)". As shown in Fig. 2 (a), (b), and (c), the contrast of tumor area increases with time up to 250 min after the injection of UCS-Gd-DOX. This longer contrast enhancement period compared to free Gd-DPTA may be contributed to the longer circulation time of nanoparticles in the blood [18].

The pH-responsive design of the unibody core-shell nanoparticle not only improved the MRI contrast at the tumor site in respect to other tissue/organs, but also successfully suppressed the growth of the subcutaneous human cervical cancer in mouse xenograft models. As a theranostic nanoparticle with Gd-conjugation and DOX doping can be synthesized in a straightforward approach, we anticipate further expansive applications of UCS-Gd-DOX in the field of cancer treatment.

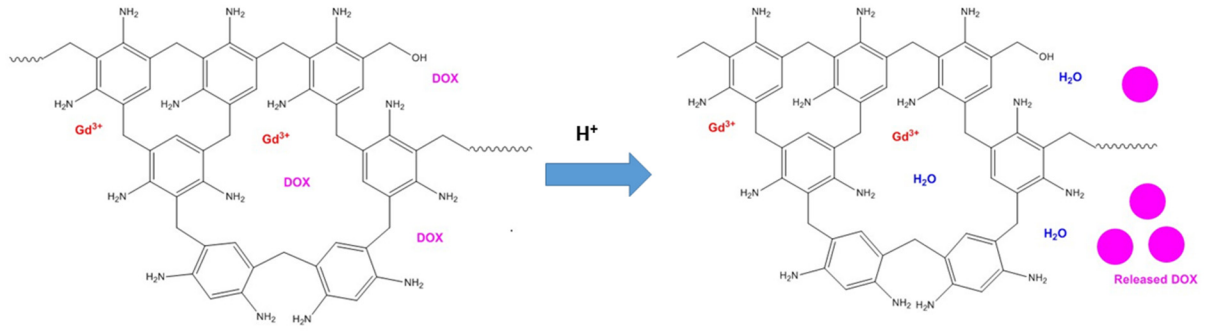

Figure 1. pH controllable drug delivery and contrast-enhanced MR imaging based on the core-shell smart polymer nanoparticles. At low pH, protonation of amino groups on the shell leads to releasing of the DOX molecules to bulk solution. Upon releasing, the empty scaffolds of shell allow the entrance of water molecules to interact with the inner-layered Gd, thus switching on the contrast.

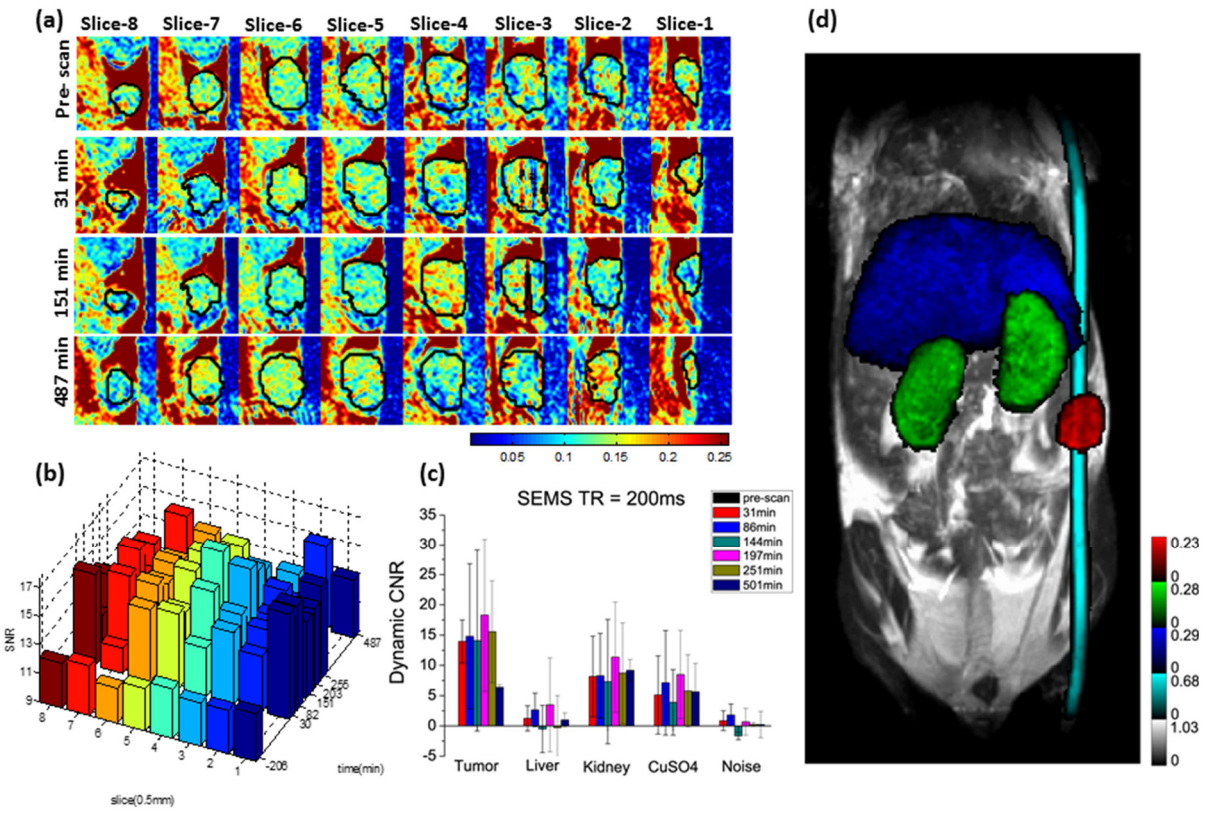

Figure 2. MR analysis of human cervical cancer bearing mice using UCS-Gd-DOX. (a) 2D-slice images of tumor of mouse C, the tumor is indicated with black circles and the color bar indicates the MR signal intensity. Only the image pixels with intensity values between ±2 standard deviation (STD) of ROI were kept to avoid image artifacts. (b) Signal-to-noise ratio (SNR) for each slice in (a) at time point: pre-scan (-206 min), 30 min, 82 min, 151 min, 203 min, 255 min, and 487 min. (c) Contrast-to-noise ratio (CNR) of tumor, liver, kidney, CuSO4, and noise area before and after the injection. Here define CNR % = [SNR(after-injection)-SNR(pre-injection)]/SNR(pre-injection) %. Error bars represent means ± standard deviation (n = 3 mice). (d) T1-weighted MR images acquired by "spin-echo multiple slices" (SEMS) and then processed by "maximum intensity projection". Repetition time (TR) = 200 ms, echo time (TE) = 10 ms, field of view (FOV) = 64 × 32 mm^2, matrix size = 256 × 128, slice thickness = 0.5 mm. The ROI of tumor, liver, kidney, and CuSO4 reference are indicated with red, blue, green, and cyan shade, respectively.

8.4 References

[1] Li Y, Xiao K, Luo J, Lee J, Pan S, Lam KS. A novel size-tunable nanocarrier system for targeted anticancer drug delivery. J. Control. Release 2010; 144: 314–323.

[2] Liu S, Han MY. Silica-coated metal nanoparticles. Chem Asian J 2010; 5: 36–45.

[3] Wei A, Leonov AP, Wei Q. Gold nanorods: multifunctional agents for cancer imaging and therapy, Methods MolBiol 2010; 624: 119–130.

[4] Sokolov K, Tam J, Travis K, Larson T, Aaron J, Harrison N, Emelianov S, Johnston K. Cancer imaging and therapy with metal nanoparticles, ConfProc IEEE Eng Med BiolSoc 2009; 2009: 2005–2007.

[5] Matsumura Y, Maeda H. A new concept for macromolecular therapeutics in cancer chemotherapy: mechanism of tumoritropic accumulation of proteins and the antitumor agent smancs, Cancer Research 1986; 46: 6387–92.

[6] Duncan R, Sat Y-N. Tumour targeting by enhanced permeability and retention (EPR) effect, Ann Oncol 1998; 9: 39.

[7] Vasey PA, Kaye SB, Morrison R, Twelves C, Wilson P, Duncan R, Thomson AH, Murray LS, Hilditch TE, Murray T, Burtles S, Fraier D, Frigerio E, Cassidy J. Phase I clinical and pharmacokinetic study of PK1 [N-(2-hydroxypropyl)methacrylamide copolymer doxorubicin]: first member of a new class of chemotherapeutic agents-drug-polymer conjugates. Cancer Research Campaign Phase I/II Committee, Clin Cancer Res 1999; 5(1): 83–94.

[8] Filippousia M, Papadimitrioub SA, Bikiarisb DN, Pavlidouc E, Angelakerisc M, Zamboulisd D, Tiana H, Van Tendelooa G. Novel core–shell magnetic nanoparticles for Taxol

encapsulation in biodegradable and biocompatible block copolymers: Preparation, characterization and release properties, Int J Pharm 2013; 448 (1): 221-230.

[9] Schleich N, Sibret P, Danhier P, Ucakar B, Laurent S, Muller RN, Jérôme C, Gallez B, Préat V, Danhier F. Dual anticancer drug/superparamagnetic iron oxide-loaded PLGA-based nanoparticles for cancer therapy and magnetic resonance imaging, Int J Pharm 2013; 447(1-2): 94-101.

[10] Wang J, Gong C, Wang Y, Wu G. Magnetic nanoparticles with a pH-sheddable layer for antitumor drug delivery, Colloids Surf B Biointerfaces 2014; 118: 218-25.

[11] Patra HK, Khaliq NU, Romu T, Wiechec E, Borga M, Turner APF, Tiwari A. MRI-Visual Order–Disorder MicellarNanostructures for Smart Cancer Theranostics, AdvHealthc Mater 2014; 3(4): 526–535.

[12] Ji W, Li N, Chen D, Jiao Y, Xu Q, Lu J. A hollow porous magnetic nanocarrier for efficient near-infrared light- and pH-controlled drug release, RSC Adv 2014; 4: 51055-51061.

[13] Gao X, Luo Y, Wang Y, Pang J, Liao C, Lu H, Fang Y. Prostate stem cell antigen-targeted nanoparticles with dual functional properties: in vivo imaging and cancer chemotherapy, Int J Nanomedicine 2012; 7: 4037-51.

[14] Huang S, Cheng Z, Chen Y, Liu B, Deng X, Ma P, Lin J. Multifunctional polyelectrolyte multilayers coated onto Gd_2O_3:Yb^{3+},Er^{3+}@MSNs can be used as drug carriers and imaging agents, RSC Adv, 2015; 5: 41985-41993.

[15] Ho L-C, Hsu C-H, Ou C-M, Wang C-W, Liu T-P, Hwang L-P, Lin Y-Y, Chang H-T. Unibody core-shell smart polymer as a theranostic nanoparticle for drug delivery and MR imaging, Biomaterials 2015; 37: 436-446.

[16] Murgia S, Bonacchi S, Falch AM, Lampis S, Lippolis V, Meli V, Monduzzi M, Prodi L, Schmidt J, Talmon Y, Caltagirone C. Drug-loaded fluorescent cubosomes: versatile nanoparticles for potential theranostic applications. Langmuir 2013; 29: 6673-6679.

[17] Caltagirone C, Falchi AM, Lampis S, Lippolis V, Meli V, Monduzzi M, Prodi L, Schmidt J, Sgarzi M, Talmon Y, Bizzarri R, Murgia S. Cancer-cell-targeted theranosticcubosomes. Langmuir 2014; 30: 6228-36.

[18] Vexler VS, Clement O, Schmittwillich H, Brasch RC. Effect of varying the molecular-weight of the MR contrast agent Gd-DTPA-polylysine on blood pharmacokinetics and enhancement patterns, J MagnReson Imaging 1994; 4: 381-388.

Chapter 9

MR Theranostic Hyperthermia: Thermodynamic Behavior and Aggregation/Disruption of Monomers/Clusters

9.0 Abstract

Magnetic resonance hyperthermia is a new nano-medical therapy that emerges in recent years. In the presence of external alternating magnetic fields produced by MR instruments, magnetic nanoparticles accumulated at the tumor site can generate heat through Neel relaxation and/or Brownian relaxation. Through magnetic resonance hyperthermia, magnetic nanoparticles can serve as "molecular bullets" to kill cancer cells, leaving surrounding healthy tissues unaffected. Such hyperthermic effects can also be used for thermal activation and control releasing of cancer drugs. One major challenge of magnetic resonance hyperthermia is to optimize the heating efficiency of magnetic nanoparticle suspension. Heating efficiency depends on the size, physical properties, and aggregation state of magnetic nanoparticles. In this study, the thermodynamic behavior of magnetic nanoparticles and the aggregation/disruption of monomers/clusters under different temperatures were studied by 3D Metropolis Monte Carlo method. The relationship between the critical temperature for aggregation/disruption and the frequency of external magnetic field has been established through revised Langevin function. Simulation results show that the relative content of aggregates in colloidal magnetic nanoparticle suspension decreased with the increase of temperature, and the aggregates disrupted completely into monomers at or above the critical temperature. In addition, increasing the frequency of

external alternating magnetic field significantly lowered down the critical temperature, and there existed a critical frequency where the critical temperature stabilized and became unaffected by the frequency. Preheating the suspension under critical frequency will disrupt the aggregates into monomers and thus optimize the heating efficiency of magnetic nanoparticles.

9.1 Introduction

Magnetic nanoparticles have found popular applications in magnetic resonance molecular imaging and nanomedicine for medical diagnosis and therapy. Because these nanoparticles are biocompatible, injectable, nontoxic, and are able to target specific tissues through specific (e.g., antibody-antigen) and non-specific (e.g., enhanced permeability and retention effect) targeting mechanisms, they can serve as "molecular beacons" to enhance the MR image contrast for early tumor detection. Moreover, through interacting with external alternating magnetic fields, these magnetic nanoparticles accumulated at the tumor site can generate heat through Neel relaxation and/or Brownian relaxation [1-4]. Through magnetic resonance hyperthermia, magnetic nanoparticles can serve as "molecular bullets" to kill cancer cells, leaving surrounding healthy tissues unaffected. Such hyperthermic effects can also be used for thermal activation and control releasing of cancer drugs.

However, pre-clinical and clinical applications of magnetic resonance hyperthermia with magnetic nanoparticles is limited by a few major theoretical difficulties and experimental challenges. For example, conventional theoretical models for magnetic resonance hyperthermia assume that the magnetic nanoparticles act independently as single units and are dispersed uniformly in the colloidal suspension, thus making the interaction among the nanoparticles negligible. However, in real biomedical applications, when magnetic nanoparticles have been

injected into blood vessels or been bound to cancer cells through the antibody-antigen interaction, individual nanoparticles are highly likely to aggregate and form clusters. The resulting aggregation state changes the physical properties of the magnetic nanoparticle suspension, such as magnetic susceptibility. Furthermore, aggregate formation and disruption were found to be affected by external magnetic field conditions [5]. Consequently, a higher magnetic field strength is required to disrupt these aggregates, lowering the overall heating efficiency of the magnetic nanoparticle suspension. To optimize the heating efficiency for magnetic resonance hyperthermia, further understanding and formulation of aggregate formation and disruption is needed.

Previous magnetic resonance experiments have demonstrated that the thermal disruption of magnetic nanoparticle dimers is a second-order phase transition, [6] where the critical temperature for this second-order phase transition was then further characterized [7]. The inverse susceptibility-temperature curve of magnetic nanoparticle aggregates was also shown to respond differently to the frequency of the external magnetic field [8]. Because the critical temperature is a function of the external alternating magnetic field frequency and the heat-generation mechanism is closely related to the relaxation effects under such magnetic field, the frequency at which the aggregates of magnetic nanoparticles completely disrupt into monomers can be described by the critical temperature. In this chapter, we aim to illustrate the relationship between the critical temperature and its corresponding critical frequency by a revised Langevin function. 3D cluster-moving based Metropolis Monte Carlo method is used to simulate the thermodynamic behavior and the aggregation/disruption of the magnetic nanoparticles under different temperatures. This critical frequency can then serve as an important reference for optimizing the heating efficiency of the magnetic nanoparticles. We hypothesize that preheating

the magnetic nanoparticles at the critical frequency to disrupt all clusters present in the colloidal suspension can minimize the loss of energy and therefore optimize the heating efficiency for magnetic resonance hyperthermia

9.2 Theory

9.2.1 Formation of aggregates among magnetic nanoparticles

At room temperature, magnetic nanoparticles are stabilized in the colloidal suspension by various interactions [9] between nanoparticles, including inter-particle repulsions (e.g., electrostatic repulsion and steric repulsion) and inter-particle attractions (e.g., magnetic dipole-dipole interaction and van der Waals force). For example, for any two magnetic nanoparticles i and j with center-to-center distance r, if we assume the surface distance between these two particles is x, radii R_i and R_j, magnetic moments m_i and m_j, thickness of surface coating δ, and the distance vector pointed from nanoparticle i to j is R_{ij}, then the interaction energies among magnetic nanoparticles can be described as:

$$U_d = \frac{\mu_0}{4\pi}\left[\frac{m_i \cdot m_j}{{R_{ij}}^3} - 3\frac{(m_i \cdot R_{ij})(m_j \cdot R_{ij})}{{R_{ij}}^5}\right] \quad (1)$$

$$U_v = -\frac{A}{6}\left[\frac{2}{s^2-4} + \frac{2}{s^2} + \ln\left(\frac{s^2-4}{s^2}\right)\right] \quad (2)$$

$$U_e = \frac{\epsilon R \sigma^2}{2}\exp\left(-\frac{x}{\lambda}\right) \quad (3)$$

$$U_s = 2\pi R^2 N'\left[2 - \frac{l+2}{t}\ln\left(\frac{2(1+t)}{2+l}\right) - \frac{l}{t}\right](k_B T) \quad (4)$$

and the total interaction energy as:

$$U = U_d + U_v + U_e + U_s \quad (5)$$

where μ_0 is the permeability of free space, A the Hamaker constant for van der Waals interaction (associated with the magnetic nanoparticle surface coating layer and the dielectric properties of

carrier liquid), ϵ the dielectric constant of the solvent, σ the surface potential of the particle, λ the Debye length, k_B the Boltzmann constant, T the absolute temperature of colloidal magnetic nanoparticle suspension, and N' the number of molecules adsorbed on the surface of nanoparticles. $s = \frac{x}{R} + 1$, $l = \frac{R_{ij}-2R}{R}$, $t = \frac{\delta}{R}$. U_d, U_v, U_e, and U_s denote the magnetic dipole-dipole interaction, van der Waals' interaction, electrostatic repulsion, and steric repulsion, respectively. For the diluted nanoparticle concentrations used in MR nanomedical, theranostic applications, only the dominating dipole-dipole interaction term is considered. With higher nanoparticle concentrations and thus closer nanoparticle spacing, multipolar interactions need to be included as well [2]. Consequently, the interactions between magnetic nanoparticles depend on a number of factors such as temperature, magnetic field strength, particle size, and particle concentration (since the concentration determines the distance between the nanoparticles). The kinetic energy of the nanoparticles is not sensitive to the parameters such as temperature, magnetic field strength, particle size, and particle concentration, and therefore can be conveniently neglected (i.e., treated as a constant).

The colloidal magnetic nanoparticle suspension must sustain a balance between attraction and repulsion to maintain the stability, as any change in the external environment, such as temperature, concentration, or applied magnetic field, can influence the interaction among nanoparticles. For example, when the mutual repulsion among particles is smaller than the mutual attraction, magnetic nanoparticles tend to aggregate; in contrast, when the repulsion is larger than the attraction, magnetic nanoparticle aggregates will be disrupted into individual particles. For a certain colloidal magnetic nanoparticle suspension, adjusting experimental parameters and therefore controlling the aggregation/disruption of magnetic nanoparticles is essential for optimizing the heating efficiency of magnetic resonance hyperthermia.

9.2.2 Critical frequency and critical temperature under an alternating magnetic field

The relative amounts of monomers and clusters in the colloidal magnetic nanoparticle suspension can be expressed as P_m and P_c [10], respectively:

$$P_m = \frac{T}{T^*} \tag{6}$$

$$P_c = (1 - \frac{T}{T^*})^{\frac{1}{2}} \tag{7}$$

where T is the absolute temperature of suspension and T^* the critical temperature for second-order phase transition. Based on the Langevin function, the equilibrium magnetic susceptibility for the mixed system can thus be described as [10]

$$\chi(T) = \frac{\phi}{H_0}\left[M_{dm}\left(\frac{T}{T^*}\right)\left(\coth\left(\frac{\mu_0 m H_0}{k_B T}\right) - \frac{k_B T}{\mu_0 m H_0}\right) + M_{dc}(1 - \frac{T}{T^*})^{\frac{1}{2}}\coth\left(\frac{\mu_0 \overline{m_c} H_0}{k_B T}\right) - \frac{k_B T}{\mu_0 \overline{m_c} H_0}\right] \tag{8}$$

where k_B represents the Boltzmann constant, ϕ the volume fraction of magnetic nanoparticle, H_0 the strength of external alternating magnetic field, μ_0 the permeability of free space, M_{dm} and M_{dc} the saturation magnetization for monomers and clusters, respectively, and m and $\overline{m_c}$ the average magnetic moment for monomers and clusters, respectively. When excited by an external magnetic field, magnetic nanoparticles generate heat through relaxation mechanisms, such as Brownian relaxation and Neel relaxation [11-14]. The power dissipation can be expressed as [12]

$$P = \mu_0 \pi f {H_0}^2 \chi'' = \frac{2\mu_0 {H_0}^2 (f\pi)^2 \tau \chi(T)}{1+(2\pi f\tau)^2} \tag{9}$$

A portion of the dissipated energy contributes to the raise in temperature of magnetic nanoparticles, where another portion to the acceleration of aggregate disruption. This distribution results in a lower critical temperature for the second order phase transition. If the unmodified critical temperature is given by ${T_0}^*$, the frequency of the magnetic field as f, and the heating duration as Δt, the critical temperature can be revised to a function of frequency [8]

$$T^*(f) = {T_0}^* - P \cdot \Delta t = {T_0}^* - \frac{2\mu_0 {H_0}^2 \Delta t (f\pi)^2 \tau \chi(T)}{1+(2\pi f\tau)^2} \quad (10)$$

If the heating duration is fixed, then the relationship between the critical frequency f^* and critical temperature $T^*(f^*)$ can be represented as

$$T^*(f^*) = {T_0}^* - P \cdot \Delta t = {T_0}^* - \frac{2\mu_0 {H_0}^2 \Delta t (f^*\pi)^2 \tau \chi(T)}{1+(2\pi f^*\tau)^2} \quad (11)$$

9.3 Methods

3D cluster-moving based Metropolis Monte Carlo method was used to simulate the thermodynamic behavior and to study the aggregation/disruption of magnetic nanoparticles at various temperatures. The Metropolis Monte Carlo method provides a universally applicable model and faster convergence. For this simulation, the magnetic nanoparticles were assumed to be distributed in a 3D cube, and their size as a log-normal distribution to ensure the model similar to the experimental scenario [15].

9.3.1 Setup of model and parameters

The magnetic nanoparticles were set to have sizes following a log-normal distribution ($\overline{D}$, σ) and distributed randomly in a cube with edge L. The diffusion is modeled by a random walk. The thickness of surface coating of each nanoparticle is set as δ, the total number of magnetic nanoparticles as N, the volume fraction of magnetic nanoparticles as ϕ, and the saturation magnetization as M. The magnetic moment can thus be represented as $m = \frac{\pi M D^3}{6}$, pointing to an arbitrary angle that ranges from 0 to 2π. For any magnetic nanoparticle i, its current state can be determined by four variables (x_i, y_i, z_i, θ_i), where (x_i, y_i, z_i) denotes the spatial coordinates and θ_i the angle between the magnetic moment m_i and external magnetic

field H. The distance vector points from nanoparticle i to j was set as R_{ij}, and the unit vector r_{ij} was set in the same direction as R_{ij}, where n_i and n_j are unit vectors along the direction of magnetic moment m_i and m_j, respectively. The total energy U_i of any magnetic nanoparticle i under the external magnetic field can then be written as

$$U_i = U_{di} + U_{vi} + U_{ei} + U_{si} + U_{hi} \tag{12}$$

where U_{di} signifies the magnetic dipole-dipole interaction, U_{vi} the van der Waals' interaction, U_{ei} the electrostatic repulsion, U_{si} the steric repulsion, and U_{hi} the interaction between individual nanoparticle and the external magnetic field. However, in our simulation considering about the general case, electrostatic repulsion was neglected since neutralized free magnetic particles dispersed in suspension, so the common interactions among magnetic nanoparticles were magnetic dipole-dipole interaction, van der Waals' interaction and steric repulsion.

The specific values of parameters used in the computer simulation include the average diameter of the magnetic nanoparticles $\overline{D} = 11.5\,nm$, standard deviation of the particle size distribution $\sigma = 0.20\,nm$, volume fraction $\phi = 0.01$, total number of magnetic nanoparticles $N = 300$, edge of the cube $L = 167.25\overline{D}$, thickness of the surface coating $\delta = 0.15\overline{D}$, saturated magnetization $M = 414\,kA/m$, magnetic field strength $H = 400\,A/m$, permeability of free space $\mu_0 = 4\pi \times 10^{-7}\,H/m$, Boltzmann constant $k_B = 1.38 \times 10^{-23}\,J/K$, Hamaker constant $A = 10^{-19}J$ (corresponding to common organic layers surface coating such as glycerol in water solution), and total number of molecules absorbed on the surface per surface area $N' = 10^{18}\,/m^2$.

9.3.2 Cluster-moving-based Metropolis Monte Carlo simulation

The interactions within the aggregating magnetic nanoparticle clusters are stronger than the interactions between clusters and the surrounding monomers in an actual colloidal magnetic nanoparticle suspension. The nanoparticle dynamics can be described by deterministic equations (e.g., Newton's second law) or stochastic equations (e.g., Fokker–Planck equation). In our molecular dynamics simulations, without loss of generality and accuracy, the nanoparticle dynamics is approximated by 3D random walk with fixed step length and variable walking direction (uniform sampling in the spherical coordinates) that satisfy the experimental translational and rotational diffusion coefficients. The choices of step length, 0.5D, and maximum rotation angle per step, pi/18, is to speed up the expensive calculation without compromising the accuracy.

To better simulate the effect resulting from changes in position and energy, a cluster-moving algorithm was employed to describe particles' random walk. The procedures for the cluster-moving-based Metropolis Monte Carlo simulation are described as follows:

(1) Initialize the system and all parameters.

(2) Change the state of the i^{th} ($i = 1,2,3 \ldots N$) magnetic nanoparticle (x_i, y_i, z_i, θ_i).

(3) Calculate the energy change for the system, $\Delta U = U_{current} - U_{previous}$, and verify whether the new state is acceptable by the Metropolis algorithm, as the system always prefers lower energy during evolution. If $\Delta U < 0$, then accept the new state of the i^{th} magnetic nanoparticle. If $\Delta U > 0$, then calculate $h = exp(-\frac{\Delta U}{k_B T})$ and compare to $temp$, a random number ranges from 0 to 1. If $h > temp$, accept the new state. If $h < temp$, reject the new state and maintain the previous state of the i^{th} magnetic nanoparticle.

(4) Repeat step (2) and (3) until the states of all *N* magnetic nanoparticles have been

changed. Record current Monte Carlo steps $N_m = 1$.

(5) Calculate the surface distance among all magnetic nanoparticles in the suspension. If the distance is smaller than $0.25\overline{D}$, assume an aggregate is formed.

(6) Repeat steps (2) through (5) until $N_m = 2000000$ to ensure the system has reached equilibrium.

To avoid complicated calculations for the center of mass of aggregates, the movement, orientation, and magnetic moment of an aggregate were represented by those of an arbitrary particle within that aggregates. The steps for each random walk were set as $S = 0.5\overline{D}$, and the rotation angle for the magnetic moment as $\Delta\theta = \frac{\pi}{18}$.

9.4 Results and Discussion

9.4.1 Simulation results of the aggregates formation

By employing the 3D cluster-moving-based Metropolis Monte Carlo method, we studied the thermodynamic behavior of 300 magnetic nanoparticles with a temperature range from 300 K to 450 K (27 ℃ to 177 ℃). The formation and disruption of magnetic nanoparticle aggregates at different temperatures were analyzed by calculating the interactions between the magnetic nanoparticles. To highlight this point, we randomly chose one magnetic nanoparticle and calculated its interaction energies evolving with Monte Carlo steps at T=300 K according to equation (12), as shown in Table.1. What's more, by assuming clusters would form when the surface distance between particles is smaller than $0.25\overline{D}$, we obtained the distribution of monomers and aggregates when the system is at equilibrium, as illustrated in Fig. 1. At room temperature T=300 K and T=310 K, aggregates with various size/structure were formed among magnetic nanoparticles. However, when the temperature was increased to T=350 K and T=360

K, aggregates first disrupted into smaller portions, then into monomers. When the temperature was further increased to T=400 K and T=450 K, the majority of the nanoparticles in the system was in the monomeric form. It suggests that the attractive and repulsive interactions become balanced at higher temperatures.

Table 1. Interaction energies (in Joule) of randomly chosen magnetic nanoparticle evolving with Monte Carlo steps at T=300 K

Monte Carlo Steps	U	U_d	U_v	U_s	U_h
0	1.7770×10^{-21}	3.8729×10^{-24}	-5.2130×10^{-27}	1.8267×10^{-21}	-5.3522×10^{-23}
10	3.1940×10^{-21}	4.5583×10^{-23}	-2.3155×10^{-27}	3.3207×10^{-21}	-1.3127×10^{-22}
100	3.6034×10^{-21}	9.5663×10^{-24}	-4.6260×10^{-27}	3.7501×10^{-21}	-1.5693×10^{-22}
1000	2.5901×10^{-21}	2.6149×10^{-24}	-2.0991×10^{-27}	2.6828×10^{-21}	-9.5298×10^{-23}
10000	3.7607×10^{-21}	1.0562×10^{-23}	-2.8352×10^{-27}	3.9184×10^{-21}	-1.6821×10^{-22}
50000	1.8502×10^{-21}	-6.3504×10^{-26}	-1.6851×10^{-26}	1.9074×10^{-21}	-5.7140×10^{-23}

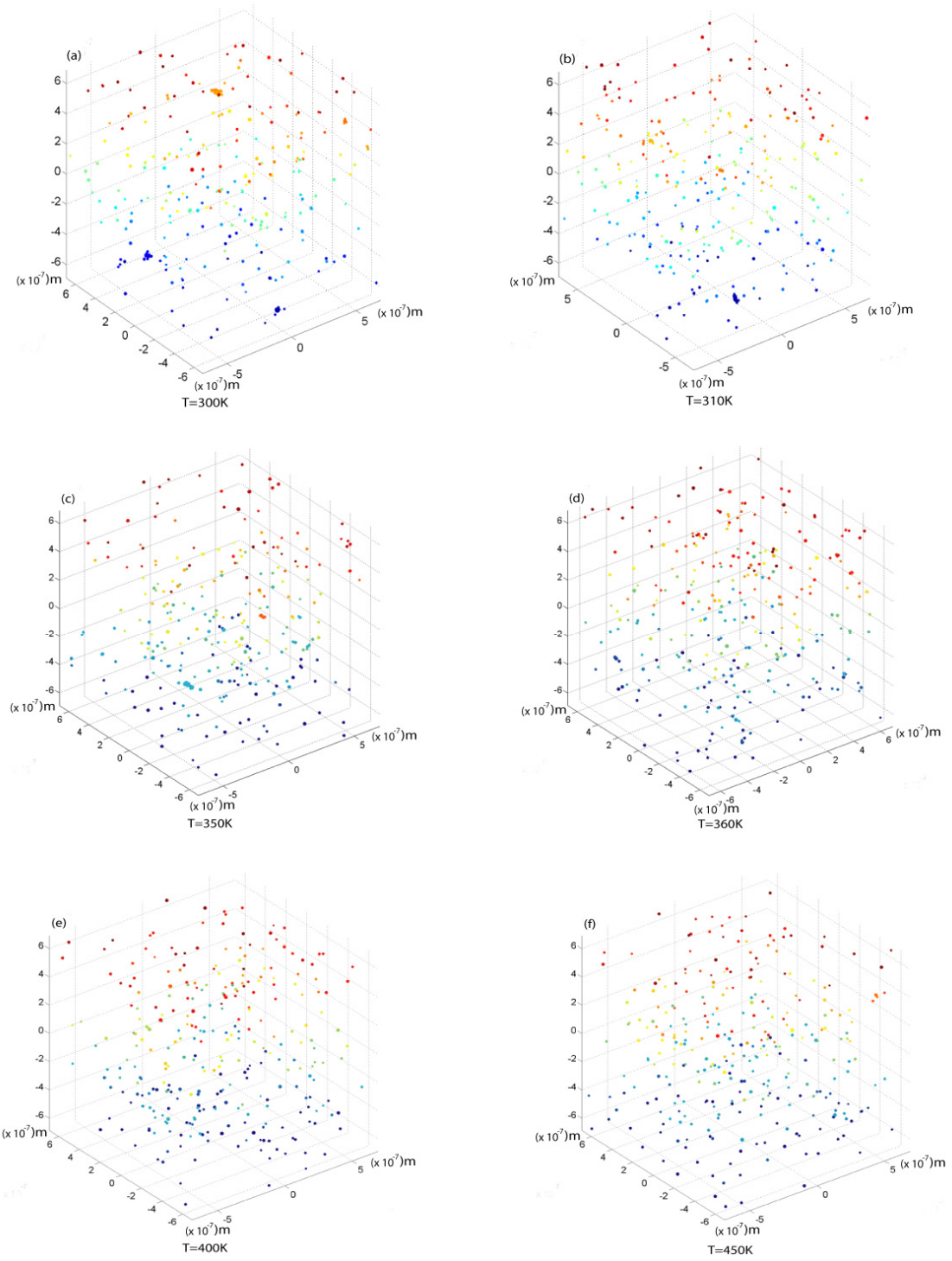

Figure 1. Distribution of monomers and clusters in magnetic nanoparticle suspension at equilibrium at different temperatures. (a) T=300 K (b) T=310 K (c) T=350 K (d) T=360 K (e) T=400 K (f) T=450 K. To aid the 3D visual effect, z-coordinates of the magnetic nanoparticles are color-coded.

Based on the simulation results, the relative contents of aggregates and monomers in the magnetic nanoparticle suspension were assessed at different temperatures, as shown numerically in Table. 2 and diagrammatically in Fig. 2. With the elevation of temperature, the relative content of monomers was found to increase, while that of aggregates to decrease. Fluctuations observed in Fig. 2 are mainly due to the disruption of larger aggregates into smaller portions, resulting in a relative increase in the number of aggregates.

Table 2. The number and relative content of both monomers and aggregates in suspension at different temperature

Temperature	Aggregates	Monomers	Relative Content
300 K	16	249	0.064
310 K	18	252	0.071
320 K	17	253	0.067
330 K	15	258	0.058
340 K	14	260	0.053
350 K	14	266	0.053
360 K	16	266	0.060
370 K	15	270	0.056
380 K	10	276	0.036
390 K	11	276	0.040
400 K	11	277	0.040
450 K	6	288	0.021

9.4.2 Analysis of the critical frequency for aggregates disruption

According to equations (10) and (11), the critical temperature can be reduced if an external alternating magnetic field with higher frequency is applied. To further explore the

relationship between the critical temperature and magnetic field frequency, the critical temperature was plotted as a function of magnetic field frequency under various scenarios shown in Fig. 3. All results revealed similar trends where the critical temperature decreased dramatically as the frequency increased from 0 Hz, but remained unaffected once the frequency reached a certain critical value. Such critical value of the frequency is then defined as the "critical frequency" of the corresponding colloidal magnetic nanoparticle suspension. Heating at or above the critical frequency can optimize the heating efficiency, resulting in the complete disruption of aggregates into monomers.

Figure 3(a) shows curves of the critical temperature vs. magnetic field frequency for suspensions containing four commonly used magnetic materials (listed in Table 3). When the magnetic field frequency is lower than 300 Hz, the critical temperature dramatically decreases with the increase in frequency. Continual increase in frequency does not result in a further obvious decrease in critical temperature, while at frequency values higher than 500 Hz, the critical temperature no longer decreases, but rather becomes stable. This indicates a critical

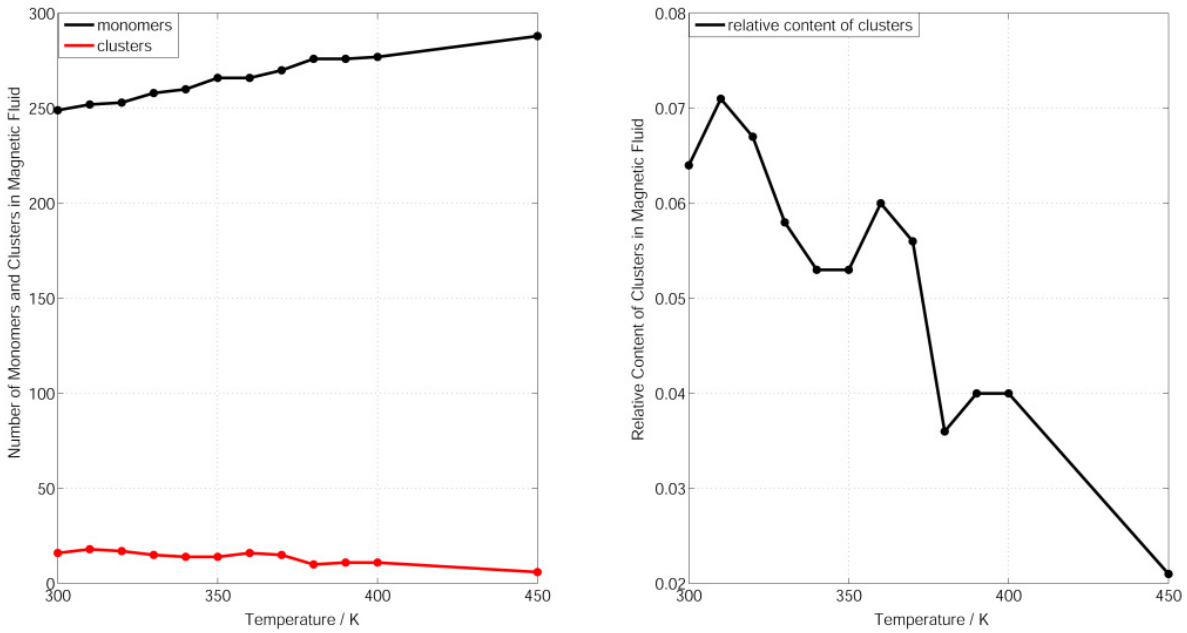

Figure 2. Relative content of clusters in suspension at different temperatures.

frequency of around 500 Hz for all of the four magnetic materials studied, despite of their different final critical temperatures, range from 354 K to 362 K.

In a real suspension, the sizes of magnetic nanoparticles usually obey the log-normal distribution with a certain standard deviation. Therefore we take magnetite, which is the most strongly magnetic mineral in nature, as an example and further discuss how the size distribution of magnetic nanoparticles affects the relationship between the critical temperature and the magnetic field frequency. When the mean diameter of the magnetic nanoparticles in the suspension is fixed, different size distributions does not cause notable changes in the critical temperature v.s. magnetic field frequency curve, as shown in Fig. 3(b). When the size distribution is fixed, however, changing the mean diameter of the magnetic nanoparticles significantly changes the critical temperature v.s. magnetic field frequency curve, as shown in Fig. 3(c). A decrease in mean diameter from 25 nm to 16 nm displays a much higher critical frequency requirement to disrupt the aggregates.

Table 3. Physical properties of magnetic materials

Magnetic Solid	Chemical Formula	$M_d(kA \cdot m^{-1})$	$K(kJ \cdot m^{-3})$	$c(J \cdot kg^{-1} \cdot K^{-1})$	$\rho(kg \cdot m^{-3})$
Maghemite	$\gamma - Fe_2O_3$	414	15	746	4600
Magnetite	$FeO \cdot Fe_2O_3$	446	23	670	5180
Cobalt Ferrite	$CoO \cdot Fe_2O_3$	425	180	700	4907
Barium Ferrite	$BaO \cdot 6Fe_2O_3$	380	300	650	5280

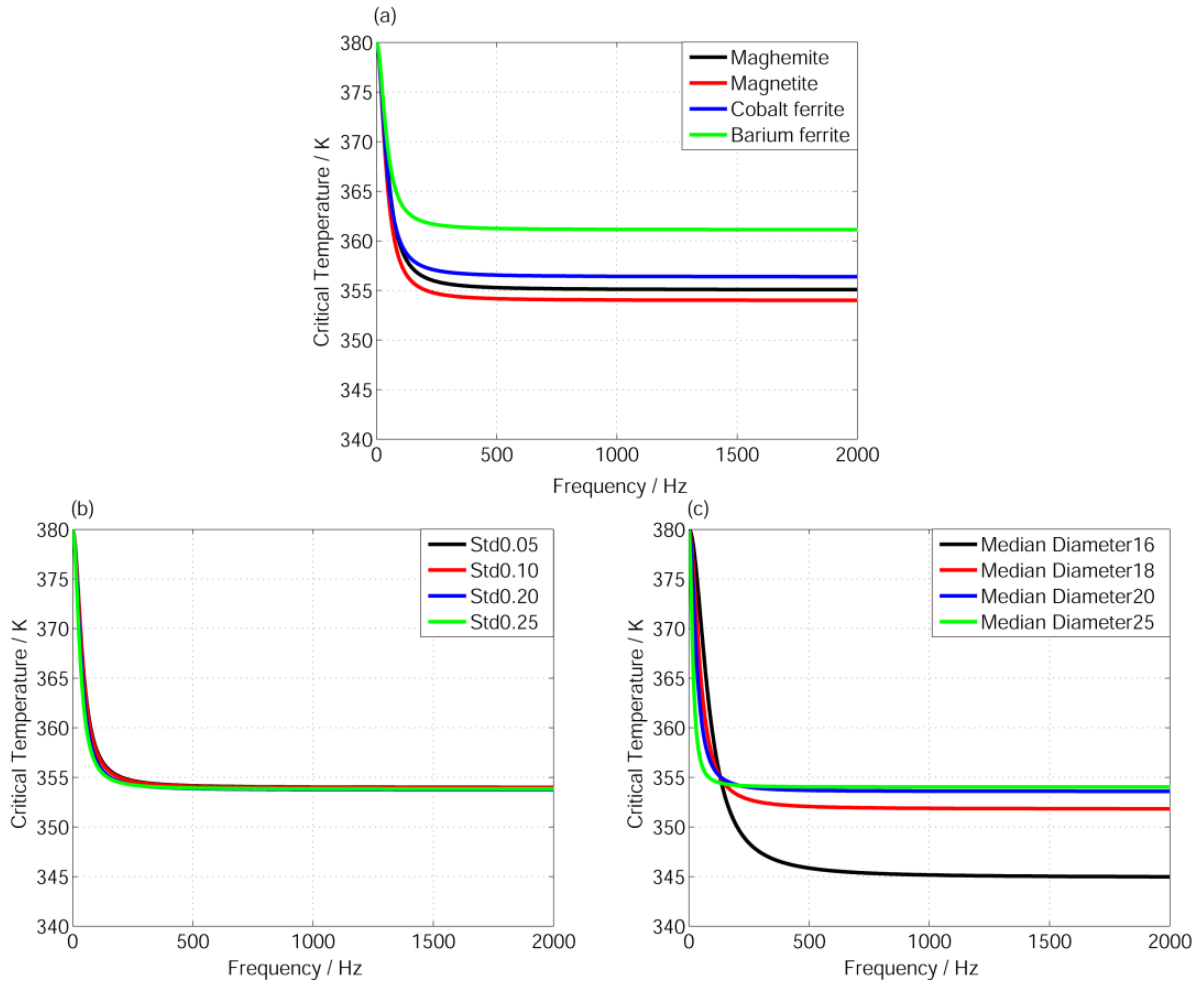

Figure 3. The critical temperature for cluster disruption of magnetic nanoparticle suspension as a function of external magnetic field frequency. (a) The critical temperature for cluster disruption of different magnetic nanoparticle suspension versus external magnetic field frequency. (b) The critical temperature for cluster disruption of magnetite versus external magnetic field frequency under different size distribution (same median diameter $\overline{D} = 20.00\,nm$, the standard deviations shown in the figure are all in the unit of nm). (c) The critical temperature for cluster disruption of magnetite versus external magnetic field frequency under different median diameter (same size distribution $\sigma = 0.25\,nm$).

9.5 Conclusion

Magnetic nanoparticles have found popular applications as "molecular beacons" for medical diagnosis and as "molecular bullets" for targeted therapy. Consequently, the sensitive detection [16-18] and effective heating of magnetic nanoparticles are fundamental to the development of magnetic resonance molecular imaging and nanomedicine. For nanomedical, theranostic applications of magnetic resonance hyperthermia in cellular environments, the interactions between the nanoparticles with the other nanoparticles and with surrounding biomolecules such as proteins, lipids and sugars (all of which could be electrically charged) and small ions (cations and anions) could be significant and generally discount the heating efficiency [19].

As a first step in optimizing the hyperthermia effect, the thermodynamic behavior of magnetic nanoparticles and aggregation dynamics were studied in this work. 3D cluster-moving-based Monte Carlo method was used to simulate the thermodynamic behavior of the magnetic nanoparticles and to further analyze the monomer/aggregate distribution at various temperatures. Simulation results show that the relative content of aggregates decreases with the increase of temperature, until all the particles exist as monomers at or above the critical temperature. The critical temperature is further found to be related to the frequency of the external alternating magnetic field, where the critical temperature continually decreases with the increase of frequency until the critical frequency is reached. Any increase of frequency beyond this point no longer affects the critical temperature. Our simulation suggests that the heating efficiency of magnetic nanoparticle suspension may be optimized for its potential applications in magnetic resonance hyperthermia by preheating the colloidal suspension at the critical frequency to disrupt aggregates into monomers.

9.6 References

[1] Jordan A, Wust P, Fähling H, *et al*. Inductive Heating of Ferrimagnetic Particles and Magnetic Fluids: Physical Evaluation of Their Potential for Hyperthermia. Int J Hyperthermia, 2009, 25: 499-511.

[2] Krishnan K M. Biomedical Nanomagnetics: A Spin Through Possibilities in Imaging, Diagnostics, and Therapy. IEEE Trans Magn, 2010, 46: 2523-2558.

[3] Gordon R T, Hines J R, Gordon D A. Biophysical Approach to Cancer Treatment via Intracellular Temperature and Biophysical Alterations. Medical Hypotheses, 1979, 5: 83-102.

[4] Jordan A, Wust P, Scholz R, *et al*. Cellular Uptake of Magnetic Fluid Particles and Their Effects on Human Adenocarcinoma Cells Exposed to AC Magnetic Fields In Vitro. Int J Hyperthermia, 1996, 12: 705-722.

[5] Alexey O I, Sofia S K, Valentin S M, *et al*. Ferrofluid aggregation in chains under the influence of a magnetic field. J Magn Magn Mater, 2006, 300(l): e206-e209.

[6] Morais P C, Gonçalves G R R, Bakuzis A F, *et al*. Experimental Evidence of Dimer Disruption in ionic Ferrofluid: A Ferromagnetic Resonance Investigation. J Magn Magn Mater, 2001, 225: 84-88.

[7] Zhong J, Xiang Q, Massa L O, *et al*. Second-Order-Like Cluster-Monomer Transition Within Magnetic Fluids and its Impact Upon the Magnetic Susceptibility. Nanoscale Res Lett, 2012, 7: 167.

[8] Du Z, Liu W, Zhong J, *et al*. Signature of cluster disruption within magnetic fluid samples: The key information provided by low frequency alternating current susceptibility measurements. J Appl Phys, 2014, 115: 194310.

[9] Ganguly R, Zellmer B, Puri I K. Field-Induced Self-Assembled Ferrofluid Aggregation in

Pulsatile Flow. Phys Fluids, 2005, 17: 097104.

[10] Xiang Q, Zhong J, Zhou M, *et al*. AC field dependence of cluster disruption in magnetic fluids. J Appl Phys, 2011, 109: 07B317.

[11] Wang X, Gu H, Yang Z. The heating effect of magnetic fluids in an alternating magnetic field. J Magn Magn Mater, 2005, 293: 334.

[12] Rosensweig R E. Heating magnetic fluid with alternating magnetic field. J Magn Magn Mater, 2002, 252: 370.

[13] Ondeck C L, Habib A H, Ohodnicki P, *et al*. Theory of magnetic fluid heating with an alternating magnetic field with temperature dependent materials properties for self-regulated heating. J Appl Phys, 2009, 105: 07B324.

[14] Skumiel A, Łabowski M. The Heating Effect of the Biocompatible Ferrofluid in an Alternating Magnetic Field. Molecular and Quantum Acoustics, 2006, 27: 233-238.

[15] Chantrell R W, Popplewell J, Charles S W. Measurements of particle-size distribution parameters in ferrofluids. IEEE Trans Magn, 1978, 14 (5): 975-977.

[16] Hwang D W, Lin Y.-Y., Hwang L.-P. Studies of magnetic resonance imaging with active feedback RF field. Chinese J Magn Reson, 2010, 27 (3): 409-416.

[17] Huang S Y, Walls J D, Lin Y.-Y. Periodic control of spin turbulence in solution magnetic resonance. Chinese J Magn Reson, 2010, 27 (3): 425-435.

[18] Li Z, Hsu C.-H., Dimitrov N, Hwang D W, Chang H.-W., Hwang L.-P., Lin Y.-Y. Sensitive imaging of magnetic nanoparticles for cancer detection by active feedback MR. Magn Reson Med, 2015, DOI: 10.1002/mrm.25632.

[19] Hilger I, Kaiser W A. Iron oxide-based nanostructures for MRI and magnetic hyperthermia. Nanomedicine 2012, 7(9): 1443–1459.

Chapter 10

MR Theranostic Hyperthermia: Optimizing Specific Loss Power and Heating Efficiency

10.0 Abstract

Magnetic fluid hyperthermia has been a recent field of investigation for its ability to generate heat by the Specific Loss Power (SLP) produced when magnetic nanoparticles are placed in an alternating magnetic field. Previous studies have assumed magnetic nanoparticles act as singular units, and have designed theoretical models reflecting this characteristic. In reality, magnetic fluids are a colloidal-based system containing varying amounts of nanoparticle aggregates, which in turn, experimentally affects the magnitude of heat generated. In this chapter, we focus on establishing a model to describe the colloidal-based magnetic fluid by considering aggregation effects, which would greatly reduce the heating efficiency of the magnetic fluid. We then compare our cluster-based model with the currently prevailing model published by Rosensweig, which are then compared to experimental results, and concluded that aggregation consideration in theoretical models provided a more accurate estimation framework for experimental results. Additionally, magnetic nanoparticles within the size range of 9nm-14nm were best predicted with our proposed cluster-based model. Overall, our proposed cluster-based model predicts that the ideal magnetic particle size for maximal magnetic fluid heating efficiency to be 20% smaller than predicted by previous models.

10.1 Introduction

Magnetic fluid hyperthermia (MFH) has been widely investigated field for the last decade, particularly for its potential applications in cancer treatment [1, 2]. A number of studies have shown that these magnetic fluids, or magnetic nanoparticle (MNP) suspensions, are able to release heat through relaxation mechanisms when exposed to a relatively weak alternating magnetic field (AMF) [1, 3, 4]. This selective heating can be used to target cancer tissue, as these abnormal growths are more susceptible to cell death under elevated temperatures [5]. However, further applications of MFH is constrained to the limited availability of accurate prediction models for evaluating the heating efficiency and heating capacity of the ferrofluid.

To look at these heating properties, the specific loss power (SLP) lays a constructive platform for calculating the heat generation per mass unit of dissipating material. Experimentally, heat generated by SLP is shown to be dependent on magnetic fluid and MNP properties, specifically the mean particle size and size distribution, as well as the frequency of the AMF [6, 7, 8]. Reaching a therapeutic temperature for cancer treatment while administering minimal manipulating MNP size and in turn, altering the SLP produced.

Problematically, traditional models for estimating SLP do not accurately predict reported experimental data [9, 10, 11]. This limitation can be accounted for by analyzing the ferrofluid composition and structure. The original model proposed by Rosensweig [12] assumes MNPs act independently of one another in suspension. Morais *et al.* [13] and Castro *et al.* [14] found MNPs form clusters when in solution, where Ganguly *et al.* [15] reported individual particles formed interactions, including electrostatic attraction, electrostatic repulsion, steric repulsion, and magnetic dipolar interactions. Interestingly, several groups have determined cluster formation

does not depend on the solution composition, as MNPs were found to form aggregates in similar magnitudes when suspended in either water or glycerol [16-19].

Furthermore, magnetic fluid characteristics and structures differ under varying AMF strengths, such that the relative content of agglomerates changes the magnetization and susceptibility of the ferrofluid [20, 21]. Thus, we aim to propose a revised model for estimating the SLP by considering particle aggregation to mediate the existing discrepancy between the current theoretical and experimental results.

Under an AMF, magnetic susceptibility is dependent on temperature, where the Langevin function is used to describe the linear relationship between temperature and the inverse of magnetic susceptibility. According to a publication by Zhong *et al.* [22] the relative quantities of monomeric and clustered particles in the ferrofluid are characterized by a critical temperature. This critical temperature describes the temperature at which MNP clusters dissociate into individual units completely.

To account for a dependence on this critical temperature, we propose a modified Langevin function to redefine the magnetic susceptibility of the ferrofluid, as well as develop an alternative SLP model based upon this revised function. The proposed models will account for cluster formation and size distribution of the MNPs. These theoretical models will then be compared to experimental data and results previously published [6, 23, 24] in hopes of providing an accurate model for predicting SLP. Not only do we aim to provide the groundwork for predicting the heating efficiency and heating capacity of magnetically induced hyperthermia, but also to design a model describing a temperature dependent function of nanoparticle size in heat generation for future applications of MFH in cancer therapy.

10.2 Theory

10.2.1 Relaxation

To calculate the SLP value of colloidal MNP as an interacting system in ferrofluids, we first need to describe two relaxation mechanisms [28] of MNP fluctuation dispersed in a fluid. The first relaxation, referred to as the Brown relaxation, and derived by Deby [29], assumes the dipole of the MNP is fixed in the easy axis of the magnetic crystal, thus is known as the rigid dipole model. To look at this relaxation mechanism, the whole particle is said to rotate towards the external field mechanically under the thermal effect against the viscous drag in the suspending medium. This viscosity coefficient of the ferrofluid solution carrier is described by the constant η, and is temperature dependent. The solution carrier was designated as water, assuming the ferrofluid aggregation does not depend on the suspending solution [16-19]. Thus, the Brown relaxation time, τ_B, can be expressed as:

$$\tau_B = \frac{3\eta V_h}{k_B T} \tag{1}$$

where the particle's hydrodynamic volume is described as $V_h = (1 + \delta/R)^3 V$, and V is the volume of the particle. k_B represents the Boltzman constant, and R the radius of the nanoparticle. The surfactant thickness is represented as δ, and is a property of the ferrofluid.

The second relaxation mechanism, known as the Néel relaxation [30], describes a particle that cannot release energy through particle reorientation. Because the magnetic moment rotates away from the easy axis towards the external field, the mechanism is known as the soft dipole approximation. The Néel relaxation time, τ_N, is expressed as:

$$\tau_N = \begin{cases} \tau_0 \Gamma^{-\frac{1}{2}} exp\Gamma & \Gamma \geq 1 \\ \tau_0 \Gamma & \Gamma \ll 1 \end{cases} \tag{2}$$

in which $\Gamma = \frac{K_a V}{k_B T}$. Here K_a represents the anisotropy constant. In our proposed model, K_a for a ferrofluid that forms clusters can be derived using the relative contents of monomers and clusters, denoted as P_m and P_c respectively:

$$P_m = \frac{T}{T^*} \tag{3a}$$

$$P_c = (1 - \frac{T}{T^*})^{\frac{1}{2}} \tag{3b}$$

T describes the temperature of the solution, while T^* is the transition temperature at which all clusters would disrupt into monomers, and can be altered by the external parameters of frequency, and concentration of the ferrofluid. For example, if $T = T^*$, then all MNPs would be present in monomers.

If the anisotropy constant for monomers is written as $K_{am} = K_a$, then the anisotropy constant for clusters, K_{ac}, can be expressed as:

$$K_{ac} = \frac{(1-P_m)K_a}{P_c} \tag{4}$$

Because both relaxation mechanisms will occur simultaneously in the ferrofluid [12], the effective relaxation time is given as:

$$\tau = \frac{1}{\tau_B} + \frac{1}{\tau_N} \tag{5a}$$

or alternatively as:

$$\tau = \frac{\tau_B \cdot \tau_N}{\tau_B + \tau_N} \tag{5b}$$

When $\tau_B \ll \tau_N$, then $\tau \approx \tau_B$. Likewise, when $\tau_B \gg \tau_N$, then $\tau \approx \tau_N$. Hence the effective relaxation time depends on the stronger relaxation mechanism, and can be written in the decay form when the two mechanisms are co-occuring.

10.2.2 Magnetization

Because MNPs directly influence the ferrofluid parameters, we investigated the effects of cluster formation on magnetization and magnetic susceptibility of the ferrofluid. Rigorously derived by Xiang *et al.* [31], the magnetization of a ferrofluid, $M(T)$, where monomers and multimers depend on temperature, can be rewritten as:

$$M(T) = \phi \left[M_{dm} \left(\frac{T}{T^*} \right) L \left(\frac{\mu_0 m H_0}{k_B T} \right) + M_{dc} (1 - \frac{T}{T^*})^{\frac{1}{2}} L(\frac{\mu_0 \overline{m_c} H_0}{k_B T}) \right] \quad (6)$$

The volume fraction of MNP is given by ϕ and is canceled out when calculating SLP shown below. The magnetic permeability is given as the constant μ_0. Here, the single-domain magnetization of monomeric suspended particles is represented as $M_{dm} = M_d$. Using the reduced anisotropy constant K_{ac} from equation (4), the magnetization of clusters M_{dc} is expressed as:

$$M_{dc} = \frac{(1-P_m)M_d}{P_c} \quad (7a)$$

Substituting in equations (3a) and (3b), we obtain the final cluster magnetization expression:

$$M_{dc} = (1 - \frac{T}{T^*})^{\frac{1}{2}} M_d \quad (7b)$$

Because MNP clusters exhibit a reduced anisotropy constant, the magnetization for clusters is also reduced.

In our revised model, the magnetism of the single domain monomeric particles is related to the corresponding average magnetic moment of different monomers by $m = VM_d$. Likewise, clusters would be related to the average magnetic momentum of other clusters by:

$$\overline{m_c} = \frac{(1-P_m)VM_d}{P_c} \quad (8a)$$

Again, substituting in equations (3a) and (3b), we obtain the final expression for the average magnetic momentum between individual clusters:

$$\overline{m_c} = (1 - \frac{T}{T^*})^{\frac{1}{2}} V M_d \tag{8b}$$

Finally, equations (8a) and (8b) are used to derive a new Langevin function. For single monomeric particles, the average magnetic momentum of singular units would expressed as:

$$L\left(\frac{\mu_0 m H_0}{k_B T}\right) = \coth\left(\frac{\mu_0 m H_0}{k_B T}\right) - \frac{k_B T}{\mu_0 m H_0} \tag{9a}$$

To account for cluster formation, the additional Langevin function would use the average magnetic momentum between clusters calculated in equation (8b), and would similarly be expressed as:

$$L\left(\frac{\mu_0 \overline{m_c} H_0}{k_B T}\right) = \coth\left(\frac{\mu_0 \overline{m_c} H_0}{k_B T}\right) - \frac{k_B T}{\mu_0 \overline{m_c} H_0} \tag{9b}$$

All in all, the cluster-based model takes into account the formation of MNP aggregates to produce the corrected expression for the actual magnetization effect using a revised Langevin function.

10.2.3 Magnetic susceptibility

Using this expression for the magnetization of the ferrofluid, the corresponding equilibrium magnetic susceptibility, $\chi(T)$, is given as:

$$\chi(T) = \frac{M(T)}{H_0} \tag{10a}$$

Substituting equation (6) into (10a) gives the expression:

$$\chi(T) = \frac{\phi}{H_0}\left[M_{dm}\left(\frac{T}{T^*}\right) L\left(\frac{\mu_0 m H_0}{k_B T}\right) + M_{dc}(1 - \frac{T}{T^*})^{\frac{1}{2}} L(\frac{\mu_0 \overline{m_c} H_0}{k_B T})\right] \tag{10b}$$

As derived by the Shilomis relaxation equations [12], when an AMF current is applied to the ferrofluid, the magnetization can be expressed as:

$$\frac{\partial M(t)}{\partial \mathrm{t}} = \frac{1}{\tau}(M_0(t) - M(t)) \tag{11}$$

Thus, using the equilibrium magnetic susceptibility (10b), the equilibrium magnetization $M_0(t)$ under the alternating magnetic field can be expressed as:

$$M_0(t) = \chi(T)H_0 cos\omega t = Re[\chi(T)H_0 e^{i\omega t}] \tag{12}$$

where $\omega = 2\pi f$ is the angular frequency of the AMF and f is the frequency of the magnetic field. The final expression for both the real and imaginary portions of the equilibrium susceptibility can then be respectively written as:

$$\chi' = \frac{\chi(T)}{1+(\omega\tau)^2} \tag{13a}$$

$$\chi'' = \frac{\omega\tau\chi(T)}{1+(\omega\tau)^2} \tag{13b}$$

and total equilibrium susceptibility as:

$$\chi\,(\mathrm{T}) = \chi' + \chi'' \tag{13c}$$

10.2.4 Power dissipation

Using the derived equilibrium magnetization and magnetic susceptibility, we can now calculate the adjusted power dissipation. For magnetic particles suspended in an AC field, the power dissipation is equal to the change in internal energy, ΔU, or equivalently, the loss of magnetic work [12]:

$$\Delta U = -\mu_0 \oint M(t)dH \tag{14a}$$

$$\Delta U = -\mu_0 \oint_0^{\frac{2\pi}{\omega}} Re\left[\chi H_0 e^{-i\omega t}\right]dH \tag{14b}$$

$$\Delta U = \mu_0 \pi {H_0}^2 \chi'' \tag{14c}$$

Substituting in equation (13b) and $\omega = 2\pi f$, we get the final expression for the loss of magnetic work:

$$\Delta U = \frac{2\mu_0 {H_0}^2 f\pi^2 \tau\chi(T)}{1+(2\pi f\tau)^2} \tag{14d}$$

Using the change in internal energy, the volumetric power dissipation P can be expressed as:

$$P = f\Delta U \tag{15a}$$

Substituting in equation (14c):

$$P = \mu_0 \pi f {H_0}^2 \chi'' \tag{15b}$$

the derived complex part of the equilibrium magnetic susceptibility in equation (18c), we can express P as:

$$P = \frac{2\mu_0 {H_0}^2 (f\pi)^2 \tau \chi(T)}{1+(2\pi f\tau)^2} \tag{15c}$$

Finally, to obtain the modified power dissipation for cluster formation, substitute equation (6) for χ (T), in equation (15c):

$$P = \frac{2\mu_0 {H_0}^2 (f\pi)^2 \tau \chi(T) \phi}{1+(2\pi f\tau)^2} \left[M_{dm} \left(\frac{T}{T^*}\right) L\left(\frac{\mu_0 m H_0}{k_B T}\right) + M_{dc}(1 - \frac{T}{T^*})^{\frac{1}{2}} L(\frac{\mu_0 \overline{m_c} H_0}{k_B T}) \right] \tag{15d}$$

10.2.5 Specific Loss Power (SLP)

SLP can be calculated as:

$$SLP = \frac{P}{\rho \phi} \tag{16a}$$

where ρ represents the density of the ferrofluid. The corresponding adjusted SLP accounting for cluster formation in the ferrofluid would be expressed as:

$$SLP = \frac{2\mu_0 \tau H_0 (\pi f)^2}{\rho[1+(2\pi f\tau)^2]} \left[M_{dm} \left(\frac{T}{T^*}\right) L\left(\frac{\mu_0 m H_0}{k_B T}\right) + M_{dc}(1 - \frac{T}{T^*})^{\frac{1}{2}} L(\frac{\mu_0 \overline{m_c} H_0}{k_B T}) \right] \tag{16b}$$

10.3 Methods

To determine the accuracy of our revised model, predicted values were compared to previously published data. Using the magnetic iron oxide nanoparticles, γ-Fe_2O_3 (maghemite),

computational parameters were set up to match the corresponding results from experiments. Specific ferrofluid constants used in all models include the magnetization $m_s = 2.8\,x\,10^5\,Am^{-1}$ and density $\rho = 4.9\,x\,10^3\,kgm^{-3}$. The carrier solvent water has a viscosity coefficient $\eta = 0.7x10^3\,PI$. Matlab was used to compute all simulations and figures.

10.3.1 Modeling Comparisons

The first computational model mainly looked at the differences between the original Rosensweig model and our cluster-based model using parameters published by Hergt *et al*. [6]. To look at the imaginary portion of equilibrium susceptibility as a function of frequency, the mean MNP core diameter was set to 18nm and the hydrodynamic diameter three times the core diameter.

Both the imaginary portion of the equilibrium susceptibility and SLP was calculated as a function of MNP diameter with a fixed field magnetization strength of f = 410 *kA/m* and field amplitude of H_0 = 11 *kA/m*. The surfactant thickness δ=3, so that the hydrodynamic volume V_h was three times that of the volume of the MNP.

10.3.2 Experimental Comparisons.

The experimental results published by Khandhar *et al*. [23] was then used as a reference point to compare how each model approached real data. Data regarding the MNP size and corresponding SLP reported is summarized in Table 1. Again, the magnetic field strength was set to f = 410 *kA/m* and field amplitude of H_0 = 11 *kA/m* to produce the theoretical models. The anisotropy energy density was set to K_a = 16*kJm*, and surfactant thickness δ=0, so that the hydrodynamic volume V_h is the same as the MNP volume.

Table 1. Experimental results reported by Khandhar *et al.* [23], used as a reference for comparing theoretical models depicted in Fig. 2.

Sample		1	2	3	4	5
Particle Size	Diameter (nm)	5.3	6.7	8.0	10.2	16.5
	σ	0.19	0.20	0.21	0.28	0.43
SLP (W/g)		4	14	37	275	1650

Lastly, the experimental results published by Gonzales-Weimuller *et al.* [24] were then used for a second comparison for both theoretical models. Data regarding MNP size and corresponding SLP reported is summarized in Table 2. The magnetic field strength was set to f = 700 kA/m and field amplitude of H_0 = 24.811 kA/m. The anisotropy energy density was set to K_a = 16 kJ/m, and surfactant thickness δ=0, so that the hydrodynamic volume V_h is the same as the MNP volume.

Table 2. Experimental data reported by Gonzales-Weimuller *et al.* [24] were used as a reference to compare how each theoretical model approached experimental results.

Sample		1	2	3	4
Particle Size	Diameter (nm)	4.6	8.5	11.2	9.6
	σ	0.075	0.15	0.21	0.22
SLP (W/g)		180	130	447	200

10.4 Results and Discussion

10.4.1 Cluster-Based Modeling

To verify the prediction accuracy of the proposed cluster-based model in contrast to the original Rosensweig model [12], we computed SLP values from both models, then compared them to existing experimental data [6,23,24]. Each computation setup used the corresponding experimental parameters to eliminate potential variables for the purpose of comparison. We

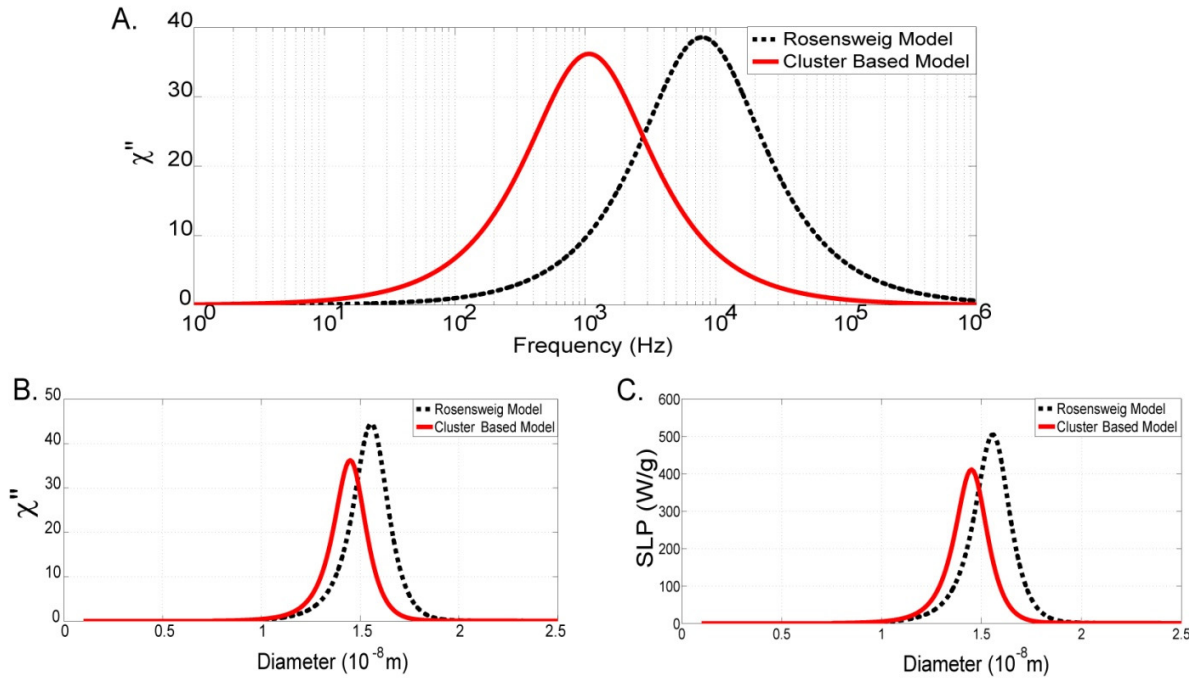

Figure 1. SLP was recalculated with the parameters reported by Hergt *et al.* [6] using the Rosenweig model and the proposed cluster-based model. The imaginary part of the magnetic susceptibility was plotted as a function of frequency with a magnetic nanoparticle size of 18nm (A). The imaginary part of the magnetic susceptibility was then calculated as a function of MNP diameter, with magnetic field strength of 410 *kA/m,* magnetic field amplitude of *11kA/m*, and anisotropy constant 15 kJ/m^3(B). The resulting SLP was then computed as a function of MNP diameter (C) using the same conditions as part (B).

mainly focused on the magnetic iron oxide nanoparticle γ-Fe_2O_3 (maghemite), as it is well tolerated by the human body in comparison to other MNPs [25,26,27].

We first looked at how the aggregation behavior of interacting MNPs affects the prediction of SLP values. Because SLP is proportional to the power dissipation, which is in part determined by the imaginary part of the magnetic susceptibility as described in equation (15b), changes in the imaginary part of magnetic susceptibility due to the ferrofluids behavior would be reflected on the resulting SLP. Experimental results reported by Hergt *et al.* [6] regarding the relationship between the frequency and imaginary part of the magnetic susceptibility of the ferrofluid, were shown to be significantly different from the predicted Rosensweig theoretical values. Specifically, experimental results for the colloidal-based ferrofluid suspension were shown to have a lower susceptibility peak value than predicted, implying the model suggested by Rosensweig alone cannot fully characterize the ferrofluid system. Our proposed model aimed to explain the inconsistency between this original prediction and experimental results by considering cluster formation in the ferrofluid solution.

Using the parameters outlined in the methods section, we compared the differences between the Rosensweig model and the proposed cluster-based model. The imaginary part of magnetic susceptibility was calculated as a function of the magnetic field frequency, depicted in Fig. 1A. Furthermore, the imaginary part of the colloidal-based ferrofluid susceptibility, Fig. 1B, varied as a function of the magnetic nanoparticle core diameter. As a result, calculations based on the proposed cluster consideration shifted the SLP curve to the left, as well as decreased the maximum SLP value. Taking ferrofluid agglomeration into account reduced the overall magnetic anisotropy described by equation (4), as well as reduced the value of both magnetization and average magnetic momentum given by equations (7b) and (8b), respectively. Particularly, the

decrease in magnetic anisotropy is reflected in the relaxation time, where the decrease in magnetization and average magnetic momentum is reflected in the equilibrium magnetic susceptibility, which altogether contributed to the shift of the original prediction for the SLP curve.

The SLP was also plotted as a function of the MNP mean core diameter using the same parameters, which revealed that the predicted SLP values reflected the variation in imaginary part of magnetic susceptibility, as these two functions are shown to be linearly related.

The main difference between these two models is the consideration of MNP interactions within the real ferrofluid. Because the Rosensweig model assumes MNPs act as individual units independent of each other, the SLP value, as well as the optimal MNP size, is estimated to have a higher value. In reality, however, MNPs are not found simply in singular units, but rather as aggregated clusters. As a result, predictions of SLP values were reduced for the corresponding optimal MNP size estimations. Theoretical models should therefore reflect the relative content of clusters in the real ferrofluid. By taking cluster formation into consideration, our proposed model predicted SLP values, and corresponding optimal MNP size at the maximum SLP, to be 20% smaller than those made by the previous model.

10.4.2 Experimental Comparison

The predictions calculated from both models were then compared to experimental data to show how these theoretical predictions approach reported results, described in Fig. 2. Though there are still some differences between our cluster-based prediction and experimental data, our model offers relatively more accurate theoretical values for estimating the SLP in comparison to the Rosensweig model (Fig. 2A). Each theoretical function for predicting the values for the SLP

as a function of MNP size were plotted using the corresponding experimental condition to see how each model approached the experimental result (Figures 2B-F). Where individual comparisons differed only in the mean MNP core diameter size and standard deviation, each theoretical SLP prediction showed similar functional trends. Within the superparamagnetic range, SLP values of all samples elevate significantly with the increase of particle size, as other heat generation mechanisms become more influential. However, the presence of aggregates in the ferrofluid shifted the overall curve to the left, predicting a relatively lower SLP value when

compared to predictions made by the Rosenswig model, consistent with the predicted modeling differences described in Fig. 1. The cluster-based model is most accurately able to predict sample 4 in particular, which has a mean core diameter 10.2nm and standard deviation of 0.28nm. In contrast, neither theoretical model accurately predicted the SLP for sample 5, which has a mean core diameter of 16.5nm and standard deviation of 0.43nm. This divergence is most likely due to the availability of other heat generation mechanisms, such as hysteresis [8,18], with the larger MNP size. Notably, MNPs within the size range of 9nm-14nm are predicted best with the

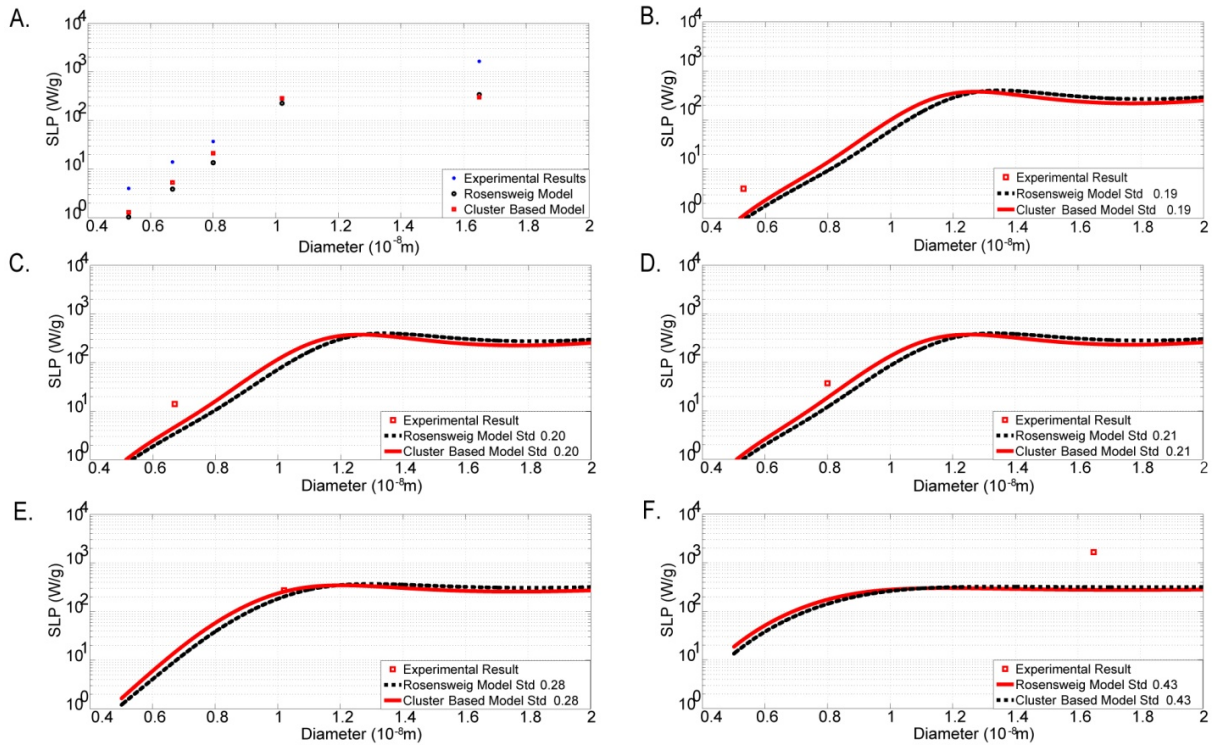

Figure 2. Theoretical comparisons between the Rosensweig model and cluster-based model. Magnetic field strength was set to 410 *kA/m*, amplitude 11*kA/m*, and anisotropy energy density to 16 kJ/m^3. Computational calculations of both models used the corresponding experimental parameters, and were then compared to experimental results (A), published by Khandhar *et al.*[23] summarized in Table 1. Each experimental value was then used as a reference point to assess how each model approached the experimental result (B-F).

cluster-based model. This shift in theoretical values produce a better estimation that fits more accurately with experimental data.

Additional comparisons of the two models were made using the experimental parameters and data reported by Gonzales-Weimuller *et al.* [24] were summarized in Table 2 and shown in Fig. 3A. Individual analyses of the theoretical SLP functions approaching experimental results are shown in Figures 3B-E. Similar to the previous comparison, the proposed cluster-based model approaches experimental results closer than the original model. SLP of MNPs with a diameter between 9nm-14nm were more accurately predicted by the proposed model in comparison to other sizes of MNPs.

The increased aggregation of MNPs changes the structure of the magnetic fluid, decreasing magnetic anisotropy, magnetization, and the average magnetic momentum, which in turn, contributes to the decrease of the overall values in the imaginary part of susceptibility. Physically, a portion of the energy provided by the magnetic field is absorbed by the particle aggregates to overcome interactions, such as electrostatic attraction, electrostatic repulsion, steric repulsion, and magnetic dipolar interactions, to disrupt the agglomerates into monomers. As a result, the heating efficiency is decreased, and SLP values are less than the predicted value based on the original theory.

Moreover, predicting the amount of heat generated with increasing particle size becomes more difficult, as alternative heat releasing mechanisms become available. Consequently, a relatively smaller particle size should be chosen to reach the same heating efficiency, as the SLP produced by smaller MNPs are better predicted by the cluster-based model.

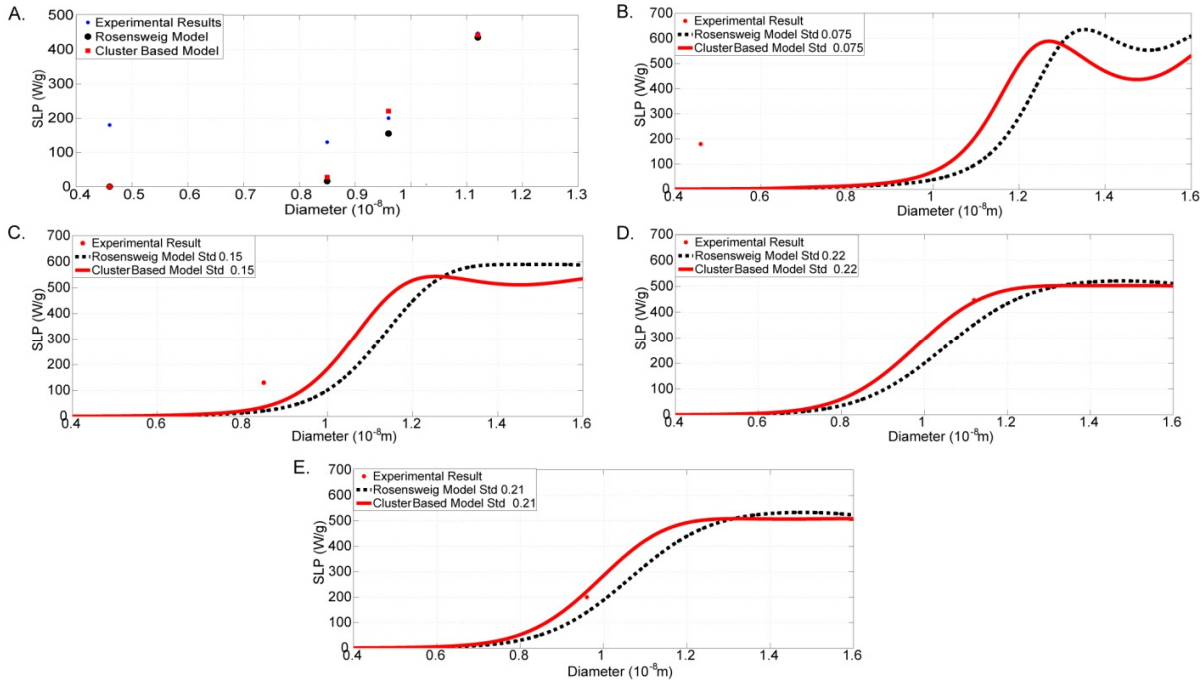

Figure 3. Additional theoretical comparisons between the Rosensweig model and cluster-based model. Similar to the previous models, magnetic field strength was set to 410 *kA/m*, amplitude 11*kA/m*, and anisotropy energy density to 16 kJ/m^3. Applying parameters published by Gonzales-Weimuller *et al.* [24] (summarized in Table 2), experimental data was compared to both theoretical models (A). Each model model was then shown to approach experimental values (B-E) to analyze the prediction accuracy of SLP as a function of MNP diameter.

10.5 Conclusion

By considering the effects of particle aggregation on SLP in a magnetic fluid system, our proposed cluster-based model provides a more accurate prediction of experimental values, particularly within a MNP size range of approximately 9nm-14nm, as shown in Figure 2E and Figure 3D. Smaller particles do not offer effective heating efficiency, as they generate small SLP values. Likewise, although larger particles may produce higher rates of heating, the heat generating mechanism is ambiguous, where relaxation, hysteresis, or both mechanisms, may occur. The presence of multiple heating mechanisms would require a more complicated prediction model, making accurate theoretical assessments difficult.

In terms of potential cancer treatment uses, optimal MNP size should produce sufficient heat, while still being describable by theoretical representations. This proposed cluster-based model offers a theoretical method for approximating the amount of heat that can be generated by MNPs for potential MFH uses in cancer therapy.

10.6 References

[1] Jordan, A.; Wust, P.; Fähling, H.; John, W.; Hinz, A.; Felix, R. Inductive Heating of Ferrimagnetic Particles and Magnetic Fluids: Physical Evaluation of Their Potential for Hyperthermia.*Int. J. Hyperthermia*. **2009**, *25*, 499-511.

[2] Krishnan, K. M. Biomedical Nanomagnetics: A *Spin* Through Possibilities in Imaging, Diagnostics, and Therapy. *IEEE Trans Magn*. **2010**, *46*, 2523-2558.

[3] Gordon, R.T.; Hines, J.R.; Gordon, D. A Biophysical Approach to Cancer Treatment via Intracellular Temperature and Biophysical Alterations. *Medical Hypotheses*. **1979**, *5*, 83-102.

[4] Jordan, A.; Wust, P.; Scholz, R.; Tesche, B.; Fähling, H.; Mitrovics, T.; Vogl, T.; Cervós-avarro, J.; Felix, R. Cellular Uptake of Magnetic Fluid Particles and Their Effects on Human Adenocarcinoma Cells Exposed to AC Magnetic Fields *In Vitro*. *Int. J. Hyperthermia*. **1996**, *12*, 705-722.

[5] Wada, S.; Yue, L.; Tazawa, K.; Furuta, I.; Nagae, H.; Takemori, S.; Minamimura, T. New Local Hyperthermia Using Dextran Magnetite Complex (DM) for Oral Cavity; Experimental Study in Normal Hamster Tongue. *Oral Diseases*. **2001**, *7*, 192-195.

[6] Hergt, R.; Dutz, S.; Müller, R.; Zeizberger, M. Magnetic Particle Hyperthermia: Nanoparticle Magnetism and Materials Development for Cancer Therapy. *J. Phys.: Condens. Matter*. **2006**, *18*, 2919-2934.

[7] Hergt, R.; Andrä, W. Biomagnetic Instrumentation. In *Magnetism in Medicine: A Handbook*; Andrä, W., Nowak, H., Eds.; Wiley-VCH Verlag GmbH & Co. KgaA: Weinheim, 2007; pp 550.

[8] Hergt, R.; Dutz, S.; Röder, M. Effects of Size Distribution on Hysteresis Losses of Magnetic Nanoparticles for Hyperthermia. *J. Phys.: Condens. Matter*. **2008**, *20*, 385214.

[9] Bordelon, D.E.; Cornejo, C.; Grüttner, C.; Westphal, F.; DeWeese, T.L.; Ivkov, R. Magnetic Nanoparticle Heating Efficiency Reveals Magneto-Structural Differences When Characterized with Wide Ranging and High Amplitude Alternating Magnetic Fields. *Journal of Applied Physics*. **2011**, *109*, 124904.

[10] Li, Z.; Kawashita, M.; Araki, N.; Mistumori, M.; Hiraoka, M. Effects of Particle Size of Magnetite Nanoparticles on Heat Generating Ability Under Alternating Magnetic Field. *Bioceramics Development and Application.*, **2011**, *1*, D110128.

[11] Khandhar, A. P.; Ferguson, R. M.; Simon, J. A.; Krishnan, K. M. Enhancing Cancer Therapeutics Using Size-Optimized Magnetic Fluid Hyperthermia. *Journal of Applied Physics*. **2012**, *111*, 07B306.

[12] Rosensweig, R.E. Heating Magnetic Fluid with Alternating Magnetic Field. *Journal of Magnetism and Magnetic Materials*. **2002**, *252*, 370-374.

[13] Morais, P.C.; Gonçalves, G.R.R.; Bakuzis, A.F.; Neto, K.S.; Pelegrini, F. Experimental Evidence of Dimer Disruption in ionic Ferrofluid: A Ferromagnetic Resonance Investigation. *Journal of Magnetism and Magnetic Materials*. **2001**, *225*, 84-88.

[14] Castro, L.L.; da Silva, M.F.; Bakuzis, A.F.; Miotto, R. Aggregate Formation on Polydisperse Ferrofluids: A Monte Carlo Analysis. *Journal of Magnetism and Magnetic Materials*. **2005**, *293*, 553-558.

[15] Ganguly, R.; Zellmer, B.; Puri, I.K. Field-Induced Self-Assembled Ferrofluid Aggregation in Pulsatile Flow. *Physics of Fluids*. **2005**, *17*, 097104.

[16] Dennis, C.L.; Jackson, A.J.; Borchers, J.A.; Hoopes, P.J.; Strawbridge, R.; Foreman, A.R.; van Lierop, J.; Grüttner, C.; Ivkov, R. Nearly Complete Regression of Tumors via Collective Behavior of Magnetic Nanoparticles in Hyperthermia. *Nanotechnology*. **2009**, *20*, 395103.

[17] Verde, E.L.; Landi, G.T.; Carrião, M.S.; Drummond, A.L; Gomes, J.A.; Vieira, E.D.; Sousa, M.H.; Bakuzis, A.F. Field Dependent Transition to the Non-Linear Regime in Magnetic Hyperthermia Experiments: Comparison Between Maghemite, Copper, Zinc, Nickel, and Cobalt Ferrite Nanoparticles of Similar Sizes. *AIP Advances*. **2012**, *2*, 032120.

[18] Carrey, J.; Mehdaoui, B.; Respaud, M. Simple Models for Dynamic Hysteresis Loop Calculations of Magnetic Single-Domain Nanoparticles: Application to Magnetic Hyperthermia Optimization. *Journal of Applied Physics*. **2011**, *109*, 083921.

[19] Attaluri, A.; Ma, R.; Qiu, Y.; Li, W.; Zhu, L. Nanoparticle Distribution and Temperature Elevations in Prostatic Tumours in Mice During Magnetic Nanoparticle Hyperthermia. *Int. J. Hyperthermia*. **2011**, *27*, 491-502.

[20] Liu, W.; Zhong, J.; Xiang, Q.; Yang, G.; Zhou, M. Discretization of Magnetization Curves and Their Application in Size Estimation of Nanosized Ferrofluid. *IEEE Transactions on Nanotechnology*. **2011**, *10*, 1231-1237.

[21] Sherman, S.G.; Wereley, N.M. Effect of Paricle Size Distribution on Chain Structures in Magnetoheological Fluids. *IEEE Transactions on Magnetics*. **2013**, *47*, 3430-3433.

[22] Zhong, J.; Xiang, Q.; Massa, L.O.; Qu, F.; Morais, P.C.; Liu, W. Second-Order-Like Cluster-Monomer Transition Within Magnetic Fluids and its Impact Upon the Magnetic Susceptibility. *Nanoscale Research Letters*. **2012**, *7*, 167

[23] Khandhar, A.P.; Ferfuson, R.M.; Simon, J.A.; Krishnan, K.M. Tailored Magnetic Nanoparticles for Optimizing Magnetic Fluid Hyperthermia. *J. Biomed. Mater. Res*. **2012**, *100*, 728-737.

[24] Gonzales-Weimuller, M.; Zeisberger, M.; Krishnan, K.M. Size-Dependant Heating Rates of Iron Oxide Nanoparticles for Magnetic Fluid Hyperthermia. *Journal of Magnetism and Magnetic Materials*. **2009**, *321*, 1947-1950.

[25] Häfeli, U.O.; Riffle, J.S.; Harris-Shekhawat, L.; Carmichael-Baranauskas, A.; Mark, F.; Dailey, J.P.; Bardenstein, D. Cell Uptake and *in Vitro* Toxicity of Magnetic Nanoparticles Suitable for Drug Delivery. *Molecular Pharmaceutics*. **2009**, *6*, 1417-1428.

[26] Gonzales, M.; Mitsumori, L.M.; Kushleika, J.V.; Rosenfeld, M.E.; Krishnan, K.M. Cytotoxicity of Iron Oxide Nanoparticles Made from the Thermal Decomposition of Organometallics and Aqueous Phase Transfer with Pluronic F127. *Contrast Media & Molecular Imaging*. **2010**, *5*, 286-293.

[27] Weissleder, R.; Stark, D.D.; Engelstad, B.L.; Bacon, B.R.; Compton, C.C.; White, D.L.; Jacobs, P.; Lewis, J. Superparamagnetic Iron Oxide: Pharmacokinetics and Toxicity. *AJR*. **1988**, *152*, 167-173.

[28] Skumiel, A.; Łabowski, M. The Heating Effect of the Biocompatible Ferrofluid in an Alternating Magnetic Field. *Molecular and Quantum Acoustice*. **2006**, *27*, 233-238.

[29] Debye, P. Polar Molecules. *The Chemical Catalog Co*. Dover, New York, 1929.

[30] Néel, L. Theorie du trainage magnetique des ferromagnetiques en grains fins avec applications aux terres cuites. *Geophysics*. **1949**, *5*, 99-136.

[31] Xiang, Q.; Zhong, J.; Zhou, M.; Morais, P.C.; Liu, W. AC Field Dependence of Cluster Disruption in Magnetic Fluids. *Journal of Applied Physics*. **2011**, *109*, 07, B317.

[32] Shliomis, M.I.; Stepanov, V.I. Theory of the Dynamic Susceptibility of Magnetic Fluids In *Advances in Chemical Physics*; Coffey, W., Eds.; John Wiley & Sons, Inc: Perm, Russia, 1994.

[33] Wang, X.; Gu, H.; Yang Z. The Heating Effect of Magnetic Fluids in an Alternating Magnetic Field. *Journal of Magnetism and Magnetic Materials*. **2005**, *293*, 334-340.

Chapter 11

Conclusion and Outlook

To achieve early detection and targeted therapy of cancers, integrated, synergistic approaches using "active feedback magnetic resonance" and “supramolecular magnetic nanoparticles” in the framework of magnetic resonance molecular imaging and nano medicine were carried out during my PhD study. The specific aims are to develop “supramolecular magnetic nanoparticles” into powerful (i) “molecular beacons” for early detection of cancers, through sensitive imaging of magnetic nanoparticles; and (ii) “molecular bullets” for targeted therapy of cancers, through electromagnetic hyperthermia induced by coupling magnetic nanoparticles with external alternating magnetic fields and control releasing of cancer drugs.

The research plan had encompassed a balanced approach to develop a rigorous theoretical understanding on sensitively imaging magnetic nanoparticles by active- feedback spin dynamics of selective self-excitation and fixed-point dynamics on one hand and sound methodology with biomedical applicability to early pancreatic cancers and brain tumors detection on the other. Computer simulations, phantom experiments of superparamagnetic nanoparticles, and in vivo experiments of orthotopic pancreatic cancer and brain tumor mouse models had been used to validate the applicability and efficacy of our proposed methods.

In vivo magnetic resonance imaging from mouse models infected with human cancer cell lines and targeted by “supramolecular magnetic nanoparticles”-CA19-9 shows that, while the majority of the conventional MRI methods show no indication of tumors, our innovative approaches are successful in highlighting the tumor mass with close correlations of the sizes and locations with histopathology.

This year (2015), it is estimated that about 1.82 million people in US will be diagnosed with cancer, and about 0.73 million (40%) will die of it. While the death rate of most diseases has dropped significantly, cancer death rate has been maintained at about 40% over the past 60 years. If early tumor detection in stage I or II can be made possible and routine, about 30% of those who died of cancers their lives can actually be saved (based on various assumptions). Based upon the research training and experiences over my PhD study, I am now ready to target real-life cancer problems using our newly developed MR imaging methodologies, thereby transforming fundamental physical chemistry and imaging research into life-saving applications. In response to the urgency of these medical challenges, I am determined to achieve the research objectives during my continuous research as a postdoctoral researcher/temporary lecturer in this great Department with my PhD advisor.